Advancements of MRI Measurements of Bound and Pore Water Concentration of Cortical

Bone for Evaluation of Fracture Risk

By

Mary Katherine Manhard

Dissertation

Submitted to the Faculty of the

Graduate School of Vanderbilt University

in partial fulfillment of the requirements

for the degree of

DOCTOR OF PHILOSOPHY

in

Biomedical Engineering

August, 2016

Nashville, Tennessee

Approved:

Mark D. Does, Ph. D., Chair

Jeffry S. Nyman, Ph. D.

E. Brian Welch, Ph. D.

William A. Grissom, Ph. D.

S. Bobo Tanner, M.D.

TABLE OF CONTENTS

iv

LIST OF TABLES

LIST OF FIGURES

Chapter 1

Introduction and Background

The current standard for diagnosing fracture risk comprises measurements of bone mineral density (BMD), primarily by dual-energy X-ray absorptiometry (DXA). However, fracture resistance is affected by many factors other than BMD, such as architecture, collagen integrity, or cortical porosity. In addition, clinical risk factors such as age, previous fracture, family history, and use of corticosteroids can affect bone strength [1]. Recently, nuclear magnetic resonance (NMR) measures of the water bound to the collagen matrix (bound water) and free water occupying pore space (pore water) have shown promise in further assessing fracture risk [2], [3]. Nuclear Magnetic Resonance (NMR) based techniques have recently been translated into Magnetic Resonance Imaging (MRI) methods; the Double Adiabatic Full Passage (DAFP) sequence for measuring pore water concentration and the Adiabatic Inversion Recovery (AIR) sequence to measure bound water concentration. These imaging methods can be used to obtain maps of bound and pore water content throughout the cortical bone volume. Measures of bound and pore water concentration have the potential to give a new and more thorough evaluation of bone characteristics and health that is not obtainable with currently used methods.

The overall aim of the work presented in this dissertation is to advance clinically practical MRI methods for quantitatively imaging bound and pore water concentrations in cortical bone so that they will be useful in evaluating fracture risk. Chapter 1 gives a background of bone fracture risk and current diagnostic methods.

Chapter 2 reports on the translation and validation of the AIR and DAFP methods using a 3D ultra-short echo time (UTE) imaging technique for quantitatively measuring bound and pore water concentrations in human cortical bone. Previously, the AIR and DAFP methods were successfully developed and tested using non-imaging NMR-based sequences. These sequences were translated into imaging methods on the 4.7 Tesla (T)

and the 3T systems using clinically practical parameters to acquire bound and pore water maps in a reasonable scan time (under 30 minutes total for extremities). Some technical challenges specific to ultra-short echo time imaging of cortical bone are discussed in this translation. Finally, an experimental validation was performed by implementing the methods on ex vivo cadaveric femurs on both the small bore 4.7T system and the clinical 3T system to obtain 3D bound and pore water maps. Then, cored out sections underwent the previously validated non-imaging NMR measurements of bound and pore water content. These results were compared to corresponding regions of interest (ROIs) from the 3D images to verify that the bound and pore water concentrations were consistent.

In Chapter 3, the methods were further validated by assessing the measurements in vivo with healthy volunteers by imaging both the tibia and the radius. These bound and pore water concentration measurements were repeated three times and the variability of the measurements was assessed to confirm good repeatability of the methods.

The work in Chapter 4 evaluates the utility of the AIR and DAFP methods as predictors of whole bone mechanical properties. The hypothesis that MRI measures of bound and pore water concentrations would offer new information about the characterization of the bone that could help to better predict fracture risk was tested. Ex vivo cadaveric bones were obtained and imaged using the MRI AIR and DAFP methods along with non-MR imaging measures from X-ray for comparison. These bones underwent biomechanical tests and correlations were made between imaging measures and biomechanical properties. These tests assessed the relative contribution from structural properties, bone density, and bound and pore water to the strength and toughness of the bone.

Chapter 5 demonstrates the improved speed and flexibility of the DAFP and AIR methods with the implementation of 2D UTE with half-pulse excitation. The 3D AIR and DAFP methods, the initially developed techniques used in this dissertation work, require an isotropic resolution and need relatively long scan times to achieve an adequate resolution in long bones such as the radius and the tibia (on the order of 10-15 minutes per scan). With

certain anatomical sites, such as the femoral neck or in the distal radii, the cortical thickness is thin enough that a small voxel size may be needed to adequately resolve bound and pore water concentrations. Additionally, some locations such as the spine or hip are difficult to image without drastically increasing the field of view (FOV), resulting in long scan times. To overcome these difficulties, 2D AIR and DAFP was implemented on a clinical 3T Philips system to allow for much faster scans and more flexibility in volume covered. The signal-to-noise ratio (SNR) as well as the resulting bound and pore water concentration maps obtained from 2D AIR and DAFP imaging were quantitatively compared with the 3D AIR and DAFP methods.

Chapter 6 discusses the use of AIR and DAFP methods evaluated on patients undergoing drug treatment for osteoporosis before the start of treatment, and these were compared to healthy controls to test for differences between normal and osteoporotic bone. The results of this study display the excellent sensitivity of the AIR and DAFP methods, and further paves the way for future studies testing changes in bound and pore water concentrations with different disease groups and in response to drug treatment. The ability to image patients in this manner has the potential to help clinicians determine the efficacy of a drug treatment and subsequent patient response, and would potentially provide a new tool and knowledge for diagnosing and treating bone fracture risk.

1.1   The Burden of Bone Fracture

Bone fractures are a widespread problem that affect over 75 million people in the world, with more than 2.3 million fractures per year globally [4]. Over a lifetime, the risk of a fracture is around 40% for white Caucasian women in the United States, and is 13% for white Caucasian men [5]. Fractures often affect the elderly, where a fracture incident can be particularly detrimental and may cause individuals to become bedridden or require long term care for daily activities [4]. Bone fractures in high risk populations such as the elderly are associated with high rates of mortality, morbidity, and disability [6]. The most common

fragility fractures occur in the hip, the spine, and the wrist as these fractures often result from a fall, though they can happen spontaneously. Fractures can be extremely painful and result in hospitalization or surgery, and the costs associated with bone fracture risks are over 17 billion dollars per year in the United States alone [7]. Furthermore, the elderly population in the United States is increasing rapidly, and fracture-related costs are expected to increase by 50% by the year 2025 [7].

Increases in bone fractures and bone fracture risk occur for a variety of reasons, and are often related to aging. Fractures are a particularly large problem in post-menopausal women because of the role of estrogen in bone remodeling [8]. Several diseases and disorders are also associated with increased fracture risk, including some genetic diseases such as cystic fibrosis and osteogenesis imperfecta, hypogonadal states such as anorexia nervosa or Turner's syndrome, some gastrointestinal disorders, hematologic disorders, and endocrine disorders such as hyperparathyroidism and diabetes mellitus [9]. Diabetes in particular has a rapidly increasing prevalence [10], leading to even higher costs and an increasing need for comprehensive clinical procedures to accurately measure and diagnose fracture risk.

1.2 Bone Biology and Implications for Fracture Risk

Human bone is comprised of cortical bone and cancellous (also known as trabecular or spongy) bone. Cortical bone makes up approximately 80% of the skeleton [11] and is comprised of a mineral component (primarily crystals of calcium phosphate), an organic matrix (primarily type 1 collagen), lipids, and porous spaces that are filled with fluid. Osteons, the functional units of cortical bone, are approximately $100\,\mu$m in diameter, are separated from each other by layers of lipids, and run parallel to the length of the bone. At the center of an osteon is the Haversian canal, which carries nerves and blood vessels and includes most of the bone's porosity. The rest of the bone's porosity is in the lucuno-canalicular system. Lacunae are small spaces in the mineral and collagen matrix than contain individual osteo-

cytes, are important for cell communication and nutrition in the bone and are connected by small transverse canals, the canaliculi. Volkmann canals run between different Haversian canals and help the transport of blood and nutrients. Osteoblasts and osteoclasts are cells that reside on the surface of the bone and regulate bone remodeling and resorption, and abnormalities in these cells activity can decrease mineral content or collagen content and ultimately increased fracture risk [12].

The mineral component of bone gives it its strength and stiffness, but is also extremely brittle. Collagen fibers and the cross-linking of collagen gives bone plasticity, which allows bones to absorb energy without breaking after the onset of permanent deformation (i.e., post-yield strain) [12], [13]. Both the strength and plasticity of bone help to increase fracture resistance. Bone fracture risk increases with low bone mineral density (BMD) or poor collagen content. Fracture risk increase typically is attributed to a decrease in BMD, though changes in collagen organization or condition also affect fracture risk. As a person ages, the collagen integrity of their bones decreases which results in increased brittleness of the bone [14], [15], leading to a significant increase in fracture risk.

Clinically, an individual is typically diagnosed as being at high fracture risk by measures of low BMD or by the incidence of a fracture. Since current BMD measurements are known to not fully reflect a patient's fracture risk, other risk factors and secondary markers of fracture risk are often used clinically in combination with BMD to determine treatment. For example, biochemical markers of bone turnover can be used to predict risk of fracture and rapidity of bone loss; bone resorption markers include high serum beta C-telopeptite levels and the presence of N-telopeptite of type I collagen in the urine, while markers of bone formation markers include alkaline phosphatase, osteocalcin, and aminoterminal propeptide of type I procollagen (P1NP) [9]. However, these markers are subjective to day-to-day variability and are not specific to any bone or bone mechanical property [16].

Another recently developed tool is the World Health Organization's Fracture Risk Algorithm (FRAX) [9]. This online tool helps predict the 10-year probability of a fracture

by combining BMD scores as well as other risk factors such as age, sex, history of fracture, smoking and alcohol consumption, and various diseases associated with high fracture. However, the FRAX system is only designed to guide clinical decisions and still lacks additional information about the composition of the bone itself [17], [18].

1.3   Current Imaging Methods for Assessing Fracture Risk

Dual X-ray Absorptiometry (DXA) is the most commonly used imaging technique for fracture risk diagnosis and is considered the gold standard methodology in the clinic. It was first introduced in 1987, and is fast, inexpensive, and a well-validated and well-studied method that has very low radiation dose (5-20 μSv). DXA uses two X-rays at two different energy levels and subtracts soft-tissue components to get a measure of bone mineral density (BMD) on a two-dimensional, areal basis. The World Health Organization has identified T-scores to classify an individual's BMD measurements, defined as the standard deviation of BMD relative to a young healthy population of the same ethnicity and sex [8]. Osteoporosis is defined as having a T-score lower than -2.5 (standard deviations away from normal); osteopenia is defined as having a T-score lower than 1. However, DXA has many limitations — this method can only generate a two-dimensional projection of the bone, and varies significantly based on anatomical structure, making bone size and orientation critical factors. Degenerative disc disease or calcifications can lead to an increased apparent BMD and falsely lower a fracture risk diagnosis [1], [19], while other imaging artifacts arising from excess soft tissue in obese patients or prosthetic implants in the background can also severely alter DXA results. In addition, DXA does not fully explain the age-related increase in fracture risk [20] nor the increase in fracture with diabetes [21].

Quantitative computed tomography (QCT) is much less used clinically than DXA, but can obtain volumetric measures of BMD [22]. QCT takes conventional CT bone imaging measurements from the patient and uses concurrently-imaged phantoms with known BMD values to project the BMD over the entire patient bone volume. Volumetric measures

such as cross sectional moment of inertia and cortical bone thickness can help determine whole bone mechanical properties [19], [23], [24], and unlike DXA, volumetric BMD measurements are not sensitive to degenerative disease. QCT also allows for trabecular bone density measurements, though the resolution of these QCT scans is relatively low. High resolution peripheral QCT (HR-pQCT) uses a dedicated imaging system for extremities to get higher resolution and SNR than conventional QCT. This allows for both BMD measurements and visualization of trabecular and cortical bone architecture, such as porosity. These properties can be used in finite element modeling to estimate mechanical properties from structure and BMD on a voxel-by-voxel basis, to help better determine fracture risk [25]–[27]. HR-pQCT is still limited to the extremities, and has high radiation exposure and higher cost than DXA. These factors, along with the limited validation of QCT methods for diagnosing fracture risk in comparison to the relatively well-studied DXA methodology, leads QCT to be a secondary technique for measuring fracture risk clinically.

Quantitative ultrasound (QUS) is another method less frequently used, but has shown some promise in distinguishing between fractured and non-fractured subjects [28]. Quantitative ultrasound of bone is typically performed in the calcaneus of the heel, which is of particular interest as it is one of the only peripheral bones comprised primarily of trabecular bone. While most fractures begin in cortical bone, bone loss usually begins in trabecular bone, so it is often of interest to detect early changes in bone quality. QUS measures both velocity and amplitude of ultrasound waves through bone tissue. This has been shown to reflect elastic modulus and compressive strength. However, ultrasound usage is not standardized and results can be influenced by positioning and devices. While it offers a radiation-free method of assessing bone, the efficacy of the methods need to be improved before it is a clinically viable tool [28].

Micro-MRI, or μMRI is a method that has been recently used to evaluate structure and trabecular bone architecture [29]–[31], usually at the extremities though it has also been applied at the proximal femur [32]. Micro-MRI can also be used with finite element

modeling to predict mechanical properties from structure, and is a useful tool because of the lack of radiation. However, problems such as susceptibility artifacts can change the apparent size of trabeculae and make evaluating results difficult [33].

The imaging measurements of bone quality discussed thus far are are only sensitive to the mineral composition of bone, and do not account for soft tissue components such as the collagen matrix. The collagen content of bones can not be measured with standard methods, and there is a need for improved diagnostic methods for measuring bone fracture risk. MRI has the ability to measure both the concentration of water bound to collagen and the concentration of water existing in the pores of the bone. Developing MRI based methods to evaluate bone fracture risk could yield better and safer imaging methods for treatment planning in cases of osteoporosis, diabetes, and other diseases associated with increased bone fracture.

1.4   Nuclear Magnetic Resonance Studies of Cortical Bone

Before MR methods of imaging cortical bone were developed, non-imaging methods with hydrogen proton (^{1}H) NMR have characterized the proton signal from cortical bone. NMR has been used to determine micro-structural characteristics of many types of porous materials [34]–[36], and has also been applied to human cortical bone [37]–[40].

NMR measures magnetization from hydrogen proton spins, which are aligned with an external magnetic field, B_0. The frequency (ω_0) that spins process about B_0 is related by the gyromagnetic ratio, γ:

$$\omega_0 = \gamma B_0 \tag{1.1}$$

For ^{1}H, this ratio is 26,751 rad/s/G. By applying radiofrequency (RF) pulses to tip magnetization away from equilibrium, an NMR signal can be measured in the plane transverse to the B_0 field. Different tissues experience different relaxation properties that dictate sig-

nal contrasts in MR. T_1 is the time constant that describes the rate at which the longitudinal magnetization recovers back to equilibrium. Longitudinal relaxation is often referred to as spin-lattice relaxation, and describes relaxation that occurs because of interactions of spins with its surrounding environment. T_2 is the time constant that describes the rate of transverse relaxation. Transverse relaxation refers to the excited signal dephasing, or becoming incoherent, in response to spin-spin interactions as well as variations in the local magnetic field.

Carr-Pucell-Meiboom-Gill (CPMG) pulse sequences use a 90° RF excitation pulse followed by a train of 180° refocusing pulses, where an acquisition is collected at the echo time after each refocusing pulse [41]. The CPMG pulse sequence can be used to measure the T_2 of proton signals of cortical bone signal. By acquiring the CPMG signal at many echo times and fitting the data in a non-negative least squares sense to a sum of decaying exponentials, a T_2 spectrum can be produced, which shows the relative amount of protons across a large range of T_2 values.

In cortical bone, three main pools of proton signal are observed. The protons from the collagen in cortical bone make up the pool with the shortest T_2 relaxation times (less than 100 μs). This signal is too short to be measured with standard clinical imaging methods. The water bound to the collagen matrix of cortical bone (bound water) has a relatively short T_2 relaxation time, between $100 - 1000$ μs [2]. Finally, the water in the porous space of cortical bone (pore water) has a longer T_2 relaxation time, and spans a range of T_2 values from 1 ms $-$ 1 s. The T_2 values of pore water generally correspond with pore size [39]. An example of a fitted CPMG curve and the resulting T_2 spectrum from cortical bone can be seen in Figure 1.1 below.

On clinical MRI scanners, T_2 can not be easily measured because the echo time needed for a spin echo sequence is typically too long to measure these short T_2 components, so T_2^* values are used instead. Average T_2^* values over a bone can be found using bi-exponential fitting of the free induction decay (FID) signal magnitude, resulting in bound water T_2^*
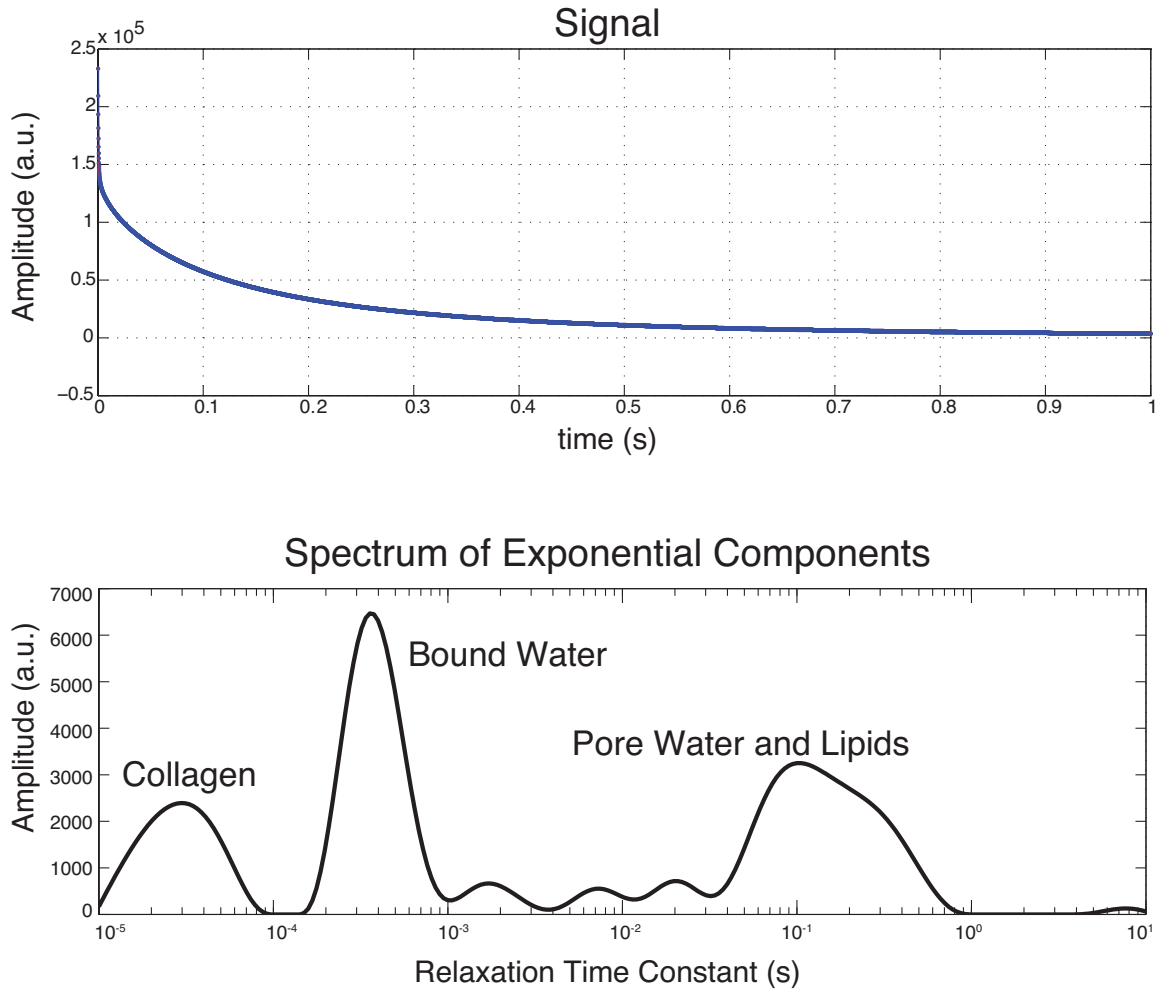
Figure 1.1: Signal decay shown with raw and fitted values (fit to 100 T_2 relaxation times) from a CPMG sequence acquired on a cortical bone sample with 10,000 echos (top). The resulting relaxation time spectrum from the fitted curve (bottom). The signal from the collagen is below 100 μs, the signal from the collagen bound water is between $100 - 1000$ μs, and the signal from pore water spans between 1 ms $- 1$ s

values on the order of 400 μs at 4.7T and pore water T_2^* values averaging 1280 μs at 4.7T [42].

These NMR measurements of collagen, bound water, and pore water led to the determination of correlations of these measurements with mechanical properties [43]. Cortical bone samples from human femurs were used for NMR measurements to determine proton concentrations from bound water, pore water, and collagen. Adjacent sections of cortical

bone were used for μCT measurements to compare NMR measures to X-ray measures for fracture risk prediction. A third segment was used for mechanical testing. The NMR signals from collagen, bound water, and pore water showed a strong linear correlation with mechanical properties of bone, though the net signal did not. The NMR measures were found to be better predictors (higher correlation) than the μCT measures in three of four measured mechanical properties. In particular, bones with a greater concentration of bound water and a lower concentration of pore water were found to have generally greater mechanical properties (i.e., higher values of peak stress, yield stress and pre-yield toughness). However, because the bound water and pore water concentration had opposite relationships to mechanical properties, NMR measures that included signal from both bound and pore water had relatively weak predictive values of mechanical properties.

These results suggest that appropriate MRI methods that robustly distinguish and quantitatively measure bound- and pore-water concentrations in cortical bone may offer a viable methodology for predicting fracture risk. A challenge in developing such methods stems from observations that while bound- and pore-water exhibit widely different T_2 values, their T_2^* values are much more similar [42]. Thus, using conventional UTE MRI with T_2^* weighted contrast to differentiate between bound and pore water signal (for example, using a combination of a short echo time and a longer echo time to which in theory only the pore water signal is sensitive to) may not be effective in robustly distinguishing these two signal components.

Alternatively, recently proposed methods for bound- and pore-water UTE MRI utilize adiabatic radiofrequency (RF) pulses to provide T_2 selective RF pulses over a broad enough resonance bandwidth to effectively distinguish bound- and pore-water signals [42]. The pore water signal is distributed over a large bandwidth, and therefore needs to be inverted with a large bandwidth RF pulse. Conventional pulses have a constant carrier frequency that is applied at the center of the spectrum being excited. Adiabatic pulses, or frequency modulated RF pulses, sweep through a range of carrier frequencies over the duration of the

pulse. These pulses have the ability to encompass large bandwidths and long durations. Because they include a large range of frequencies, a pore water signal can be effectively manipulated over a large range of T_2 values. However, adiabatic pulses do not have the conventional relationship between flip angle and B_1 amplitude, and instead, the direction of the magnetization stays the same as the direction of the effective B field, given that the effective magnetic field changes significantly more slowly than the rotation of the signal magnetization about the effective field (adiabatic condition). This means that the effective B_1 amplitude needs to be large relative to the rate of change of the angle of the effective B_1 over time. Consequently, the adiabatic condition in the presented pulses for selectively measuring bound and pore water is held by using a high B_1 amplitude with a relatively long pulse duration.

With high B_1 and long pulse durations, the amount of power delivered to the tissue is relatively high. The specific absorption rate (SAR) is a measure of how much power is absorbed by the tissue, and therefore how much heating the tissue experiences (usually limited to $1-3°C$) For example, the FDA limits of SAR are 12 W/kg in any gram of tissue for 15 minutes in extremities such as the leg or forearm, and 8 W/kg in any gram of tissue for 15 minute of in the torso [44]. To limit SAR deposition, longer repetition times (TRs) need to be used, which results in longer scan times.

Two clinically compatible methods for distinguishing bound and pore water were developed using adiabatic pulses [42]. A hyperbolic secant (sech), adiabatic full passage (AFP) pulse rotates magnetization $180°$ over a range of frequencies. A preparatory AFP pulse will invert pore water while saturating the bound water. Playing two consecutive broad-bandwidth adiabatic full passage pulses will drive short T_2 magnetization (bound water) to saturation while rotating long T_2 magnetization (pore water) through $360°$, leaving it essentially unaffected. This approach is referred to as the Double Adiabatic Full Passage (DAFP) method. To image bound water, a similar approach uses one adiabatic full passage pulse followed by an appropriate delay to invert and null pore water magnetization while

the bound water magnetization experiences a saturation-recovery process. This approach is referred to as the Adiabatic Inversion Recovery (AIR) method. The magnetization of bound and pore water during these pulses are illustrated in Figure 1.2 below. These methods create the basis for the following imaging studies in this work.

AIR
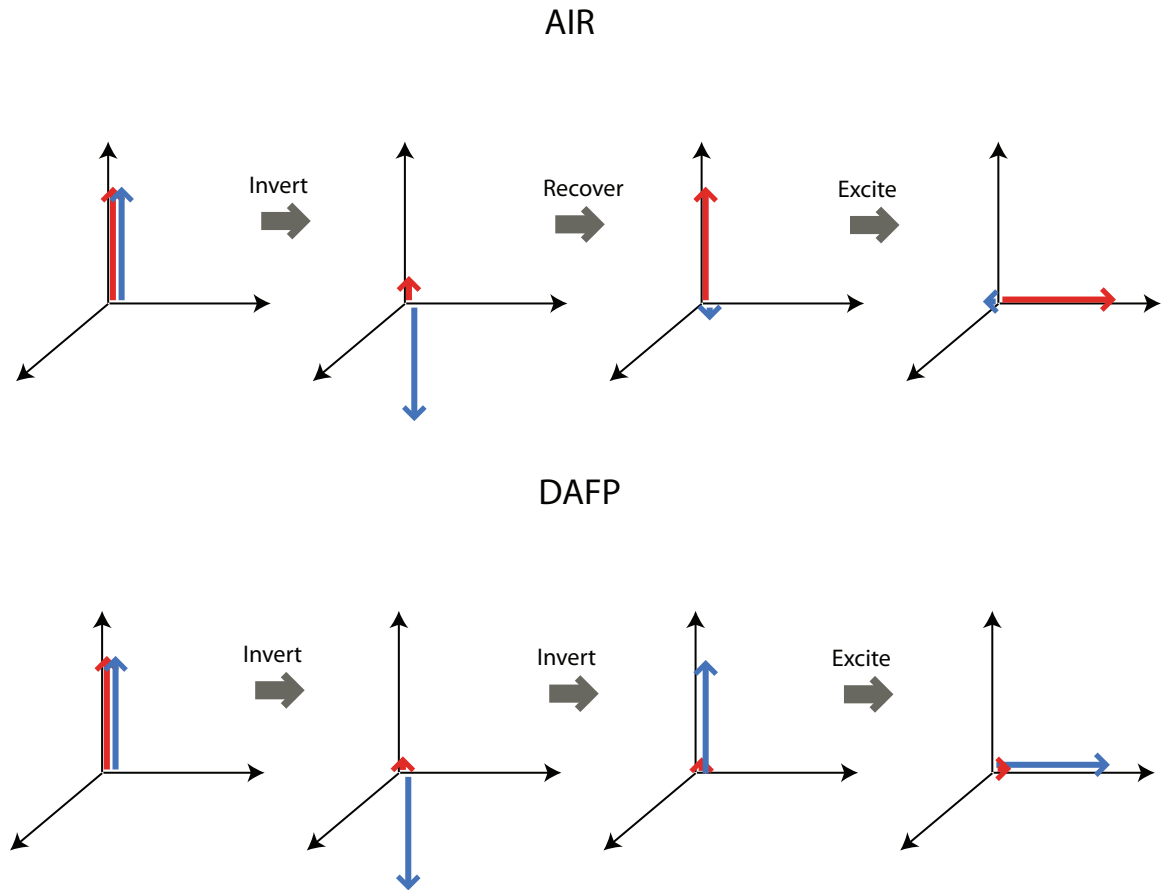
DAFP

Figure 1.2: The sequence of magnetization of bound water signal (red) and pore water signal (blue) is shown for both the AIR and DAFP pulse and UTE acquisition

1.5 References

[1] J. Kanis, "Diagnosis of osteoporosis and assessment of fracture risk.," *Lancet*, vol. 359, no. 9321, pp. 1929–36, Jun. 2002.

[2] R. A. Horch, J. S. Nyman, D. F. Gochberg, R. D. Dortch, and M. D. Does, "Characterization of 1h nmr signal in human cortical bone for magnetic resonance imaging.," *Magn Reson Med*, vol. 64, no. 3, pp. 680–7, Sep. 2010.

[3] H. H. Ong, A. C. Wright, and F. W. Wehrli, "Deuterium nuclear magnetic resonance unambiguously quantifies pore and collagen-bound water in cortical bone.," *J Bone Miner Res*, vol. 27, no. 12, pp. 2573–2581, Jul. 2012.

[4] W H O Scientific Group, "Prevention and management of osteoporosis," World Health Organization, Geneva, Tech. Rep., 2003.

[5] W. H. Organization, "Who scientific group on the assessment of osteoporosis at primary health care level," World Health Organization, Brussels, Belgium, Tech. Rep., 2004.

[6] W. H. Organization, "The world health report 1997, conquering suffering enriching humanity," World Health Organization, Geneva, Tech. Rep., 1997.

[7] R. Burge, B. Dawson-Hughes, D. H. Solomon, J. B. Wong, A. King, and A. Tosteson, "Incidence and economic burden of osteoporosis-related fractures in the united states, 2005 to 2025," *J Bone Miner Res*, vol. 22, no. 3, pp. 465–475, 2007.

[8] W. H. Organization, "Technical report: assessment of fracture risk and its application to screening for postmenopausal osteoporosis," World Health Organization, Geneva, Tech. Rep., 1994.

[9] N. O. Foundation, "Clinician's guide to prevention and treatment of osteoporosis," National Osteoporosis Foundation, Washington, DC, Tech. Rep., 2014.

[10] S. Wild, G. Roglic, A. Green, R. Sicree, and H. King, "Global prevalence of diabetes: estimates for the year 2000 and projections for 2030," *Diabetes Care*, vol. 27, no. 5, pp. 1047–1053, 2004.

[11] B. Clarke, "Normal bone anatomy and physiology.," *Clinical journal of the American Society of Nephrology : CJASN*, vol. 3 Suppl 3, S131–9, Nov. 2008.

[12] E. Seeman and P. D. Delmas, "Bone quality the material and structural basis of bone strength and fragility," *N Engl J Med*, vol. 354, pp. 2250–2261, 2006.

[13] P. A. Downey and M. I. Siegel, "Bone biology and the clinical implications for osteoporosis," *Physical Therapy*, vol. 86, no. 1, pp. 77–91, 2006.

[14] P. Zioupos, J. D. Currey, and A. J. Hamer, "The role of collagen in the declining mechanical properties of aging human cortical bone," *J Biomed Mater Res*, vol. 45, no. 2, pp. 108–116, 1999.

[15] X. Wang, X. Shen, X. Li, and C. M. Agrawal, "Age-related changes in the collagen network and toughness of bone," *Bone*, vol. 31, no. 1, pp. 1–7, 2002.

[16] K. S. Davison, D. L. Kendler, P. Ammann, D. C. Bauer, D. W. Dempster, L. Dian, D. a. Hanley, S. T. Harris, M. R. McClung, W. P. Olszynski, and C. K. Yuen, "Assessing fracture risk and effects of osteoporosis drugs: bone mineral density and beyond.," *The American journal of medicine*, vol. 122, no. 11, pp. 992–7, Nov. 2009.

[17] J. A. Kanis, D. Hans, C. Cooper, S. Baim, J. P. Bilezikian, N. Binkley, J. a. Cauley, J. E. Compston, B. Dawson-Hughes, G. El-Hajj Fuleihan, H. Johansson, W. D. Leslie, E. M. Lewiecki, M. Luckey, A. Oden, S. E. Papapoulos, C. Poiana, R. Rizzoli, D. a. Wahl, and E. V. McCloskey, "Interpretation and use of frax in clinical practice," *Osteoporosis Int*, vol. 22, no. 9, pp. 2395–411, Sep. 2011.

[18] A. Unnanuntana, B. P. Gladnick, E. Donnelly, and J. M. Lane, "The assessment of fracture risk," *J Bone Joint Surg Am*, vol. 92, pp. 743–753, 2010.

[19] M. L. Bouxsein, "Technology insight : noninvasive assessment of bone strength in osteoporosis," *Nat Clin Pract Rheum*, vol. 4, no. 6, pp. 310–318, 2008.

[20] J. Kanis, O. Johnell, A. Oden, A. Dawson, C. De Laet, and B. Jonsson, "Ten year probabilities of osteoporotic fractures according to bmd and diagnostic thresholds," *Osteoporosis Int.*, vol. 12, no. 12, pp. 989–995, 2001.

[21] A. V. Schwartz and D. E. Sellmeyer, "Diabetes , fracture , and bone fragility," *Current osteoporosis reports*, vol. 5, no. 3, pp. 105–111, 2007.

[22] J. E. Adams, "Quantitative computed tomography.," *European journal of radiology*, vol. 71, no. 3, pp. 415–24, Sep. 2009.

[23] S. L. Manske, T. Liu-Ambrose, P. M. Bakker, D. Liu, S. Kontulainen, P. Guy, T. Oxland, and H. McKay, "Femoral neck cortical geometry measured with magnetic resonance imaging is associated with proximal femur strength," *Osteoporosis Int.*, vol. 17, no. 1, pp. 1539–1545, 2006.

[24] D. M. Black, M. L. Bouxsein, L. M. Marshall, S. R. Cummings, T. F. Lang, and J. A. Cauley, "Proximal femoral structure and the prediction of hip fracture in men: a large prospective study using qct," *J Bone Miner Res*, vol. 23, no. 8, pp. 1326–1333, 2008.

[25] J. H. Keyak, S. a. Rossi, K. a. Jones, and H. B. Skinner, "Prediction of femoral fracture load using automated finite element modeling.," *J Biomech*, vol. 31, no. 2, pp. 125–33, Feb. 1998.

[26] W. Pistoia, B. van Rietbergen, E.-M. Lochmüller, C. a. Lill, F. Eckstein, and P. Rüegsegger, "Estimation of distal radius failure load with micro-finite element analysis models based on three-dimensional peripheral quantitative computed tomography images," *Bone*, vol. 30, no. 6, pp. 842–8, Jun. 2002.

[27] R. Crawford, C. E. Cann, and T. M. Keaveny, "Finite element models predict in vitro vertebral body compressive strength better than quantitative computed tomography," *Bone*, vol. 33, no. 4, pp. 744–750, Oct. 2003.

[28] G. Guglielmi, J. Adams, and T. M. Link, "Quantitative ultrasound in the assessment of skeletal status.," *Eur Radiol*, vol. 19, no. 8, pp. 1837–48, Aug. 2009.

[29] M. J. Wald, J. F. Magland, C. S. Rajapakse, Y. a. Bhagat, and F. W. Wehrli, "Predicting trabecular bone elastic properties from measures of bone volume fraction and fabric on the basis of micromagnetic resonance images," *Magn Res Med*, vol. 68, no. 2, pp. 463–73, Aug. 2012.

[30] N. Zhang, J. F. Magland, C. S. Rajapakse, Y. a. Bhagat, and F. W. Wehrli, "Potential of in vivo mri-based nonlinear finite-element analysis for the assessment of trabecular bone post-yield properties.," *Medical physics*, vol. 40, no. 5, p. 052 303, May 2013.

[31] G. Chang, C. M. Deniz, S. Honig, C. S. Rajapakse, K. Egol, R. R. Regatte, and R. Brown, "Feasibility of three dimensional mri of proximal femur microarchitecture at 3 tesla using 26 receive elements without and with parallel imaging," *J Magn Reson Img*, vol. 40, no. 1, pp. 229–38, Jul. 2014.

[32] A. Hotca, C. S. Rajapakse, C. Cheng, S. Honig, K. Egol, R. R. Regatte, P. K. Saha, and G. Chang, "In vivo measurement reproducibility of femoral neck microarchitectural parameters derived from 3t mr images," *J Magn Reson Img*, vol. 42, pp. 1339–1345, 2015.

[33] J. Folkesson, J. Goldenstein, J. Carballido-gamio, G. Kazakia, A. J. Burghardt, A. Rodriguez, R. Krug, A. E. D. Papp, T. M. Link, and S. Majumdar, "Longitudinal evaluation of the effects of alendronate on mri bone microarchitecture in postmenopausal osteopenic women," *Bone*, vol. 48, no. 3, pp. 611–621, 2011.

[34] C. L. Glaves and D. M. Smith, "Membrane pore structure analysis via nmr spin-lattice relaxation experiments," *J Membrane Sci*, vol. 46, pp. 167–184, 1989.

[35] M. Chui, R. Phillips, and M. McCarthy, "Measurement of the porous microstructure of hydrogels by nuclear magnetic resonance," *J Colloid Interf Sci*, vol. 174, pp. 336–344, 1995.

[36] W. E. Kenyon, "Petrophysical principles of applications of nmr logging," *Log Analyst*, vol. 38, pp. 21–43, 1997.

[37] X. Wang and Q. Ni, "Determination of cortical bone porosity and pore size distribution using a low field pulsed nmr approach.," *J Orthopaed Res*, vol. 21, no. 2, pp. 312–9, Mar. 2003.

[38] Q. Ni and D. P. Nicolella, "The characterization of human cortical bone microdamage by nuclear magnetic resonance," *Measurement Science and Technology*, vol. 16, no. 3, pp. 659–668, Mar. 2005.

[39] P. Fantazzini, R. J. S. Brown, and G. C. Borgia, "Bone tissue and porous media: common features and differences studied by nmr relaxation," *Magn Reson Img*, vol. 21, no. 3-4, pp. 227–234, Apr. 2003.

[40] Q. Ni, J. D. King, and X. Wang, "The characterization of human compact bone structure changes by low-field nuclear magnetic resonance," *Measurement Science and Technology*, vol. 15, no. 1, pp. 58–66, Jan. 2004.

[41] S. Meiboom and D. Gill, "Modified spinecho method for measuring nuclear relaxation times," *Rev. Sci. Instrum*, vol. 29, no. 8, pp. 688–691, 1958.

[42] R. A. Horch, D. F. Gochberg, J. S. Nyman, and M. D. Does, "Clinically compatible mri strategies for discriminating bound and pore water in cortical bone.," *Magn Reson Med*, vol. 68, no. 6, pp. 1774–84, Dec. 2012.

[43] R. A. Horch, D. F. Gochberg, J. S. Nyman, and M. D. Does, "Non-invasive predictors of human cortical bone mechanical properties: t(2)-discriminated h nmr compared with high resolution x-ray.," *PloS one*, vol. 6, no. 1, e16359, Jan. 2011.

[44] F. Administration and Drug, "Guidance for the submission of premarket notifications for magnetic resonance diagnostic devices," U.S. Department of Health and Human Services, Center for Devices and Radiological Health, Tech. Rep., 1998.

Chapter 2

Translation of NMR Methods to Imaging Methods for Bone Quantification

2.1   Ultra-short echo time (UTE) Imaging and Pulse Sequence Design

Conventional MRI is not well suited for imaging cortical bone signals because the T_2 of bone is extremely short compared to typical echo times (TEs). Ultra-short echo time (UTE) imaging uses a spoiled gradient echo sequence and allows for acquisition of signals with T_2 relaxation times on the order of microseconds, and this has been successfully applied to cortical bone [1]–[7].

Typical MRI sequences use Cartesian sampling to acquire k-space (the Fourier transform of the image). In UTE imaging, radial trajectories are acquired from the center of k-space. After the excitation, the read out gradient is ramped up rapidly while beginning acqusition to acquire the maximum amount of data. Typically, acquisition begins after the gradient has finished ramping, but in the case of UTE, acquisition begins on the ramp (this is referred to as ramp sampling) to further shorten TE, so data acquisition can begin as soon as the excitation pulse is finished and the RF switching from transmit to receive is completed. The radial trajectories are measured prior to image acquisition to find a precise location in k-space for each data point acquired. After the acquisition, a non-uniform Fourier transform is applied to the k-space data to reconstruct an image. The data is first density compensated using an iterative method - because the data is not spread proportionally across k-space as in Cartesian acquisitions, but instead has a majority of signal at the center, the k-space data needs to be weighted appropriately. K-space data is then gridded on to Cartesian coordinates so that it can be reconstructed using standard discrete Fourier transform (DFT) methods [8].

The order of acquisition of the radial spokes, or views, is an important factor to consider as views close together in k-space can lead to coherent artifacts in image space. The

view ordering used in the sequences described in this dissertation use Wong's method for uniformly sampling on a sphere [9]. The direction of each spoke in 3D k-space is found by moving spirally in the x and y directions of k-space, and linearly in the z direction, split between multiple passes. If acquired in one pass, each spoke is relatively close to the next, which could potentially lead to unwanted effects such as stimulated echoes and excitation from adjacent spokes. By acquiring the same number of radial spokes in multiple passes, this problem can be avoided because the acquired radial spokes are more spread out in k-space over time.

The DAFP and AIR methods discussed above are incorporated into 3D UTE sequences, as shown in Figure 2.1.
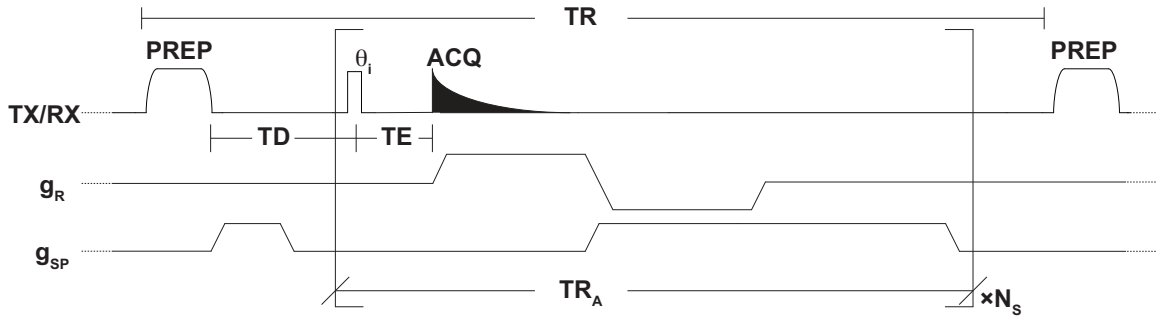
Figure 2.1: The 3D-UTE pulse sequence used. The PREP pulse is a double HS8 pulse for DAFP and a single HS8 pulse for AIR. The time delay between the end of the preparation pulse and the start of data acquisition is TD. The effective inversion-recovery time $TI = TD + TR_A \times N_S/2$, where N_S radial spokes are acquired with period TR_A during every TR period. g_R and g_{SP} show the readout gradient and the spoiler gradient, respectively.

The AFP pulses used are 10 ms in duration and have a 3500 Hz bandwidth. These pulses were previously shown to measure signal that was largely composed of bound water (AIR) or largely composed of pore water (DAFP) in NMR measurements [10], leading to the whole bone imaging studies presented in this work. Several technical challenges specific to these AIR and DAFP methods arise when quantifying bound and pore water concentrations, which are detailed in the next section along with proposed solutions.

2.2 Overcoming Technical Challenges of Cortical Bone Imaging with UTE MRI

2.2.1 Trajectory Measurements

In typical Cartesian measurements, the readout gradient ramps up before acquisition and acquisition occurs along a constant gradient strength, which results in a linear trajectory through k-space. For UTE measurements, acquisition begins on the ramp up of the gradient to minimize TE. However, the gradient during this ramp is not perfectly linear, and distortions, eddy currents, or the propagation delay in the gradient waveform can lead to large errors in the assumed k-space trajectory. Since the acquisitions are being acquired in a center-out fashion, the large errors in the assumed trajectory are near the center of k-space, which leads to significant errors in image space.

To avoid this error in assumed trajectories during reconstruction, the actual gradient waveforms can be measured and then used in reconstruction to reduce blurring of signal in the image. In the studies in this work, the gradient waveform measurement was performed using a modified Duyn's method [11] on both the Varian small animal system and the Philips human imaging system. Briefly, this method plays out a slice select gradient followed by acquisition during which the gradient waveform to be measured is played out. This is repeated with the gradient waveform off. The difference in phase accrued in each point read out ($\Delta\phi(t)$) is proportional to the location in k-space, $k(t)$, as can be seen from equation 2.1:

$$\Delta\phi(t) = \int_0^t \gamma G(t) D dt = D k(t) \tag{2.1}$$

where $G(t)$ is the gradient waveform being measured and D is the distance the selected slice is from isocenter. On the 3T Philips scanner, the trajectories were measured along the x, y, and z axes, and then interpolated to all trajectories in k-space. Below Figure 2.2 shows an example measured gradient waveform along with the ideal gradient waveform to illustrate typical changes between ideal and actual waveforms. Because of the predistortion

used in Philips gradient performance, the actual waveform has a slightly earlier start than
the ideal waveform.
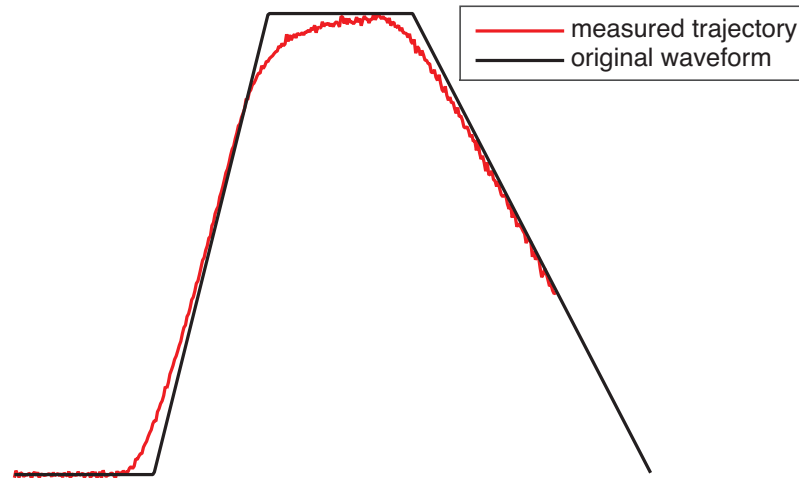
Figure 2.2: Ideal (black) and measured readout waveforms on the 3T using a modified
Duyn's method. The measured waveform is shown in red.

Without use of measured trajectories in reconstruction, substantial blurring and poor
image quality occurs. If measurements are not performed and assumed trajectories are
used instead in reconstruction, this could have a significant impact on quantitative results
in bound and pore water concentration maps.

2.2.2 Variable Flip Angle Approach

Acquiring multiple radial views with one magnetization preparation pulse significantly
decreases scan time and accelerates acquisition, which is necessary when translating to
practical human studies. Conventional Magnetization Prepared Rapid Gradient Echo (MP-
RAGE) protocols [12] are commonly used for this purpose. If a constant flip angle is
used over the course of the acquisitions, the transverse magnetization decreases with every
acquisition. Radial trajectories are especially sensitive to these changes because the origin
of k-space is sampled with every spoke. To keep transverse magnetization constant over
the course of the acquisitions, a variable flip angle approach was used, where the flip angle

was increased over the acquisitions for one preparation pulse [13].

The solution to the variable flip angle approach can be analytically solved for by neglecting relaxation effects. Because the time between acquisitions is short ($\approx$3 ms), longitudinal relaxation during the train of acquisitions is extremely short and can be neglected with minimal effects. For example, assuming a bound water T_1 = 350 ms, the signal would decay by less than 1% per acquisition. This leads to a simple geometric relationship between the longitudinal magnetization (M_z), the transverse magnetization (M_T), and the flip angle (θ):

$$M_z(n+1) = sin(\theta)M_z(n) \tag{2.2}$$

$$M_T(n+1) = cos(\theta)M_z(n) \tag{2.3}$$

where n is the acquisition number. If flip angles over the course of the sequence are found such that the transverse magnetization is held constant over the train of acquisitions for a desired train length, an equation for θ can be solved for:

$$\theta(n) = arctan(sin(\theta(n+1))) \tag{2.4}$$

This method maximizes the signal for greater SNR efficiency. This flip angle schedule and its effects on magnetization is demonstrated in Figure 2.3.

2.2.3 Receive Field Calibration

The coils used in these studies on the Philips 3T system were receive only, primarily the 8 channel knee coil and 8 channel wrist coil, and RF transmission was performed by the body coil. The receive field (B_1^-) is quite inhomogeneous for these small dedicated receive only coils, and so for quantitative imaging, it is necessary to map the B_1^- field. For
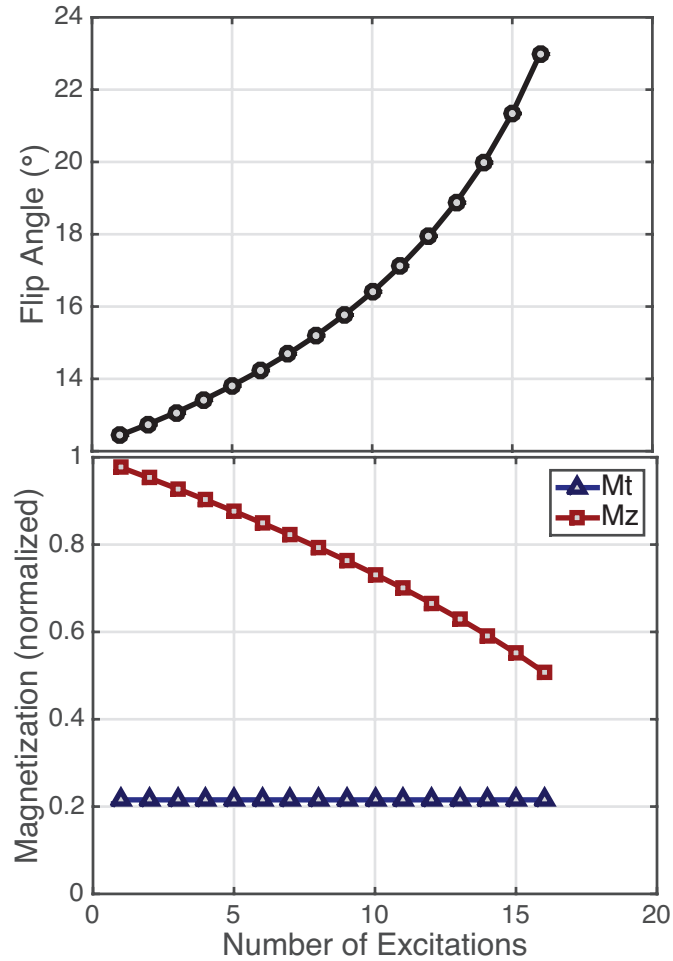
Figure 2.3: This diagram shows a sequence of 16 flips after one preparation pulse. The top graph shows the change in flip angle over the 16 acquisitions, ranging from 12.5 to 23. The bottom graph shows the longitudinal (red) and transverse (blue) magnetization. This method holds the transverse magnetization constant over the course of the flip angles.

most tissues, the scanner's automatic reference calibration (referred to as Constant LEvel AppeaRance, or CLEAR by the Philips system) will solve this problem. However, this automated correction filters out signal in bone regions because typical imaging sequences do not have a significant amount of bone signal.

To manually solve for the receive field map, a homogeneous B_1^- field from the body coil is assumed within the region inside the receive coil. A ratio of low resolution images acquired with i) the body coil for receiving and ii) the receive coil of interest for receiving

will give a map that gives the relative B_1- field for every location inside the field of view. The ratio of these images is smoothed using an apodized window and multiplied by all images to get B_1^- calibrated images. In these UTE bone scans, the B_1^- field is manually calibrated for every subject. An example of a B_1- map applied to a UTE image is shown in Figure 2.4.

Uncorrected   Corrected
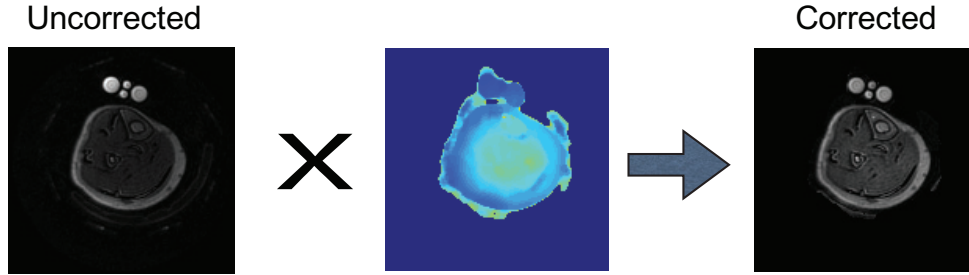
Figure 2.4: The receive field (center) is calibrated as a smoothed ratio of images acquired with 1) the body coil (S_{body}) and 2) the receive coil of interest (S_{knee}). The map is multiplied by the UTE image (left) to find a B_1^- corrected image (right).

2.2.4 Signal Amplitude Correction from Relaxation-Induced Blurring

As the relaxation times of bound and pore water are similar to the acquisition duration, it is necessary to account for the effect of transverse relaxation during the acquisition on image signal amplitude. Relaxation during acquisition broadens the image-domain point spread function, which can blur a significant amount of signal out of the voxel or ROI. Ramp sampling exacerbates the problem because the signal decays more rapidly in k-space. The broad point spread function due to these short relaxation times leads to an underestimation in signal, especially in the short bound water signal.

This signal loss can be accounted for analytically from the point spread function for one voxel, or by simulating the effect this would have on a particular geometry. The amount of signal loss depends on the geometry of the sample being imaged; geometries with greater widths and more voxels have less signal loss than geometries with fewer voxels, so it is

useful to compute this loss based on the geometry of the signal being measured. For 3D imaging of long bones, the samples are roughly invariant in the direction of the long axis of the bone, so the blurring effect can be neglected in that direction. Also, because the k-space sampling is radial, the point spread function can be solved in 1D (25,26), then applied in the 2D plane corresponding to the axial view of the bone.

For a known image geometry, T_2^*(s), and k-space trajectory, the signal attenuation can be numerically estimated as follows: i) a masked 2D bone image, $s(r)$ (bone signal = 1, all other signal equals 0) is Fourier transformed to produce the k-space signal, $S(k)$; ii), the effect of T_2^* decay during acquisition is imparted by multiplying $S(k)$ by $H(k)$, derived below; iii) the resulting apodized signal is inverse Fourier transformed to produce a blurred image, $sb(r)$; and iv) the signal loss term, β, is then computed on a voxel-by-voxel basis as $\beta = sb(r)/s(r)$.

The apodizing function, $H(k)$, is derived for a 2D radial acquisition as follows. The signal decay during acquisition as a function of time is

$$h(t) = e^{-\frac{1}{T_2^*}} \tag{2.5}$$

and k is a function of t by the relationship:

$$|k(t)| = \frac{\gamma}{2\pi} \int_0^t g(t')dt' \tag{2.6}$$

where γ is the gyromagnetic ratio and $g(t)$ is the gradient waveform. In this case, ramp sampling needs to be included in this calculation. Since we know $g(t)$ for both the ramp sampling case $(t < t_0)$ and after the ramp $(t \geq t_0)$, k can be solved for both during the ramp acquisition and after the ramp. Assuming that $g(t)$ increases linearly at constant slew rate up to max gradient amplitude, G, at time $t = t_0$, then,

$$
|k(t)| = \begin{cases} \frac{\gamma}{2\pi} \frac{Gt^2}{2t_0}, & t < t_0 \\ \frac{\gamma}{2\pi} G(t - t_0), & t \geq t_0 \end{cases}
\tag{2.7}
$$

Let $k_0 = k(t_0) = \frac{\gamma}{2\pi} Gt_0$, then

$$
t = \begin{cases} \sqrt{\frac{4\pi t_0 |k|}{\gamma G}}, & k < k_0 \\ \frac{2\pi |k|}{\gamma G} + \frac{t_0}{2}, & k \geq k_0 \end{cases}
\tag{2.8}
$$

Substituting 2.8 into Equation 2.5, we can solve for H as a function of k to give the apodizing function in k-space:

$$
H(k) = \begin{cases} e^{\frac{\sqrt{\frac{4\pi t_0 |k|}{\gamma G}}}{T_2^*}}, & |k| < k_0 \\ e^{\frac{\frac{2\pi |k|}{\gamma G} + \frac{t_0}{2}}{T_2^*}}, & |k| \geq k_0 \end{cases}
\tag{2.9}
$$

Now this point spread function can be applied to the k-space signal to estimate the signal decay in a known geometry. This is illustrated in Figure 2.5, where a masked bone slice (bone signal = 1, all other signal equals 0) is Fourier transformed, the resulting k-space is apodized by multiplying by $H(k)$ and then inverse Fourier transformed back to image space. The amount of signal loss, β, can be estimated by evaluating the percent decrease in signal in a particular region of interest (ROI).

2.3 Signal Quantification

The bound and pore water concentration can be mapped by quantifying the signal using the signal equations for these pulse sequences. The signal equations for DAFP and AIR measurements in cortical bone are shown below:

$$
S_{DAFP} \approx S_0^{pw} \beta^{pw} sin\theta_1 \frac{(\alpha^{pw})^2 (1 - e^{-R_1^{pw} TR})}{1 - (\alpha^{pw})^2 e^{-R_1^{pw} TR} cos\theta_E} e^{-R_2^{*pw} TE}
\tag{2.10}
$$

| Original Mask | Apodize K-space | Blurred Mask |

k . H(k)

FT   IFT
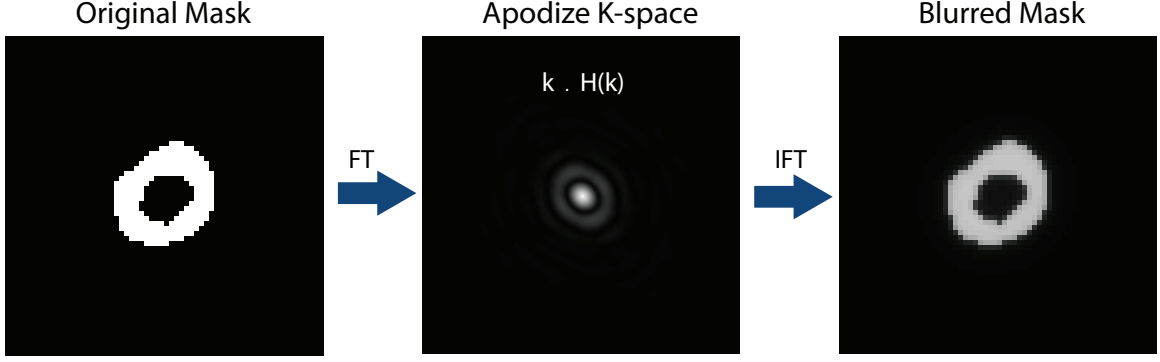
Figure 2.5: Estimated signal loss due to relaxation induced blurring. The masked 2D image of 1s and 0s is Fourier transformed to k-space, where the signal is multiplied by the point spread function and then inverse Fourier transformed back to image space. The resulting image shows the amount of signal lost, and β is calculated based on the region of interest.

and

$$S_{AIR} \approx S_0^{bw} \beta^{bw} sin\theta_1 \frac{1 - (1 - \alpha^{bw})e^{-R_1^{bw}TI} - \alpha^{bw}e^{-R_1^{bw}TR}}{1 - \alpha^{bw}e^{-R_1^{bw}TR}cos\theta_E}e^{-R_2^{*bw}TE}, \qquad (2.11)$$

where α is the inversion efficiency of the AFP pulse, β is the signal loss due to relaxation-induced blurring, S_0 is proportional to water concentration, and superscripts ^{pw} and ^{bw} indicate pore water and bound water, respectively. Replacing ^{pw} or ^{bw} with ^{ref} provides the signal equations for a reference marker for each sequence, imaged adjacent to the bone of interest. Thus, given the observed bone signals S_{DAFP} and S_{AIR}, the equilibrium signals, S_0^{pw} and S_0^{bw} were computed from each bone ROI or voxel using the DAFP and AIR signal equations above. These relative measures of proton density were then converted into absolute units of mol ^{1}H/L$_{bone}$ by comparison to corresponding values from the reference marker (S_0^{ref}), which had a known concentration.

By incorporating these solutions to the specific technical challenges that come with UTE imaging of cortical bone, we are able to use these DAFP and AIR imaging sequences to map pore and bound water concentrations, respectively. The following section shows an experimental validation of these imaging methods by comparing results to the previously

validated NMR methods in ex vivo bones.

2.4 Experimental Validation of Quantitative Bound and Pore Water Imaging Methods

Text for this section was taken from:

Manhard MK, Horch RA, Harkins KD, Gochberg DF, Nyman JS, Does MD. Validation of quantitative bound- and pore-water imaging in cortical bone. Magnetic Resonance in Medicine. 2014; 71(6):2166-71.

2.4.1 Introduction

Recent studies showed that ^{1}H NMR signals with short T_2 ($\approx 400\ \mu$s) correspond primarily to collagen-bound water and those with longer T_2 components (1 ms$-$1 s) correspond primarily to pore water [14]–[17]. These bound and pore water measures correlate to mechanical properties of bone, including yield stress, peak stress, and pre-yield or elastic toughness [6], [18]–[20]. In particular, bones with a greater concentration of bound water and a lower concentration of pore water have higher values of peak stress, yield stress, and pre-yield toughness. These results suggest that appropriate MRI methods that robustly distinguish and quantitatively measure bound- and pore-water concentrations in cortical bone may offer a viable methodology for predicting fracture risk. In particular, they can assess the contribution of the bone tissue to fracture resistance in addition to the structural contribution already provided by conventional MRI or X-ray computed tomography. This is potentially quite useful since clinical assessment of areal bone mineral density by dual-energy X-ray absorptiometry does not necessarily capture all the deleterious effects of aging and certain diseases (type 2 diabetes, chronic kidney disease) on fracture risk [21], [22].

Bi-exponential analysis of T_2^* signal decays has shown correlations between the fitted components amplitudes and the bound and pore water concentrations [2], [6], [23], [24].

This approach requires noise-sensitive non-linear regression and may be limited at high static field strengths by the similarity of T_2^* of bound and pore water [10], [16], [17]. An alternative approach uses T_2-selective adiabatic radiofrequency (RF) pulses over a broad enough resonance bandwidth to effectively distinguish bound- and pore-water signals [10]. Specifically, playing two consecutive broad-bandwidth adiabatic full passage pulses will drive short T_2 magnetization (bound water) to saturation while rotating long T_2 magnetization (pore water) through $360°$, leaving it essentially unaffected. This approach is referred to as the Double Adiabatic Full Passage (DAFP). To image bound water, a similar approach uses one adiabatic full passage pulse followed by an appropriate delay to invert and null pore water magnetization while the bound water magnetization experiences a saturation-recovery process. This approach is referred to as the Adiabatic Inversion Recovery (AIR). Presented here are demonstrations and validations of DAFP and AIR methods of imaging bound- and pore-water of human cadaver bones, using clinically practical parameters, on both a 4.7T small-bore and a 3.0T human system.

2.4.2 Methods

The Vanderbilt Donor Program supplied human femurs from three cadaveric donors, two males and one female, mean age 77 years. Mid-shaft sections of each bone were cut to ≈ 80 mm in length. Images of the femur mid-shafts along with a $CuSO_4$-doped 10% H_2O/90% D_2O phantom (in a 10 mm NMR tube adjacent to the bone) were acquired using the DAFP and AIR sequences, detailed below, with $96 \times 96 \times 96$ mm^3 field of view and a nominal isotropic resolution of 1.5 mm. After imaging, cylindrical cortical bone samples ($4-9$ mm length, 6 mm diameter) were cored from four radial locations near the middle of the mid-shaft. These samples, along with a long-T_2 water sample of known volume, were used to provide reference values of bound and pore water concentrations using a previously described CPMG protocol [10] at 4.7 T. Imaging at 3T was performed on a Philips Achieva (Best, NL) using their Knee 8ch receive coil and the body coil for

signal transmission. Measurements at 4.7 T were performed on an Agilent Direct Drive (Santa Clara, CA) using an in-house built 63-mm diameter low-proton birdcage style coil for whole bone imaging and an in-house built 20 mm diameter low-proton loop-gap style RF coil for CPMG measurements on isolated bone specimen [25].

2.4.2.1 Pulse Sequences

Figure 2.1 shows sequence diagrams of the DAFP and AIR sequences. In all cases, the following sequence parameters were used: radial sampling of k-space with 83 points at 250 kHz receiver bandwidth, acquisition time per spoke = 332 μs; a post-acquisition spoiler gradient 1.74 ms duration and 31 mT/m amplitude; repetition time per spoke (TR_A) = 3.18 ms; number of spokes per shot (N_S) = 16; total number of spokes = 8192; RF excitation pulse width = 115 μs. The radial spokes were distributed evenly over the k-space sphere [9]. A variable flip angle schedule was used for excitations in order to generate approximately constant transverse magnetization for all 16 spokes [13], with an initial prescribed flip angle, θ_1 = 12.5° and effective total flip angle, θ_E = 60° (i.e., longitudinal magnetization is reduced by $cos\theta_E$ by the combination of all 16 excitations). In all cases, the effective echo time (TE), as measured from the center of the RF excitation pulse to the start of acquisition, was 105.5 μs (4.7T) and 127.5 μs (3.0T).

The AIR sequence used a sequence repetition time (TR) = 300 ms, TI = 90ms/85ms (4.7T/3T), and a 10 ms duration, 3.5 kHz bandwidth, 8th ordered hyperbolic secant (HS8) pulse [26] as the preparation pulse. The DAFP sequence used TR = 400 ms, TD = 5 ms, and two consecutive HS8 pulses (20 ms total duration). The maximum gradient amplitudes and slew rates of the human system were also used on the 4.7T. The TR values for each sequence were dictated by FDA-defined RF power deposition limits on the 3.0T scanner. On the 4.7T system, one excitation provided sufficient signal, resulting in scan times of $\approx$ 3.5 min and $\approx$ 2.5 min for DAFP and AIR, respectively. On the 3.0T system, lower signal-to-noise ratio (SNR) dictated 4 averaged excitations ($\approx$ 13.5 m) for DAFP and 6 averaged

excitations ($\approx$ 20.5 m) for AIR to achieve SNR comparable to 4.7T.

In addition, a conventional UTE (CUTE) image was acquired for each bone at 3.0T and 4.7T, and at 4.7T a B_1 map was also acquired. The CUTE acquisition used TR/TE = 2.5 ms/62.5 μs and a 25 μs duration, 6° flip excitation pulse. The B_1 mapping was performed by the Bloch-Siegert method [27] with a multi-slice spin echo acquisition. Ten axial slices (3 mm thick/5 mm gap) spanned the length of the bone. The B_1 measured in the water phantom of each slice was used to determine the actual flip angle seen in each slice for analysis of AIR and DAFP data (see below). Variation of B_1 within the slice was independently determined to be < 2.5% for the coil used on the 4.7T. On the 3.0T, the body RF coil was used for transmission and was independently determined to vary in B_1 by < 4.5% over the entire bone volume, so no B_1 mapping was necessary.

2.4.2.2 Data Analysis

All data were analyzed using MATLAB (Natick, MA). Images were reconstructed using standard trajectory mapping, density compensation, and gridding methods [8]. Bound and pore water concentrations were computed on a voxel-by-voxel basis, then regions of interest (ROIs) were defined at the approximate locations from which the cylindrical bone samples were taken. The signal equations for DAFP and AIR measurements in cortical bone are shown in equations 2.10 and 2.11 on page 28.

At 4.7T, previously obtained values were used for inversion efficiency (α), T_1, and T_2^* of bound water, pore water, and the reference marker [10]: $\alpha^{bw/pw/ref}$ = 0.09/-0.78/-0.83, $T_1^{bw/pw/ref}$ = 357 ms/551 ms/13 ms, $T_2^{*bw/pw/ref}$ = 290 μs/1280 μs/13 ms. At 3.0T, T_{1pw} was estimated from one bone using a saturation-recovery fast spin echo acquisition, and T_1^{bw} was estimated to change similarly from 4.7T as did T_1^{pw}. T_2^* values at 3.0T were used as measured by Du et al. for ex vivo human cortical bone [24]. Because T_2 values were assumed to be nearly B_0 independent, the same α values were used at 3.0T as were previously measured at 4.7T. A summary of parameter values used at 3.0T were $\alpha^{bw/pw/ref}$

$= 0.09/-0.78/-0.83$, $T_1^{bw/pw/ref} = 290$ ms/450 ms/10 ms, $T_2^{*bw/pw/ref} = 350$ μs/2600 μs/10 ms.

The blurring-induced signal loss values (β) were empirically estimated by simulating the effect of blurring using the known bone geometry for each bone. Individual β values were found for each ROI and bone, but mean estimates used to create images were $\beta^{bw/pw}=$ 0.77/0.97 at 3.0 T and 0.74/0.93 at 4.7 T. In both cases, β^{ref} was defined $= 1.0$. Thus, given the observed bone signals S_{DAFP} and S_{AIR}, the equilibrium signals, S_0^{pw} and S_0^{bw} were computed from each bone ROI or voxel using Equations 2.11 and 2.10. These relative measures of proton density were then converted into absolute units of mol ^{1}H/L$_{bone}$ by comparison to corresponding values of S_0^{ref}, which were known to reflect 11.11 mol $^1H/L_{H_20}$.

The non-imaging data from the extracted cortical bone samples were analyzed by fitting CPMG echo amplitudes to a broad range of decaying exponential functions by non-negative least squares criteria subject to a minimum curvature constraint, resulting in a T_2-spectrum for each sample [16], [28]. The integrated T_2 spectrum amplitude over various domains provided signal amplitude measures for bound water (100 μs $< T_2 < 1$ ms), pore water (1 ms $< T_2 < 1$ s) and reference sample ($T_2 > 1$ s). The bound and pore water signals amplitudes were then converted into units of mol ^{1}H/L$_{bone}$ by comparison with the reference signal amplitude and known volumes of the bone and reference samples, and the known proton concentration of water.

2.4.3 Results

Figure 2.6 shows approximately the same slice taken from 3D bound- and pore-water images of one bone at 3T and 4.7T. The gray scale images are CUTE images; color overlaid images are the bound or pore water concentration maps generated from the respective method. The DAFP image shows consistently a higher concentration of pore water in the posterior section of the femur, which agrees with previous findings [19], [29], and in general there is an apparent negative correlation between the spatial distribution of bound and

pore water, as expected. The signal to noise ratio (SNR) of DAFP/AIR images were 27/22 at 4.7T and 26/28 at 3.0T, defined as

$$SNR = \mu_S/(\mu_N/\sqrt{\pi/2}) \tag{2.12}$$

where μ_S and μ_N are mean signal in a region of cortical bone and background noise, respectively. (At 3.0T, the background of the AIR images showed significant signal from the foam used to hold the bone samples, so for this μ_N measure one scan was repeated with a larger FOV but equal voxel size and receiver bandwidth.) The RF coil used at 3.0T is suitable for wrist and lower leg imaging, so these SNR values should be predictive of in vivo scans of the radius and tibia.

Figure 2.7 shows a representative T_2 spectrum from an extracted cortical bone sample, with the bound water, pore water, and water marker signals labeled. Figure 2.8 shows linear correlations between bound/pore water concentrations measures from the extracted samples and those from the AIR and DAFP images at approximate locations of the extracted bone samples (shown by red squares on inset image). Coefficients of determination for pore water concentrations were $r^2 = 0.41$ at 3T and $r^2 = 0.94$ at 4.7T; for bound water concentrations they were $r^2 = 0.76$ at 3T and $r^2 = 0.55$ at 4.7T.

2.4.4 Discussion

The magnetization preparations used in the AIR and DAFP pulse sequences were previously demonstrated to effectively distinguish bound and pore water signals in isolated human cortical bone samples [10]. Presented here is the translation of these methods into clinically practical MRI protocols, and the quantitative evaluation of these MRI protocols on human cadaver bones at 3.0 and 4.7 T. The results suggest that the AIR and DAFP methods are effective for quantitative imaging of bound and pore water, respectively, but there are numerous factors that may affect their performance and utility.
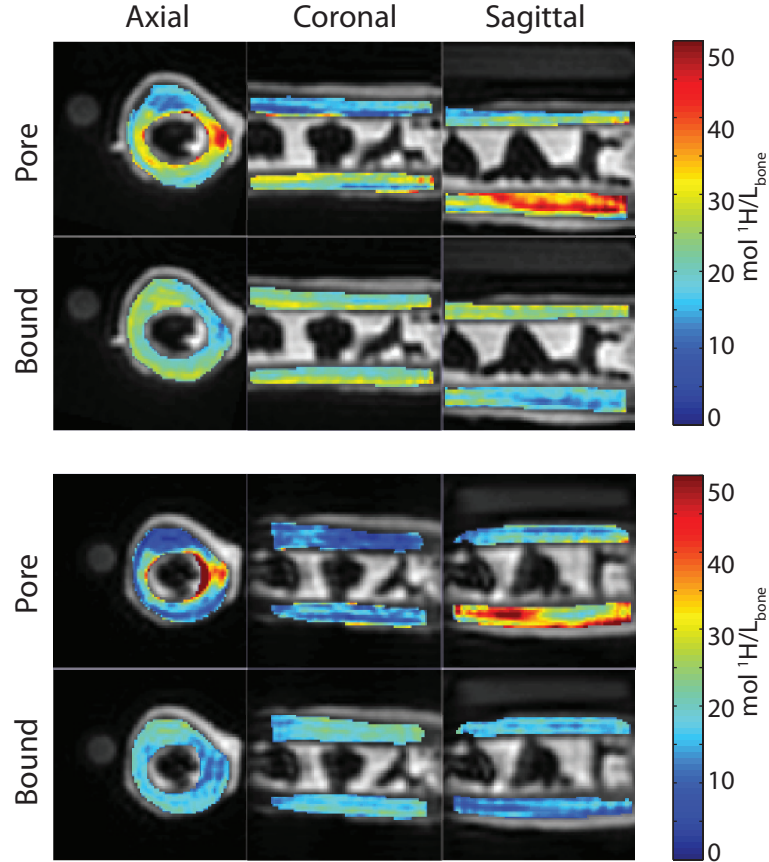
Figure 2.6: Imaging results from 3.0 T (top) and 4.7 T (bottom) of the DAFP and AIR sequences showing three cardinal planes of pore and bound water maps. Note the negative correlation between bound and pore water throughout the bone volume and the higher concentration of pore water in the posterior section of the femur.

First, in contrast to previous non-localized studies of isolated bone samples, the imaging protocols presented here required accelerated acquisition to achieve scan times amenable to human studies. Power deposition from the AFP pulses set the lower limit on TR, so additional acceleration was achieved by acquiring $N_S =16$ radial spokes in k-space per TR period, similar to a conventional MP-RAGE protocol [12]. The 3D radial trajectory sampled the k-space origin with every radial spoke, so accurate quantitation of image intensity required a variable excitation flip angle schedule that generated approximately the same amplitude of transverse magnetization for each spoke [13]. Increasing N_S requires reduced flip angles, resulting in $SNR \propto 1/\sqrt{N_S}$, so the choice of N_S depends on the SNR and scan
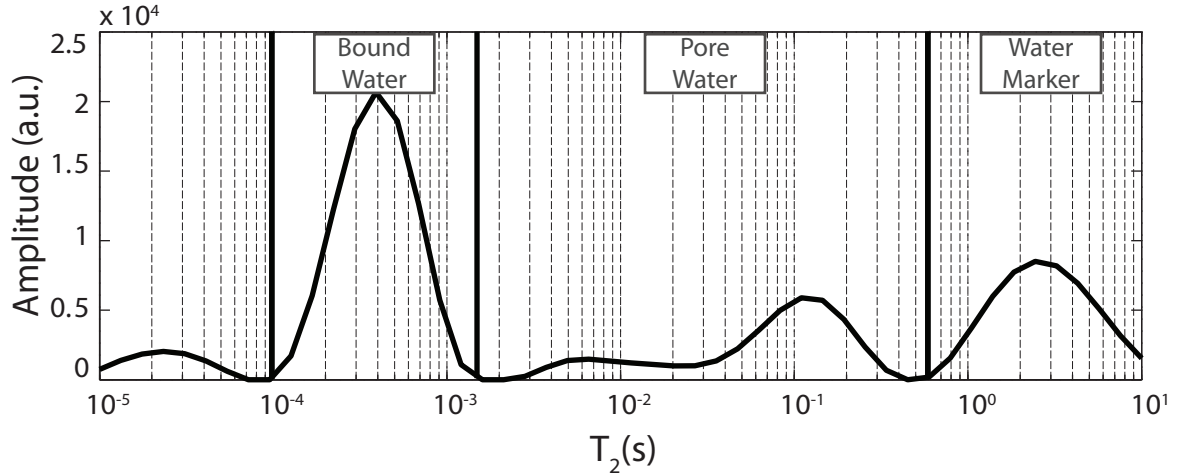
Figure 2.7: A representative T_2 spectrum from the CPMG measurements of the cored samples of cortical bone showing signals from bound water, pore water, and the water marker. The amount of bound and pore water was converted into units of mol $^1H/L$ based on the known size and concentration of the water marker.

time requirements. The choice of N_S may also affect signal accuracy, because each spoke experiences slightly different magnetization preparation. For the AIR sequence, each of the N_S spokes is acquired at a different TI and, therefore, includes a varying amount of non-nulled pore water signal. As long as the net pore water signal across the N_S spokes is zero, this is not a problem, but increasing N_S will likely result in greater net pore water signal. For the DAFP sequence, the recovery of bound water magnetization will grow with each spoke, so $N_S \times TR_A$ should be kept small compared to T_1 of bound water.

In addition to accelerated acquisition, practical use of the AIR and DAFP protocols depends upon having good estimates of a number of parameters in the signal equations, 2.11 and 2.10. As done here for scans on the 4.7T, it is relatively quick and easy to map B_1, thereby providing good estimates of θ_1 and θ_E on a case-by-case basis. However, estimates of bound- and pore-water relaxation rates may not be readily acquired during a clinical protocol, so good population estimates are needed. The values used here and in a previous study [10] of a small sample of cadaver bones have been sufficient to demonstrate
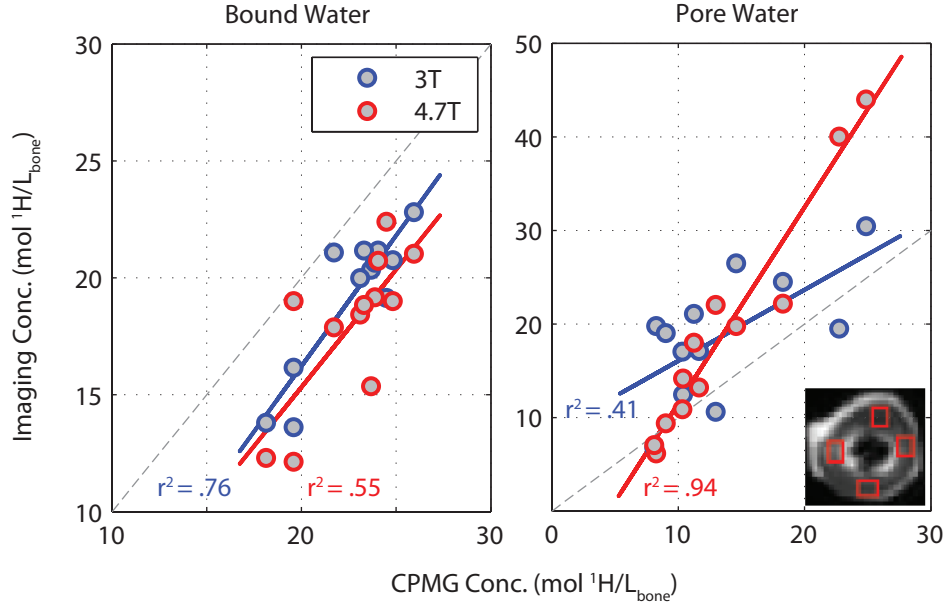
Figure 2.8: Concentrations from CPMG measurements versus DAFP and AIR results at approximate ROI locations from 3 T and 4.7T images of a) bound water and b) pore water. Both 3 T and 4.7 T imaging measurements showed strong linear correlations with CPMG measurements. Differences in correlation coefficients between 3 T and 4.7 T are most likely due to the small sample size, though its possible that differences in T_2 and T_2^* between 3 T and 4.7 T also could affect correlations, especially since these were not measured at 3 T but only estimated from other studies.

efficacy of the AIR and DAFP methods, but it is likely that errors in these values underlie the systematic deviations between the imaging and CPMG measures seen in Figure 2.8. Given the parameters used in this work, an error of 10% in T_1 results in a 5/8% error of DAFP/AIR signal, while a 10% error in T_2^* gives a 1/4% error of DAFP/AIR signal. Further, it may not be suitable to describe T_1 and T_2^* with scalar values. In particular, pore water likely consists of a relatively broad spectrum of T_1 values due to the variation in pore sizes within the bone [15], [16], which likely explains why TI must be empirically set to null the net pore water magnetization rather that by calculation from the estimated T_{1pw} [10].

Two parameters that are known but require special attention for accurate AIR and DAFP

measures are TE and receiver bandwidth. Although it is common to define TE from the end of the RF excitation pulse, the effect of relaxation during the RF pulse must be incorporated to ensure accurate measures. For hard pulse 3D UTE, as used here, transverse relaxation can be effectively accounted for by measuring TE from the middle of the RF pulse rather than the end [30]. Accounting for transverse relaxation during the acquisition is a somewhat more complicated problem. Because the bound water T_2^* is similar to the acquisition duration (332 μs), its relatively broad point spread function results in an underestimation of bound water signal compared to signal from the long T_2 water reference [31], [32]. In the present studies, as noted in the Methods, the bound and pore water signal losses was empirically estimated, which resulted in the $\beta^{bw/pw/ref} = 0.77/0.97/1.0$ at 3.0 T and 0.74/0.93/1.0 at 4.7 T.

2.4.5 Conclusion

These studies demonstrate the translation of previously developed approaches for distinguishing bound and pore water from human cortical bone. The methods, referred to AIR and DAFP here, were implemented as part of 3D UTE pulse sequences, subject to the practical human MRI constraints of gradient performance and RF power deposition. The results showed good correlation between these imaging measures of bound and pore water and those determined by previously established non-localized CPMG measures.

2.5 References

[1] M. D. Robson, P. D. Gatehouse, M. Bydder, and G. M. Bydder, "Magnetic resonance: an introduction to ultrashort te (ute) imaging," *J Comput Assist Tomo*, vol. 27, no. 6, pp. 825–846, 2003.

[2] E. Diaz, C. B. Chung, W. C. Bae, S. Statum, R. Znamirowski, G. M. Bydder, and J. Du, "Ultrashort echo time spectroscopic imaging (utesi): an efficient method for quantifying bound and free water.," *NMR Biomed*, vol. 25, no. 1, pp. 161–8, Jan. 2012.

[3] A. Techawiboonwong, H. K. Song, and F. W. Wehrli, "In vivo mri of submillisecond t 2 species with two-dimensional and three-dimensional radial sequences and applications to the measurement of cortical bone water," *NMR Biomed*, vol. 21, pp. 59–70, 2008.

[4] A. Techawiboonwong, H. K. Song, M. B. Leonard, and F. W. Wehrli, "Cortical bone water: in vivo quantification with ultrashort echo-time mr imaging," *Radiology*, vol. 248, no. 3, pp. 824–833, 2008.

[5] J. Du, M. Carl, M. Bydder, A. Takahashi, C. B. Chung, and G. M. Bydder, "Qualitative and quantitative ultrashort echo time (ute) imaging of cortical bone," *J Magn Reson*, vol. 207, no. 2, pp. 304–11, Dec. 2010.

[6] W. C. Bae, P. C. Chen, C. B. Chung, K. Masuda, D. D'Lima, and J. Du, "Quantitative ultrashort echo time (ute) mri of human cortical bone: correlation with porosity and biomechanical properties.," *J Bone Miner Res*, vol. 27, no. 4, pp. 848–57, Apr. 2012.

[7] H. S. Rad, S. C. B. Lam, J. F. Magland, H. Ong, C. Li, H. K. Song, J. Love, and F. W. Wehrli, "Quantifying cortical bone water in vivo by three-dimensional ultrashort echo-time mri.," *NMR Biomed*, vol. 24, no. 7, pp. 855–64, Aug. 2011.

[8] N. R. Zwart, K. O. Johnson, and J. G. Pipe, "Efficient sample density estimation by combining gridding and an optimized kernel.," *Magn Reson Med*, vol. 67, no. 3, pp. 701–10, Mar. 2012.

[9] S. T. S. Wong and M. S. Roos, "A strategy for sampling on a sphere applied to 3d selective rf pulse design," *Magn Reson Med*, vol. 32, no. 6, pp. 778–784, Dec. 1994.

[10] R. A. Horch, D. F. Gochberg, J. S. Nyman, and M. D. Does, "Clinically compatible mri strategies for discriminating bound and pore water in cortical bone.," *Magn Reson Med*, vol. 68, no. 6, pp. 1774–84, Dec. 2012.

[11] J. H. Duyn, Y. Yang, J. a. Frank, and J. W. van der Veen, "Simple correction method for k-space trajectory deviations in mri.," *J Magn Reson*, vol. 132, no. 1, pp. 150–3, May 1998.

[12] J. P. Mugler and J. R. Brookeman, "Three-dimensional magnetization-prepared rapid gradient-echo imaging (3d mp rage).," *Magn Reson Med*, vol. 15, no. 1, pp. 152–7, Jul. 1990.

[13] E. M. Haacke, R. W. Brown, M. R. Thompson, and R. Venkatesan, *Magnetic Resonance Imaging - Physical Principles and Sequence Design*. 1999, pp. 463–465.

[14] P. Fantazzini, R. J. S. Brown, and G. C. Borgia, "Bone tissue and porous media: common features and differences studied by nmr relaxation," *Magn Reson Img*, vol. 21, no. 3-4, pp. 227–234, Apr. 2003.

[15] Q. Ni, J. S. Nyman, X. Wang, A. D. L. Santos, and D. P. Nicolella, "Assessment of water distribution changes in human cortical bone by nuclear magnetic resonance," *Measurement Science and Technology*, vol. 18, no. 3, pp. 715–723, Mar. 2007.

[16] R. A. Horch, J. S. Nyman, D. F. Gochberg, R. D. Dortch, and M. D. Does, "Characterization of 1h nmr signal in human cortical bone for magnetic resonance imaging.," *Magn Reson Med*, vol. 64, no. 3, pp. 680–7, Sep. 2010.

[17] H. H. Ong, A. C. Wright, and F. W. Wehrli, "Deuterium nuclear magnetic resonance unambiguously quantifies pore and collagen-bound water in cortical bone.," *J Bone Miner Res*, vol. 27, no. 12, pp. 2573–2581, Jul. 2012.

[18] J. S. Nyman, Q. Ni, D. P. Nicolella, and X. Wang, "Measurements of mobile and bound water by nuclear magnetic resonance correlate with mechanical properties of bone.," *Bone*, vol. 42, no. 1, pp. 193–9, Jan. 2008.

[19] M. A. Fernández-Seara, S. L. Wehrli, M. Takahashi, and F. W. Wehrli, "Water content measured by proton-deuteron exchange nmr predicts bone mineral density and mechanical properties.," *J Bone Miner Res*, vol. 19, no. 2, pp. 289–96, Feb. 2004.

[20] R. A. Horch, D. F. Gochberg, J. S. Nyman, and M. D. Does, "Non-invasive predictors of human cortical bone mechanical properties: t(2)-discriminated h nmr compared with high resolution x-ray.," *PloS one*, vol. 6, no. 1, e16359, Jan. 2011.

[21] J. Kanis, O. Johnell, A. Oden, A. Dawson, C. De Laet, and B. Jonsson, "Ten year probabilities of osteoporotic fractures according to bmd and diagnostic thresholds," *Osteoporosis Int.*, vol. 12, no. 12, pp. 989–995, 2001.

[22] P. Vestergaard, "Discrepancies in bone mineral density and fracture risk in patients with type 1 and type 2 diabetes–a meta-analysis.," *Osteopros Int*, vol. 18, no. 4, pp. 427–44, Apr. 2007.

[23] J. Du, E. Diaz, M. Carl, W. Bae, C. B. Chung, and G. M. Bydder, "Ultrashort echo time imaging with bicomponent analysis," *Magn Reson Med*, vol. 67, no. 3, pp. 645–9, Mar. 2012.

[24] J. Du, J. C. Hermida, E. Diaz, J. Corbeil, R. Znamirowski, D. D. D'Lima, and G. M. Bydder, "Assessment of cortical bone with clinical and ultrashort echo time sequences.," *Magn Reson Med*, vol. 70, pp. 697–704, Sep. 2013.

[25] R. A. Horch, K. Wilkens, D. F. Gochberg, and M. D. Does, "Rf coil considerations for short-t2 mri.," *Magnetic resonance in medicine : Official journal of the Society of Magnetic Resonance in Medicine / Society of Magnetic Resonance in Medicine*, vol. 64, no. 6, pp. 1652–7, Dec. 2010.

[26] M. Garwood, "Improved performance of frequency-swept pulses using offset-independent adiabaticity," *J Magn Reson*, vol. 120, pp. 133–137, 1996.

[27] L. I. Sacolick, F. Wiesinger, I. Hancu, and M. W. Vogel, "B1 mapping by bloch-siegert shift.," *Magn Reson Med*, vol. 63, no. 5, pp. 1315–22, May 2010.

[28] K. P. Whittall and A. L. MacKay, "Quantitative interpretation of nmr relaxation data," *J Magn Reson*, vol. 84, no. 1, pp. 134–152, Aug. 1989.

[29] J. D. Currey, K. Brear, and P. Zioupos, "The effects of ageing and changes in mineral content in degrading the toughness of human femora," *J Biomech*, vol. 29, no. 2, pp. 257–260, 1996.

[30] M. D. Robson and P. D. Gatehouse, "Consequences of t2 relaxation during half-pulse slice selection for ultrashort te imaging.," *Magn Reson Med*, vol. 64, no. 2, pp. 610–5, Aug. 2010.

[31] J. Rahmer, P. Börnert, J. Groen, and C. Bos, "Three-dimensional radial ultrashort echo-time imaging with t2 adapted sampling.," *Magn Reson Med*, vol. 55, no. 5, pp. 1075–82, May 2006.

[32] M. Carl and J.-T. A. Chiang, "Investigations of the origin of phase differences seen with ultrashort te imaging of short t2 meniscal tissue.," *Magn Reson Med*, vol. 67, no. 4, pp. 991–1003, Apr. 2012.

Chapter 3

Assessing Repeatability of In Vivo Quantitative Magnetic Resonance Imaging of Bound and Pore Water in Cortical Bone

Text for this section was taken from:

Manhard MK, Horch RA, Gochberg DF, Nyman JS, Does MD. In Vivo Quantitative Magnetic Resonance Imaging of Bound and Pore Water in Cortical Bone. Radiology 2015; 277(1):221-29.

3.1   Introduction

Fragility fractures are an increasingly prevalent challenge in health care, and the number of fractures continues to increase with the rapidly growing elderly population [1]. The current standard for diagnosing fracture risk comprises measurements of bone mineral density (BMD), primarily by dual-energy X-ray absorptiometry (DXA). However, bone health and fracture risk depend on many factors other than BMD, such as architecture, collagen integrity, and cortical porosity. In addition, clinical risk factors such as age, previous fracture, family history, and use of corticosteroids can affect the fracture resistance of bone [2]. Several methods have been developed to improve fracture risk assessment [3], such as quantitative ultrasound of bone that reflects material information [4-6], quantitative computed tomography (QCT) to measure trabecular volumetric bone density and cortical structure [7-9], or the web-based Fracture Risk Assessment Tool (FRAX) to account for clinical risk factors in addition to BMD measurements [10,11]. In previous work, there has been substantial progress in MRI methods for the evaluation of bone [12-15].

Through a variety of ^{1}H NMR studies on ex vivo cortical bone samples, the contributions and relaxation characteristics of signals from water in pores and water bound to the collagen matrix have been characterized [16,17]. NMR signals of short T_2 (≈ 400 μs) are

due to collagen bound water, and signals of longer T_2 (1 ms–1 s) are primarily due to pore water. In similar samples, the bound and pore water ^{1}H NMR signal amplitudes have been shown to correlate with mechanical properties, including yield stress, peak stress, and elastic toughness [18-20]. Bone specimens with a greater concentration of bound water tend to have high values of peak and yield stress and elastic toughness, where as specimens with a greater concentration of pore water are generally associated with higher porosity and lower peak stress, yield stress, and toughness. However, it is necessary to distinguish between the bound and pore water signals, since their sum has little or no relationship to mechanical properties [20].

Bound and pore water signals can be discriminated based on relaxation times using wide-bandwidth T_2-selective adiabatic radiofrequency (RF) pulses [21]. Using these pulses in conjunction with an ultra-short echo time (UTE) acquisition allows for imaging of bound and pore water signal [22]. The Double Adiabatic Full Passage (DAFP) sequence uses two consecutive adiabatic RF pulses to suppress bound water signals while retaining pore water magnetization to near its sequence equilibrium state. The Adiabatic Inversion Recovery (AIR) sequence uses a single adiabatic RF pulse followed by an appropriate delay (TI) to selectively null pore water magnetization while allowing bound water magnetization to return to near its equilibrium state. In both cases, longitudinal magnetization is excited by a hard RF pulse immediately following the magnetization preparation, resulting in a signal that is primarily pore water or bound water, respectively, for the DAFP and AIR sequences. The pulse sequence diagram for these sequences can be seen in Figure 2.1. Signal equations and a more detailed description of these methods can be found in prior works [21,22].

These sequences have previously been validated on whole human cadaveric bones on a clinical 3.0T system against non-localized measures of small bone specimens extracted from the whole bones [22]. The purpose of our study is to translate and evaluate an in-vivo MRI protocol for quantitative mapping of collagen-bound and pore water concentrations in cortical bone using relaxation-selective ultra-short echo time (UTE) methods.

3.2 Methods

3.2.1 Subjects

All studies were compliant with the Health Insurance Portability and Accountability Act, were approved by the institutional review board, and included written informed consent. Eligible volunteers included 20-80 y.o. healthy adults. Exclusion criteria included subjects with non-MRI compatible bioimplants or cerebral aneurysm clips, subjects who may have had shrapnel imbedded in their bodies, subjects younger than 20 years old, pregnant women, and subjects with a history of fragility fracture, cancer, chronic steroid use, osteogenesis imperfecta, Pagets disease or other congenital bone disease, diabetes, bisphosphonate use, medical contraindication to MRI, and drug or alcohol abuse. The wrist from five healthy volunteer subjects (31, 23, 25, 24, 26 y.o., 2 male and 3 female) and lower leg from five healthy volunteer subjects (24, 24, 49, 30, 26 y.o., 2 male and 3 female) were imaged three times each, no more than 5 weeks between scans. The subjects were consented between August 2013 and August 2014.

3.2.2 Imaging Protocol

Using a Philips (Best, NL) Achieva 3T scanner, leg scans were acquired with 1.5 mm nominal isotropic resolution using a Knee 8 channel receive coil and the body coil for signal transmission. Wrist scans were acquired with 1.2 mm nominal isotropic resolution using a Wrist 8 channel receive coil and body coil for signal transmission. Wrist scans were acquired with the volunteer lying in the prone position and the arm extended above the head. A short-T_2 reference phantom (CuSO$_4$-doped 10% H$_2$O/90% D$_2$O in a 10 mm NMR tube) in the field of view was used to convert signal intensity into absolute units of concentration (mol ^{1}H/L$_{bone}$). Another pair of reference phantoms with longer T_2s were used in measuring the relative receive field in the first phantom, as described below.

Bound and pore water maps were generated using the AIR and DAFP sequences, re-

spectively, and a conventional UTE scan was acquired for anatomical reference. All scans including positioning for both the tibia and the radius took approximately one hour. The following sequence parameters were used for the AIR sequence: repetition time (TR) = 400 ms, inversion time (TI) = 85 ms, and adiabatic inversion by a 10 ms duration, 3.5 kHz bandwidth, 8th ordered hyperbolic secant (HS8) pulse. The DAFP sequence used TR = 615/400 ms (wrist/leg), TD = 5 ms, and two consecutive HS8 pulses. Signal acquisition for DAFP and AIR scans was accomplished by acquiring 124/171 (wrist/leg) samples along each of 20000/33792 (wrist/leg) radial half-spokes in k-space. Scans were accelerated by acquiring N_S = 16 spokes per magnetization preparation (Figure 2.1), with a 3.18 ms repetition time per spoke, resulting in scan times of approximately 8/12 min AIR/DAFP on the wrist and 14 min for each scan on the leg. Magnetization was excited with a 115 μs duration hard RF pulses and a variable flip angle schedule (initial prescribed flip angle, θ_1 = 12.5°, effective total flip angle, θ_E = 60°) to generate approximately constant transverse magnetization for all 16 spokes [23]. The effective echo time (TE), as measured from the center of the RF excitation pulse to the start of acquisition, was 127.5 μs. The conventional UTE image acquired for each scan used TR = 2.5 ms, TE = 62.5 μs and a 25 μs duration, 6° flip excitation pulse. Maximum gradient amplitudes and slew rates of the system were used on all scans. The TR values were dictated by FDA-defined RF power deposition limits.

The receive-coil sensitivity map was characterized by computing the ratio of two low-resolution T_1-weighted images (TR = 447 ms, TE = 26 ms, 2 × 2 × 6 mm voxel size) using the knee coil for receiving on the first scan and the body coil for receiving on the second scan. Because the signal in the cortical bone region was very low in these T_1-weighted images due to the longer TE, the sensitivity map was smoothed using map values from surrounding voxels within an apodized 11 x 11 window. The signal in the short-T_2 reference phantom was also low in the sensitivity maps, so the sensitivity for this phantom was estimated from the mean relative sensitivity of two longer T_2 reference phantoms placed on either side of the short-T_2 phantom.

3.2.3 Image Analysis

Images were reconstructed using standard Philips base code or, for data acquired after a system hardware repair and gradient recalibration, offline using measured gradient trajectories [24] and standard density compensation and gridding methods [25]. Bound and pore water concentrations were computed on a voxel-by-voxel basis using signal equations in Ref. [22] and converted to absolute units of water equivalent concentration using the reference marker signal, which had a known concentration of 11.11 mol ^{1}H/L$_{bone}$. The blurring-induced signal loss that results from having signal with a T_2^* approximately equal to the radial acquisition time was empirically estimated by simulating the effect of blurring using the bone geometry (details in [22]). In the signal equations, for bound and pore water, respectively, T_1 was defined as 290 ms and 450 ms [22], and T_2^* as 350 μs and 2600 μs [26].

3.2.4 Statistical Analysis

For ease of manually defining regions of interest (ROIs), images were up-sampled by a factor of two using bi-cubic interpolation and ROIs were chosen by a single observer using anatomical landmarks. The size of each ROI was 12/6 voxels in slice for the tibia/radius, through 4.5 mm slice thickness. In both the tibia and the radius, the ROIs were chosen close to the mid point of the diaphysis. Keeping the distance from the distal end of the radius or tibia to the center of the FOV constant between repeated scans ensured consistency in location. Examples of ROI locations are shown in Figure 3.1. There were three ROIs in the tibia corresponding to the anterior, medial, and posterior part of the cortical bone. Two ROIs were defined in the medial and lateral parts of the radius. Voxels near the edge of the bone were avoided to minimize partial volume effects.

The standard deviation (SD) of image noise per voxel was measured as the from a background region prior to upsampling the image, and the SDs of the bound and pore water

Figure 3.1: Example ROI locations in the tibia (top) and wrist (bottom). ROIs were 3-6 voxels within the axial slice, through 3 slices.

concentrations was then computed from this value by propagation of error. The per voxel signal-to-noise ratio (SNR) was defined as the bound or pore water concentration within the cortical bone divided by the computed SD of the bound or pore water concentration. Inter-scan variability was evaluated for each subject and ROI as the SD of the ROI means across three repeated scans. With the assumption that inter-scan variability is independent of subject and ROI, the pooled SD was also computed for each protocol (DAFP/AIR and tibia/radius).

3.3   Results

To demonstrate general image quality, Figure 3.2 shows representative raw magnitude image slices of the leg of one subject using all the three UTE protocols – conventional UTE, AIR, and DAFP protocols; wrist images looked similar. The bone tissue signal in the conventional UTE and DAFP images look dark compared to surrounding tissue because of the difference in proton density between bone and fat or muscle, but the signal in the bone was above the noise in all cases.

Bound and pore water maps from all five subjects are presented quantitatively in Figures 3.3 and 3.4.

Figure 3.3 shows representative slices of bound and pore water maps in the tibia overlaid on conventional UTE images. Figure 3.4 shows similar images of the wrist with bound
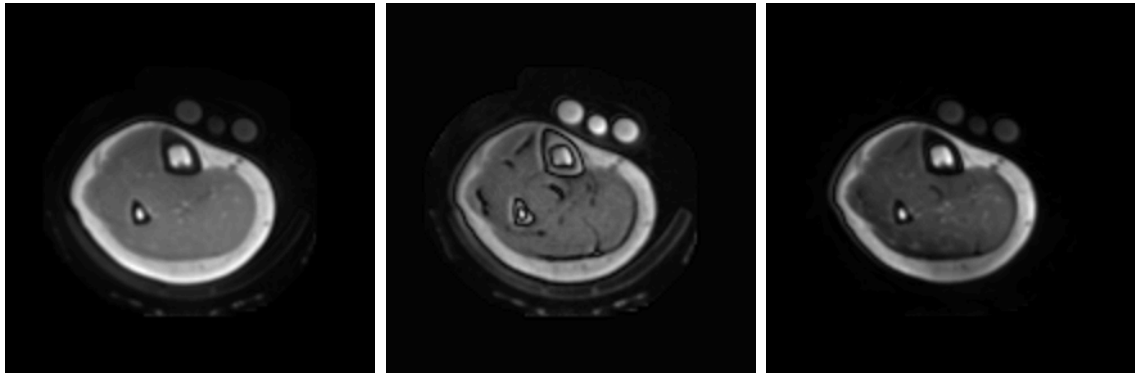
Figure 3.2: Slice of the raw lower leg image for one representative subject, showing conventional UTE (left), AIR (middle), and DAFP (right).
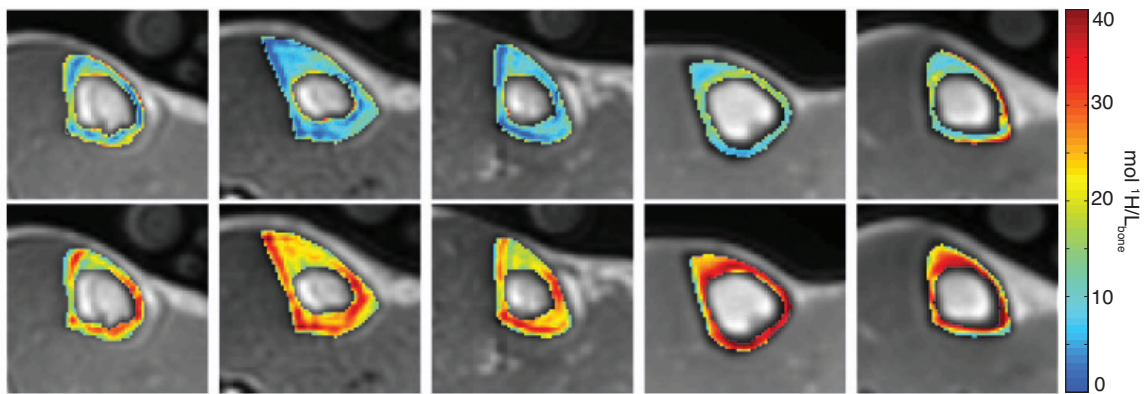
Figure 3.3: Slice of the lower leg image for all five subjects;images shown are from a conventional UTE image with the bound (bottom) and pore (top) water maps in the tibia overlaid.
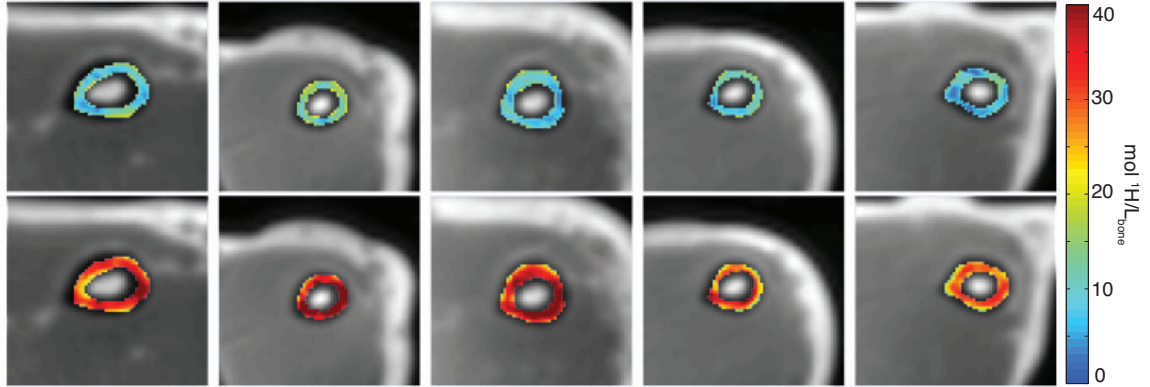
Figure 3.4: Slice of the wrist image for all five subjects; images shown are from a conventional UTE image with the bound (bottom) and pore (top) water maps in the radius overlaid.

and pore water maps overlaid on the radius. Across subjects and repeated scans, the mean per-voxel SD of the bound and pore water maps was 1.39 mol ^{1}H/L$_{bone}$ and 0.74 mol ^{1}H/L$_{bone}$, respectively, and was approximately equal for tibia and radius scans. Correspondingly, the per-voxel SNR was ≈ 20 for bound water maps and ≈ 10 for pore water maps. The repeatability of the parameter maps can be qualitatively assessed from Figure 3.5, which shows maps from the three repeated scans from one subject in tibia and one subject in the wrist.
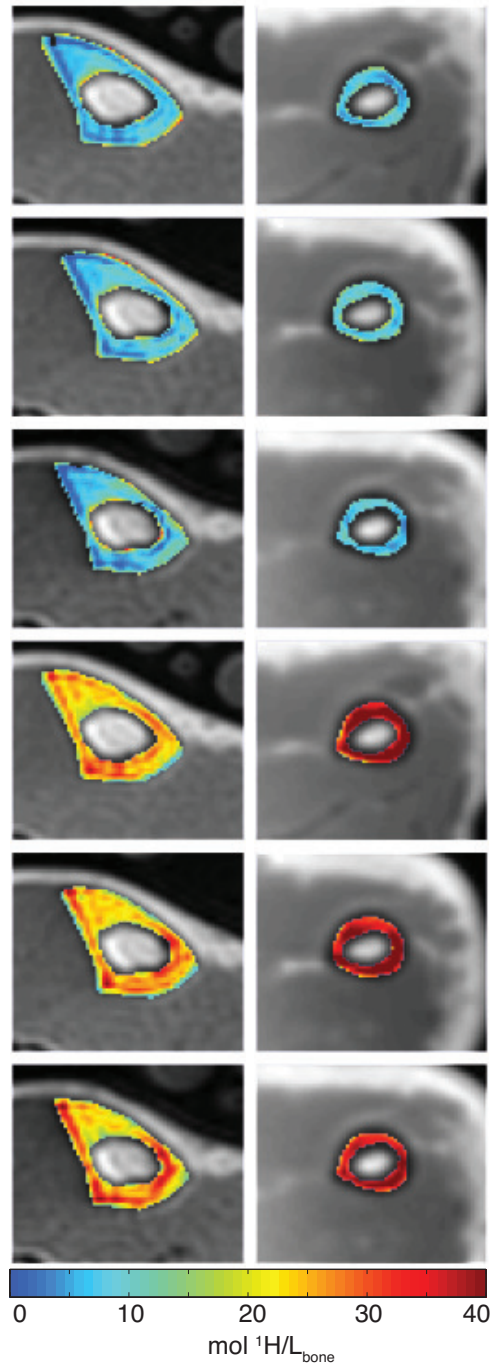
Figure 3.5: Representative image from one tibia subject and one radius subject showing a conventional UTE image with bound (bottom) and pore (top) water maps overlaid for three repeated scans.

A quantitative evaluation of mean bound and pore water concentrations among the 3 imaging sessions per subject with inter-scan variability of signals are shown in Tables 3.1

Table 3.1: Inter-scan means and standard deviations in the tibia.

| | Bound Water | | Pore Water | |
	Mean (mol^1H/L_{bone})	SD (mol^1H/L_{bone})	Mean (mol^1H/L_{bone})	SD (mol^1H/L_{bone})
Subject 1				
ROI 1	28.61	1.37	2.86	0.41
ROI 2	23.28	0.36	8.59	1.53
ROI 3	25.70	0.58	11.3	2.17
Subject 2				
ROI 1	23.11	0.75	5.53	0.07
ROI 2	29.93	1.54	3.47	0.34
ROI 3	26.45	1.98	8.99	0.76
Subject 3				
ROI 1	18.57	1.96	9.24	0.83
ROI 2	32.14	1.61	1.85	0.59
ROI 3	25.10	1.92	7.43	0.78
Subject 4				
ROI 1	24.05	0.53	8.56	1.29
ROI 2	31.67	1.43	6.53	1
ROI 3	32.57	1.74	10.34	2.23
Subject 5				
ROI 1	27.74	3.14	8.1	0.79
ROI 2	31.93	4.14	8.74	0.7
ROI 3	36.98	2.92	8.23	1.22
Mean	27.86	2.00*	7.32	1.15*

*pooled standard deviation across all subjects and ROIs

and 3.2 and summarized in Figure 3.6.

In the tibia and the radius, bound water concentrations were $\approx$ 28 and 35 mol ^{1}H/L$_{bone}$, respectively, and corresponding pore water concentrations were $\approx$ 7 and 6 mol ^{1}H/L$_{bone}$. These values were similar to previous ex vivo observations from the femur [22]. The bound and pore water are generally inversely correlated, especially in the larger anterior section of the tibia. As expected, the healthy subjects in this study had relatively high bound water and low pore water concentrations. Tabulated for each ROI, the inter-scan SD in ROI means (Tables 3.1 and 3.2, and error bars in Figure 3.6) were generally similar in magnitude with mean (range) = 1.93 (0.07-4.1) mol ^{1}H/L$_{bone}$. Given the ROI sizes, these inter-scan variations were generally greater than expected from intrinsic noise levels alone (above),

Table 3.2: Inter-scan means and standard deviations in the radius.

| | Bound Water | | Pore Water | |
	Mean (mol^1H/L_{bone})	SD (mol^1H/L_{bone})	Mean (mol^1H/L_{bone})	SD (mol^1H/L_{bone})
Subject 1				
ROI 1	28.65	0.49	4.23	1.12
ROI 2	28.99	2.51	6.37	0.45
Subject 2				
ROI 1	42.97	1.91	6.33	2.67
ROI 2	34.13	0.69	6.72	3.55
Subject 3				
ROI 1	37.53	1.28	6.2	1.93
ROI 2	40.87	3.01	5.09	1.38
Subject 4				
ROI 1	33.93	3.56	4.52	0.44
ROI 2	35.38	3.8	12.87	2.52
Subject 5				
ROI 1	32.33	3.37	5.01	1.83
ROI 2	33.79	2.72	4.07	1.41
Mean	34.86	2.59*	6.14	1.97*

*pooled standard deviation across all subjects and ROIs

indicating some systematic variation from scan to scan, causes of which are discussed below.

3.4 Discussion

The DAFP and AIR methods of measuring bound and pore water concentrations, respectively, in cortical bone were demonstrated in vivo in radius and tibia. The radius and the tibia are excellent sites for imaging with MR because of their size and accessibility for coils; additionally imaging measures from these bones have been shown to be associated with fracture risk [3]. These methods have no ionizing radiation and allow for new quantitative measures that are known to reflect material properties of bone [18–20]. In particular, bound water is not detectable with conventional bone imaging methods, but is indirectly a marker of collagen matrix integrity and has shown correlations with toughness of bone [19,20]. Low bound water measures could account for the disproportionate increase in
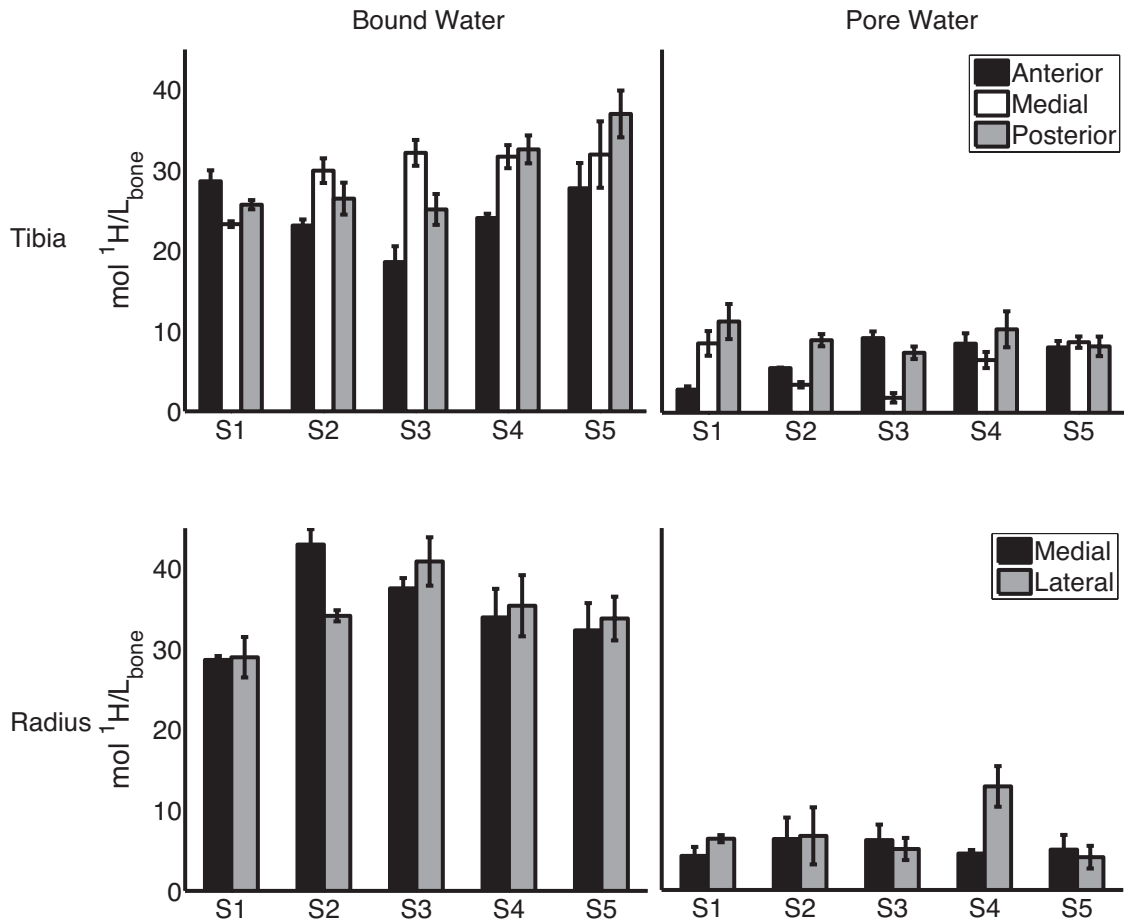
Figure 3.6: Quantified signal from the five ROIs analyzed in the tibia and radius in all three subjects (S1, S2, S3). Bars represent the mean of the ROIs over the three repeated scans, the error bars represent the inter-scan variability (SD between the three scans).

fracture risk compared to the decrease in bone density measurements in type 2 diabetes or aging populations that have demonstrated increased brittleness that can not be measured with current X-ray methods [27,28]. Pore water is an indirect measure of porosity; as pore water increases porosity increases [29]. Therefore, we postulate that subjects at high risk for fragility fractures will generally have high pore water and/or low bound water, though more studies need to be done to justify this claim. In future studies, these methods will be applied to subjects with poor bone health such as post-menopausal women to evaluate changes in bound and pore water in response to treatment.

In contrast to previous MRI studies of human bone in vivo, which provided structural

information [12,30] or net cortical bone water [31-33], our methods specifically discriminate signals from bound and pore water. (Although, one of these previous studies [32] included soft-tissue signal suppression, which likely suppressed some portion of the pore water signal.) An alternate approach for distinguishing bound and pore water signals in cortical bone using only T_2^* differences and bi-component analysis of the signal decay with echo time has been demonstrated ex vivo [26]. If incorporated into fast 2D UTE acquisitions across a wide range of echo times [31] this approach may offer another clinically-viable MRI protocol for bound and pore water measurements in vivo. Our methods directly measure bound and pore water content, which do not require multiple echo times or as high of an SNR as bi-component analysis needs to measure bound and pore water signal using T_2^* differences. Bi-component analysis can be further confounded when the underlying signal has more than two T_2^* components or fat signal which does not decay exponentially due to chemical shift differences with water. In addition, similar to some previous quantitative MRI studies of cortical bone [26, 27], the DAFP and AIR studies presented here used reference phantoms to convert signals into absolute units of proton concentration. This is especially important when separating two distinct signals from the bone, because a change in the relative fractions of these two signals could be due to a specific change in either or both.

Like many quantitative MRI protocols, the primary limitations of the methods presented here are precision and scan time. The per-voxel intra-scan variability alone was ≈ 0.8 mol ^{1}H/L$_{bone}$ in scan times of $8-14$ min, but the pooled SD of signal intensities across repeated scans was roughly twice that (Tables 1 and 2), indicating room for improvement in precision that is independent of raw SNR.

The effect of excitation flip angle calibration on our measurements was independently investigated by acquiring B_1+ maps [34], repeated on one subject five times in the tibia and three times in the radius, repositioning between measurements. Using measured B_1+ values in the bone and reference marker from these scans, the prescribed B_1+, and mean

56

bound and pore water concentrations listed in at the bottoms of Tables 1 and 2, the effect of B_1+ variation between scans on bound and pore water concentrations was calculated. These calculations showed B_1+ variations resulted in a SD in bound and pore water concentrations, respectively, to be 0.80 and 0.30 mol ^{1}H/L$_{bone}$ in the tibia and slightly lower in the radius. In principle, this source of signal variation can be accounted for with B_1+ mapping and/or better RF calibration protocols.

It is also possible that some precision errors were due to the B_1- mapping. While there was not apparent significant signal drop out in the smoothed coil sensitivity maps in the bone region, it would be advantageous to use a more sophisticated method such as inpainting to calculate the sensitivity map in areas such as the bone and reference marker. Future studies may improve on this method, however the current method gave no obvious artifacts in signal intensity.

The remaining systematic inter-scan signal variation was likely due to variation of ROI placement and associated partial volume effects. As a simple test, signal intensities were re-computed for whole-slice ROIs, and the inter-scan pooled SD decreased by an average of 0.5 mol ^{1}H/L$_{bone}$. Thus, defining larger ROIs will tend to reduce the inter-scan variance, although at the expense of losing sensitivity to more localized changes of bound or pore water concentrations. Some more sophisticated signal analysis that considers the distribution of bound and pore water throughout the entire bone volume might offer both low inter-scan variance and high sensitivity to local or global changes in bone characteristics. Also, higher resolution scans may permit more reproducible, automated ROI placement and will minimize partial volume averaging effects. Resolution may be a particularly important limitation when imaging osteoporotic patients that tend to have thin bone cortex.

Higher resolution images will require both faster scan protocols and some increase in SNR. The use of dedicated/specialized RF coils for signal reception offers the best opportunity to improve resolution and scan time albeit with a smaller field of view. Beyond hardware improvements, reduced [35] or anisotropic [36,37] field of view methods might

be effective in increasing resolution or in accessing regions, such as the femoral neck, that would otherwise require a relatively large 3D field of view and long scan time. Similarly, another possible approach is to use 2D rather than 3D UTE acquisitions. Current 2D UTE protocols use half-pulse RF excitation to keep echo times short [38-40], but signal amplitudes from these methods are very sensitive to gradient waveform calibration, making their use for quantitative methods a challenge. A 2D UTE protocol that is relatively insensitive to gradient performance has been proposed [41], but it comes with an additional SNR cost. Finally, given the relatively sparse nature of the bound and pore water maps, model based reconstruction or compressed sensing may offer avenues to reducing scan time.

Despite the current limitations of the DAFP and AIR methods, the results (Tables 3.1 and 3.2, and Figure 3.6) demonstrate potential for these methods to provide clinical insight into changes in bone health. Using the pooled SD estimates as the standard error (SE) for each method and bone, the smallest significant statistical difference detectable between repeated scans of a given individual is $t_{\alpha,\upsilon} \times \sqrt{(2)} \times SE$, where $t_{\alpha,\upsilon}$ is the t-statistic for a significance level of α and a two-tailed test, and υ is the degrees of freedom [27]. Using $\alpha = .05$ and $\upsilon = (n - k)$, with n = 45/30 (number of subjects $\times$ number of ROIs $\times$ number of scans) and k = 15/10 (number of subjects $\times$ number of ROIs) for tibia/radius based on data from this study, these smallest statistical differences are 3.3/5.8 mol ^{1}H/L$_{bone}$ in the pore water of the tibia/radius, and 5.7/7.5 mol ^{1}H/L$_{bone}$ in the bound water of the tibia/radius. Given the estimates for reducing inter-scan variability through quantitative B_1+ mapping and whole-bone data analysis, provided above, these smallest statistical differences may drop to 2.4/3.4 mol ^{1}H/L$_{bone}$ in the pore water of the tibia/radius, and 4.4/6.8 mol ^{1}H/L$_{bone}$ in the bound water of the tibia/radius. In the limit that the only factor in inter-scan repeatability is thermal noise, with the current SNR these differences drop further to 1.9/2.5 mol ^{1}H/L$_{bone}$ in the pore water of the tibia/radius, and 3.8/4.7 mol ^{1}H/L$_{bone}$ in the bound water of the tibia/radius.

Although these values are not small compared to the variation in bound and pore water

measures across subjects here, only healthy and relatively young volunteers were included in our study, which gave a relatively small range of bound and pore water values. A greater range of values is expected between healthy and unhealthy bones. From previous ex-vivo studies of cortical bone samples, bound water measures in the femur ranged from ≈ 11 to 24 mol ^{1}H/L$_{bone}$ while pore water measures ranged from ≈ 5 to 30 mol ^{1}H/L$_{bone}$ [20, 22]. These bone samples came from 43 cadavers with unknown bone health (ages 21-105 y.o.), so this wider range (13/25 mol ^{1}H/L$_{bone}$ for bound/pore water) may reflect a more clinically relevant range of values than seen in the normal subjects of our study. Further studies are needed to determine the diagnostic potential for these measures for specific clinical conditions.

In conclusion, our study demonstrates that quantitative MRI that is selective for bound or pore water of cortical bone can be practically acquired in vivo, providing bound and pore water maps with standard errors ≈ 2 mol ^{1}H/L$_{bone}$.

3.5   References

[1] NIH Consensus Development Panel on Osteoporosis Prevention, Diagnosis, and Therapy. Osteoporosis prevention, diagnosis, and therapy. JAMA. 2001;285(6):78595.

[2] Kanis J. Diagnosis of osteoporosis and assessment of fracture risk. Lancet. 2002; 359(9321):192936.

[3] Link TM. Osteoporosis imaging: state of the art and advanced imaging. Radiology. 2012;263(1):317.

[4] Gler CC, Eastell R, Reid DM, et al. Association of five quantitative ultrasound devices and bone densitometry with osteoporotic vertebral fractures in a population-based sample: the OPUS Study. J Bone Min Res. 2004;19(5):78293.

[5] Krieg M-A, Barkmann R, Gonnelli S, et al. Quantitative ultrasound in the management of osteoporosis: the 2007 ISCD Official Positions. J Clin Densitom. 2008; 11(1):16387.

[6] Guglielmi G, Adams J, Link TM. Quantitative ultrasound in the assessment of skeletal status. Eur Radiol. 2009;19(8):183748.

[7] Burrows M, Liu D, McKay H. High-resolution peripheral QCT imaging of bone micro-structure in adolescents. Osteoporos Int. 2010;21(3):51520.

[8] Liu XS, Zhang XH, Sekhon KK, et al. High-resolution peripheral quantitative computed tomography can assess microstructural and mechanical properties of human distal tibial bone. J Bone Min Res. 2010;25(4):74656.

[9] Burghardt AJ, Issever AS, Schwartz A V., et al. High-resolution peripheral quantitative computed tomographic imaging of cortical and trabecular bone microarchitecture in patients with type 2 diabetes mellitus. J Clin Endocr Metab. 2010; 95(11):504555.

[10] Kanis JA, McCloskey E V, Johansson H, Oden A, Strm O, Borgstrm F. Development and use of FRAX in osteoporosis. Osteoporos Int. 2010;21(Suppl2):S40713.

[11] Kanis JA, Hans D, Cooper C, et al. Interpretation and use of FRAX in clinical practice. Osteoporos Int. 2011;22(9):2395411.

[12] Majumdar S, Genant HK, Grampp S, et al. Correlation of trabecular bone structure with age, bone mineral density, and osteoporotic status: in vivo studies in the distal radius using high resolution magnetic resonance imaging. J Bone Min Res. 1997;12(1):1118.

[13] Wehrli FW, Hwang N, Ford JC, Haddad JG. Cancellous bone volume and structure in the forearm: noninvasive assessment with MR microimaging and image processing. Radiology. 1998;206:34757.

[14] Manske SL, Liu-Ambrose T, Bakker PM, et al. Femoral neck cortical geometry measured with magnetic resonance imaging is associated with proximal femur strength. Osteoporos Int. 2006;17(1):153945.

[15] Bae WC, Chen PC, Chung CB, Masuda K, DLima D, Du J. Quantitative ultrashort echo time (UTE) MRI of human cortical bone: correlation with porosity and biomechanical properties. J Bone Min Res. 2012;27(4):84857.

[16] Horch RA, Nyman JS, Gochberg DF, Dortch RD, Does MD. Characterization of 1H NMR signal in human cortical bone for magnetic resonance imaging. Magn Reson Med. 2010;64(3):6807.

[17] Ong HH, Wright AC, Wehrli FW. Deuterium nuclear magnetic resonance unambiguously quantifies pore and collagen-bound water in cortical bone. J Bone Min Res. 2012;27(12):257381.

[18] Fernndez-Seara MA, Wehrli SL, Takahashi M, Wehrli FW. Water content measured by proton-deuteron exchange NMR predicts bone mineral density and mechanical properties. J Bone Min Res. 2004;19(2):28996.

[19] Nyman JS, Ni Q, Nicolella DP, Wang X. Measurements of mobile and bound water by nuclear magnetic resonance correlate with mechanical properties of bone. Bone. 2008;42(1):1939.

[20] Horch RA, Gochberg DF, Nyman JS, Does MD. Non-invasive predictors of human cortical bone mechanical properties: T(2)-discriminated H NMR compared with high resolution X-ray. PLoS One. 2011;6(1):e16359.

[21] Horch RA, Gochberg DF, Nyman JS, Does MD. Clinically compatible MRI strategies for discriminating bound and pore water in cortical bone. Magn Reson Med. 2012;68(6):177484.

[22] Manhard MK, Horch RA, Harkins KD, Gochberg DF, Nyman JS, Does MD. Validation of quantitative bound- and pore-water imaging in cortical bone. Magn Reson Med. 2014;71(6):216671.

[23] Haacke EM, Brown RW, Thompson MR, Venkatesan R. Magnetic Resonance Imaging - Physical Principles and Sequence Design. 1999. p. 4635.

[24] Gurney P, Pauly J, Nishimura DG. A simple method for measuring B0 eddy currents [abstr]. Proc Intl Soc Magn Reson Med 13. 2005;866.

[25] Zwart NR, Johnson KO, Pipe JG. Efficient sample density estimation by combining gridding and an optimized kernel. Magn Reson Med. 2012;67(3):70110.

[26] Du J, Hermida JC, Diaz E, et al. Assessment of cortical bone with clinical and ultrashort echo time sequences. Magn Reson Med. 2013;70:697704.

[27] Kanis JA, Johnell O, Oden A, Dawson A, De Laet C, Jonsson B. Ten year probabilities of osteoporotic fractures according to BMD and diagnostic thresholds. Osteoporos Int. 2001;12(12):98995.

[28] Vestergaard P. Discrepancies in bone mineral density and fracture risk in patients with type 1 and type 2 diabetes–a meta-analysis. Osteopros Int. 2007;18(4):42744.

[29] Biswas R, Bae W, Diaz E, et al. Ultrashort echo time (UTE) imaging with bi-component analysis: bound and free water evaluation of bovine cortical bone subject to sequential drying. Bone. Elsevier Inc.; 2012;50(3):74955.

[30] Baum T, Kutscher M, Mller D, et al. Cortical and trabecular bone structure analysis at the distal radius-prediction of biomechanical strength by DXA and MRI. J Bone Min Metab. 2013;31(2):21221.

[31] Du J, Hamilton G, Takahashi A, Bydder M, Chung CB. Ultrashort echo time spectroscopic imaging (UTESI) of cortical bone. Magn Reson Med. 2007;58(5):10019.

[32] Techawiboonwong A, Song HK, Leonard MB, Wehrli FW. Cortical Bone Water: in vivo quantification with ultrashort echo-time MR imaging. Radiology. 2008; 248(3):82433.

[33] Rad HS, Lam SCB, Magland JF, et al. Quantifying cortical bone water in vivo by three-dimensional ultra-short echo-time MRI. NMR Biomed. 2011;24(7):85564.

[34] Sacolick LI, Wiesinger F, Hancu I, Vogel MW, 2010. B_1 mapping by Bloch-Siegert shift. Magn Reson Med. 2010;63(5):13151322.

[35] Techawiboonwong A, Song HK, Wehrli FW. In vivo MRI of submillisecond T 2 species with two-dimensional and three-dimensional radial sequences and applications to the measurement of cortical bone water. NMR Biomed. 2008;21:5970.

[36] Larson PZ, Gurney PT, Nishimura DG. Anisotropic field-of-views in radial imaging. IEEE Trans Med Imaging. 2008;27(1):4757.

[37] Li C, Siefert A, Magland J, Wehrli F. Zero Echo Time (ZTE) imaging with anisotropic field-of-view [abstr]. Proc Intl Soc Magn Reson Med 21. 2013;762.

[38] Robson MD, Gatehouse PD, Bydder M, Bydder GM. Magnetic Resonance: An introduction to Ultrashort TE (UTE) imaging. J Comput Assist Tomo. 2003;27(6):82546.

[39] Wang K, Du J, OHalloran R, et al. Ultrashort TE spectroscopic imaging (UTESI) using complex highly-constrained backprojection with local reconstruction (HYPR LR). Magn Reson Med. 2009;62(1):12734.

[40] Du J, Diaz E, Carl M, Bae W, Chung CB, Bydder GM. Ultrashort echo time imaging with bicomponent analysis. Magn Reson Med. 2012;67(3):6459.

[41] Harkins KD, Does MD, Grissom WA. Iterative method for predistortion of MRI gradient waveforms. IEEE T Med Imaging. 2014;33(8):16417.

Chapter 4

MRI-derived Bound and Pore Water Concentrations as Predictors of Fracture Resistance

Text for this section was taken from:

Manhard MK, Uppuganti S, Granke M, Gochberg DF, Nyman JS, Does MD. MRI-derived Bound and Pore Water Concentrations as Predictors of Fracture Resistance. Bone 2016; 87:1-10.

4.1 Introduction

Current methods for predicting fracture risk are X-ray based, most commonly dual-energy x-ray absorptiometry (DXA). DXA provides an areal measure of bone mineral density (aBMD) and then based on reference population data, a T-score (number of standard deviations below normal aBMD) is determined [1]. However, the use of aBMD to diagnose osteoporosis (T-score < -2.5) has low sensitivity - many fractures occur in those with normal-to-osteopenic T-scores (between -2.5 and -1) [2]. Moreover, the increase in fracture risk with age is greater than predicted by the age-related loss in bone mass or aBMD [3]. Because DXA is a 2D imaging technique, it is not particularly sensitive to the contribution of bone structure and architecture to whole bone fracture resistance. Quantitative computed tomography (QCT) and more recently high-resolution peripheral-QCT (HR-pQCT) are 3D imaging techniques that can provide clinical measurements of volumetric BMD (vBMD) as well as structural and architectural parameters. While there is evidence that these methods find differences between fracture cases and non-fracture cases [4-7], there is an overlap in the imaging measures between these cases, and they do not fully explain the increased fracture risk with age. In effect, structure and mineral density are not the sole determinants of fracture resistance [8].

Risk factors of fracture include age, prior fracture incidents, alcohol consumption, fam-

ily history, and use of corticosteroids. These factors are often included as additional predic-
tors to aBMD when using the Fracture Risk Assessment Tool (FRAX) to assess a patients
probability of suffering a fracture within 10 years. While a useful calculator, these addi-
tional risk factors still have low sensitivity and specificity [9], especially for people with
type 2 diabetes [10]. Missing from DXA and FRAX is the contribution of the collagen
phase of bone to fracture resistance. Recently, ultra-short echo time (UTE) magnetic res-
onance imaging (MRI) has been used to image cortical bone [11-13]. Unlike micro-MRI
(μMRI) that provides images of trabecular architecture [14,15] (akin to HR-pQCT), UTE-
MRI has the potential to probe the water bound to collagen in addition to pore water, a
presumptive surrogate of cortical porosity.

The water bound to the mineralized collagen matrix, or bound water, has a short trans-
verse relaxation time constant (T_2), 400 μs at 3T (the magnetic field strength), while the
water in the pore space of cortical bone has a longer T_2 (1 ms – 1 s) [16]. In ^{1}H nuclear
magnetic resonance (NMR) studies using machined samples of human cortical bone, these
bound and pore water signal components have been shown to correlate with the material
properties of the bone as determined by mechanical tests in bending [17]. Bound water
concentration (C_{bw}) decreases with age–possibly due to loss of matrix and/or the accumu-
lation of non-enzymatic collagen crosslinks [18]–and positively correlates with peak bend-
ing strength [17] and crack initiation toughness [19]. As an indirect measure of porosity of
the cortical bone [19], pore water concentration (C_{pw}) negatively correlates with bending
strength of human cortical bone.

Various UTE MRI methods have the potential to clinically investigate bound and pore
water of cortical bone, such as using bi-component analysis of the signal decay with echo
time to find T_2^* values and relative signal of bound and pore water [20] or using a dual echo
method to find a porosity index [11]. While C_{bw} and C_{pw} as determined by non-clinical
methods correlate with the material properties of cortical bone [17,21], clinically translat-
able imaging-derived C_{bw} and C_{pw} have not yet been tested as predictors of whole bone

mechanical properties. In this study, we used previously described T_2-selective magnetization preparations, adiabatic inversion recovery (AIR) and double adiabatic full passage (DAFP), in combination with UTE MRI to selectively image C_{bw} and C_{pw} in cortical bone [12,22,23].

While X-ray-based approaches give reasonably good estimates of bone mass and bone structure, the primary determinants of fracture resistance are due to more than whole bone strength alone. Toughness, or the capacity of bone to dissipate energy during failure, is known to decrease to a greater extent with advanced aging than material strength (independent of structure) [24]. This loss in toughness is perhaps one reason older subjects are more likely to break a bone regardless of their BMD measurement. This study aimed to determine whether MRI-derived measures of C_{bw} and C_{pw} of cadaveric specimens correlate with the material properties of human cortical bone (such as strength and toughness) as determined by three-point bending tests of the distal-third radius, as well as to compare MRI measures with X-ray based imaging measures, aBMD (DXA) and vBMD (by high-resolution μCT).

Part of the evaluation of how MRI measures correlate with whole bone mechanical properties is the evaluation of how best to extract quantitative information from 3D MRI C_{bw} and C_{pw} maps. Though several groups have quantified MRI-derived measures of bone, the best way to analyze and draw information from the maps remains unclear. A previous study found that small regions of interest (ROIs) inside the bone may miss changes in porosity relevant for predicting fracture [11]. In addition, when using an ROI that includes the whole bone, the determination of segmentation of cortical bone from surrounding tissue, particularly at the endosteal boundary, may significantly alter the information content of C_{bw} and C_{pw} measures. For example, the endosteal region has been shown to be the first to deteriorate when bone loss occurs [25-28], and therefore may be important for identification of increasing fracture risk. In this study, we investigate this problem by evaluating and comparing multiple methods of extracting quantitative information from MR images.

In summary, the purpose of this study was to evaluate the usefulness of whole bone imaging properties in predicting whole bone biomechanical properties. This was assessed with cadaveric radii by comparing material properties of the bone, as determined by three-point bend testing, to quantitative measures derived from MRI, DXA, and μCT images. Methods of deriving quantitative measures from MRI maps were also assessed.

4.2 Materials and Methods

4.2.1 Cadaver Specimen Processing

The Vanderbilt Donor Program (Nashville, TN) supplied fresh human forearms (elbow to fingertip) from 40 cadavers (age 56 to 97, mean 80 ± 9.5, 20 male, 20 female). DXA and MRI measures were acquired on the whole intact forearms (Figure 4.1), and subsequently, the radii were dissected out and cut 7.5 cm proximally from the distal third of the bone using a circular low-speed, water irrigated, diamond-embedded band saw (SouthBay Technology Inc., Model 660-1534). Following dissection, μCT imaging was performed on the radii with the bone immersed in a phosphate-buffered saline (PBS) medium at pH 7.4 during the scan. All imaging measurements were performed at the distal-third site of the radius. Lastly, the distal-third site was tested to failure in a three point bending (Figure 4.2). The specimens were kept for a maximum of 48 hours before being returned to the Vanderbilt Donor Program. When not being analyzed, the specimens were stored at 4°C to prevent multiple freeze-thaw cycles.

4.2.2 MRI

The forearms were imaged with a Philips Achieva (Best, NL) 3T scanner using the 8-channel knee coil for receive and the body coil for transmission. A short-T_2 reference phantom (CuSO4-doped 10% H_2O:90%D_2O) in the field of view was used along with the signal equations to convert intensity into absolute units of concentration (mol ^{1}H/L$_{bone}$)

[29]. The AIR (for C_{bw} mapping) and DAFP (for C_{pw} mapping) sequences were used for acquiring C_{bw} and C_{pw} on each forearm using a 3D radial readout with uniform sampling on a sphere [30]. Images were reconstructed using either standard Philips base code or reconstructed off-line using measured gradient trajectories. (In general, the latter approach was needed.) The k-space trajectories were measured using a modified Duyns method [31] on the x, y, and z axis. These trajectories were interpolated to the 3D radial spokes acquired and used in a gridding reconstruction [32] off the scanner.

The AIR sequence used a repetition time (TR) = 400 ms, an inversion time (TI) = 80 ms, and an eighth ordered hyperbolic secant (HS8) pulse for inversion. The DAFP sequence used a TR = 300 ms, delay time (TD) = 5 ms, and two consecutive HS8 pulses. Samples were acquired with a receiver bandwidth of 322 kHz along 124,992 radial half-spokes in k-space to uniformly sample on a sphere and cover a 250 mm^3 FOV at a 1 mm isotropic nominal resolution, for a total scan time of 39 min for the AIR sequence and 54 min for the DAFP sequence. As described in Manhard et. al. [23], for each magnetization preparation in both AIR and DAFP scans, 16 spokes were acquired (3.5 ms TR per spoke) using a variable flip angle scheme with an initial flip angle of 12.5° and an effective flip angle of 60°. The receive-coil sensitivity (B_1-) map was characterized by computing the ratio of two low resolution UTE images using the knee coil for receive on one scan and the body coil for receive on the other. This map was smoothed with a 5 by 5 median filter to remove signal dropout in cortical bone regions and applied to the AIR and DAFP scans before quantitation.

Bone signal was quantified using signal equations [23] to solve for the relative spin densities of bound water, pore water, and the reference marker, and then converted to absolute units of concentration using the known concentration of the reference marker. A constant value of the longitudinal relaxation (T_1), transverse relaxation (T_2), and inversion efficiency (α) of bound water, pore water, and the reference marker was used across specimens. Bound water was estimated to have a $T_1/T_2/\alpha$ of 290 ms/350 μs/0.09, pore water

was estimated to have a $T_1/T_2/\alpha$ of 450 ms/2600 μs/0.78, and the reference marker was estimated to have at $T_1/T_2/\alpha$ of 10 ms/10 ms/-0.83. Because the T_2 of the bone protons is on the order of the acquisition time, it is necessary to account for blurring of the signal that is induced by relaxation during the acquisition. As described in Manhard et al [23], this signal loss or blurring factor (β) was estimated on a voxel-by-voxel basis using the known two-dimensional geometry of the bone and an apodizing function that represents the blurring expected for a given location in k-space. The masked image of the bone is Fourier transformed into k-space, multiplied by the apodizing function to account for the effect of T_2^* blurring, and then inverse Fourier transformed back to image space to create a blurred mask.

The resulting C_{bw} and C_{pw} maps were analyzed by finding ROIs of the whole radius at the distal third section, through approximately 13 mm along the diaphysis of the bone. The ROIs were determined on a slice-by-slice basis using a polar segmentation method described by Rad et al [29]. In brief, the bone marrow signal was first segmented using region growing [33], and the centroid of the bone marrow signal was found. A polar transformation was then performed about the centroid, and for each angle in the polar transformed image, the first and second peaks of the derivative of the 1D data were used to define the inner and outer boundary of bone. This mask was then transformed back into Cartesian image space. Because previous literature has shown a sensitivity to the information in the endosteal region related to fracture risk [28,34], a second whole bone ROI was found by moving the inner boundary outward by a margin of 1.5 mm to decrease the amount of endosteal region that was classified as cortical bone. The outer periosteal boundary was left the same for both ROIs, as this boundary was better defined. The two ROIs for each bone were used to evaluate how the inclusion or exclusion of the endosteal region affected quantification of C_{bw} and C_{pw}, and, in-turn, the correlations between these measures and the strength and toughness measures. In each ROI, metrics computed for analysis included the mean, mode, median, maximum, minimum, first quartile (Q1), third quartile (Q3), and

skewness of C_{bw} and C_{pw}. Correlations between each of these metrics for both ROIs were compared for significant differences.

4.2.3 Dual Energy X-ray Absorptiometry (DXA)

DXA scans of the forearm, while in a supine position on the bed, were acquired using a Lunar iDXA scanner (GE, Madison, WI) at the Vanderbilt Clinical Research Center (Fig 4.1). From the scan, the areal bone mineral density (aBMD) was found in the standard area spanning 13 mm in the axial direction at the distal one-third site.

4.2.4 Micro-Computed Tomography (μCT)

The extracted radii were scanned using a Scanco μCT50 (Scanco Medical, Brttisellen, Switzerland) at an isotropic voxel size of 48 μm (peak X-ray tube potential of 70 kVp, beam current of 200 μA, 1000 projections per 360°, 1500 ms integration time, beam hardening (BH) correction for 1200 mgHA/cm^3 material attenuation, 0.5 mm Al filter). The scan was centered at the distal third of the radius and included a stack of 13 mm (272 slices).

After reconstruction, the scans were analyzed by defining a contour around the endosteal and periosteal surfaces using the Scanco semi-automated contouring tool, which uses slice-by-slice hand contouring with snake algorithms to find edges and an interpolation function between slices [35]. The contoured images were segmented to separate bone material from background (Gaussian noise filter with a sigma of 0.2 and support of 2, lower threshold of 762.5 mgHA/cm^3). Apparent volumetric bone mineral density (vBMD) was the mean value of converted attenuation of all voxels within the contoured volume (mgHA/cm^3). Porosity was calculated by subtracting the bone volume over the total tissue volume from unity. Moment of inertia for the bending about minor axis (Imin), the distance between the centroid and the outer most layer for minor axis (cmin) and the mean total cross sectional area of the bone (Tt.Ar) were also determined using standard scripts provided by the manufacturer. Representative images from all imaging modalities used can

71

be seen in Figure 4.1.
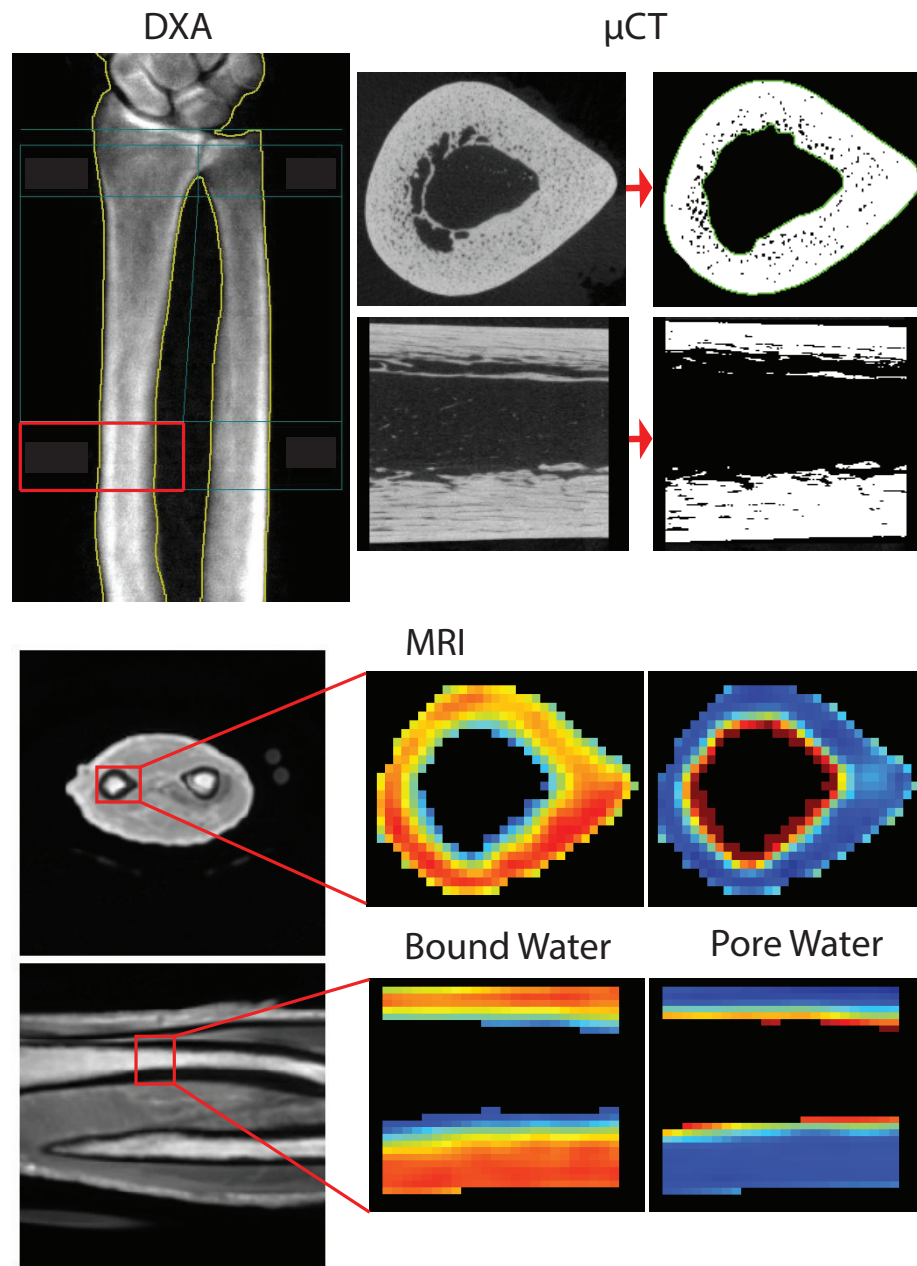
Figure 4.1: The imaging modalities used on one representative radius, all analyzed at the same distal third section (shown in the red boxes). The top left shows the DXA scan, where the blue lines show how the aBMD is typically found in a clinical setting. The red box shows the distal-third section from which the aBMD was used in this study. The top right shows the μCT scan of the distal-third section of the radius in two planes with thresholded bone. The bottom images show a conventional UTE MRI scan in two planes with corresponding C_{pw} and C_{bw} maps. .

4.2.5 Mechanical Testing

The radii were subjected to a three point bending test (MTS 858 Bionix test system with a FlexTest SE controller) by loading the distal third radius, where the bone was imaged, at 6.5 mm/min until failure. Each hydrated bone was positioned with the anterior surface facing down and with the span supports adjusted to 80 mm (40 mm on either side of the distal-third site). The resulting force vs. displacement data (Figure 4.2) was recorded at 100 Hz from a 14 kN load cell and the MTS linear variable displacement transducer (LVDT), respectively. Structural properties included the yield force (calculated at the point in which there was 15% loss in stiffness), the peak force, and work-to-fracture (area under the force vs. displacement curve). To calculate material properties, the flexure formula from beam theory (force $\times$ span $\times$ cmin/4/Imin) was used to determine both peak bending strength and yield strength. Modulus of toughness, or overall toughness, was the area under the stress vs. strain in which stress was determined by the aforementioned flexure formula and strain by $12 \times$ displacement $\times$ cmin/span^2.

4.2.6 Statistical Analysis

All statistical analysis was done with MATLAB (Mathworks, USA) and the MATLAB Statistics Toolbox. Since all imaging properties from the 40 radii were not normally distributed (as determined using a Kolmogorov-Smirnov test), Spearmans correlation coefficients (ρ) were used to evaluate the strength of the relationships between structural or material properties and imaging properties.

To determine to what extent sex explains the variance in each biomechanical property, potential predictors (age and imaging measures) were considered with sex as a categorical variable included in a general linear model. In addition, potential predictors that were not strongly inter-correlated ($\rho < 0.55$) were considered as independent predictors together in a general linear model to determine combinations of predictors that best explain the
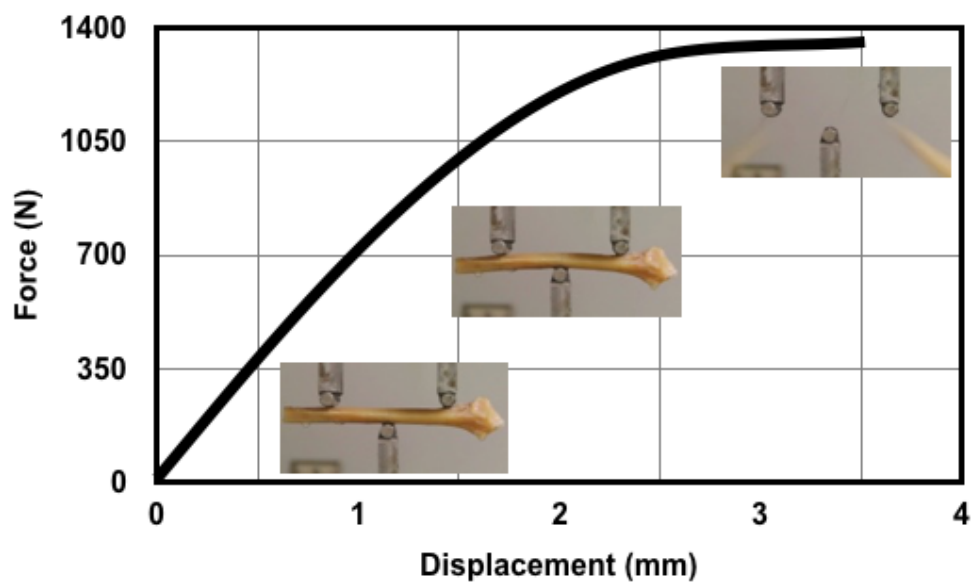
Figure 4.2: Force displacement curve from a three point bend test of a representative radius. The test was performed at the distal third site, and images show the radius in multiple stages of breaking along the curve.

variance in the biomechanical properties. No more than two independent terms and the interaction between them were included in any given model. These linear models were then bootstrapped (1000 iterations) to account for the non-normality of the parameters. The bootstrapping was performed using Matlab's default functions, which use a random sampling of the data in the fit to find significance of the correlation at each iteration. The p-value was then calculated as the median value after 1000 iterations. The predictors were considered significant if the p-value for the variable was less than 0.05.

4.3   Results

An overview of the two ROIs selected from MRI can be seen in Figure 4.3. Mean signal-to-noise ratio (SNR) of the cortical bone signal in the MR images (defined as, where μS is the mean signal in a region of cortical bone and μN is the mean signal in a region of background noise), was found to be 15 (range 5-45) for DAFP images and 12 (range 7-22) for AIR images. Slices from representative AIR and DAFP images of relatively strong and weak cadaveric arms are shown with the endosteal boundary lines overlaid and with the corresponding histograms of signal intensities resulting from each ROI used. The ROI that included more of the endosteal region (zone 1 + zone 2 in Figure 4.3) gave a lower mean C_{bw} and a histogram that was skewed towards lower values compared to the ROI that excluded more of the endosteal region (zone 1 only in Figure 4.3). The mean C_{pw} was higher for the larger ROI with a histogram skewed towards higher values. The change in histogram skewness between the two ROIs was more apparent in weaker bones.

Across all 40 bones, including more endosteal tissue resulted in an average 49% greater C_{pw} per voxel (range = 29 66%) and average 8% lower C_{bw} per voxel (range = -16 - 24%). These differences are not surprising – including more endosteal region will result in the inclusion of more signal from marrowand highlight the sensitivity of these MRI measures to segmentation of cortical bone at the endosteal boundary. Endosteal boundary definition will not only affect the magnitude of C_{bw} and C_{pw}, but also the relationship to mechanical
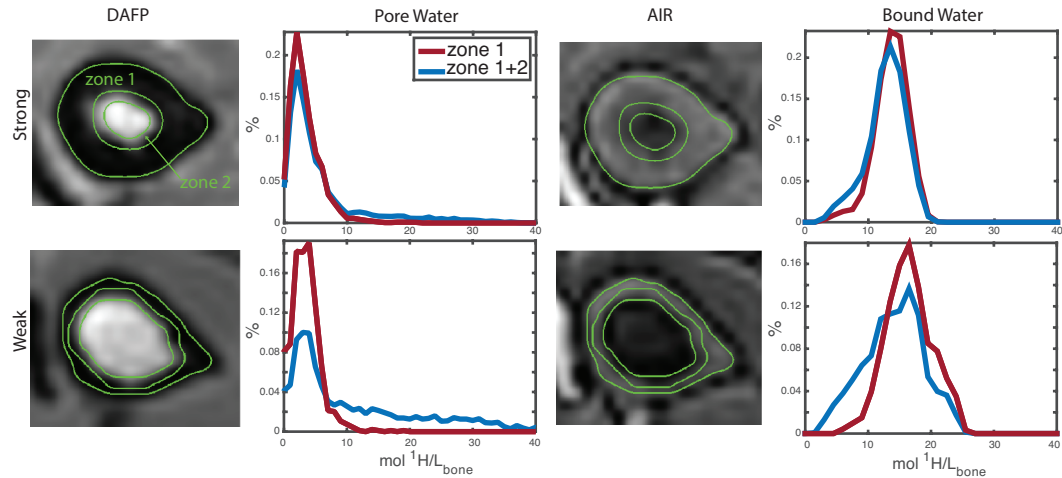
Figure 4.3: DAFP and AIR images of a radius with high (top) and low (bottom) bending strength, with green lines showing boundaries for the different ROIs. The plots show histograms (in % of total) for the C_{bw} and C_{pw} found from the two ROIs. The blue shows histograms for the total bone area including the larger endosteal region (zone 1 + zone 2) and the red shows the smaller endosteal region only (zone 1).

properties of the whole bone. For example, Figure 4.4 shows how correlations of bending strength with the mean and skewness of C_{bw} and C_{pw} are affected by the inclusion or exclusion of this endosteal region (zone 2).

Several metrics from the ROIs were correlated with biomechanical properties to evaluate the best way to extract quantitative information from the MRI-derived maps, including the mean, mode, median, maximum, minimum, Q1, Q3, and skewness. While all of the metrics of C_{pw} significantly correlated with strength and all the metrics of C_{bw} significantly correlated with both strength and toughness for both ROIs, there were no significant differences at the 95% confidence level between metrics or ROIs for either C_{bw} and C_{pw}. Table 1 gives an overview of correlations of the mean, median, and skewness for both ROIs with peak bending strength and toughness. Though not statistically different at the P<0.05 significance level, correlation coefficients were higher in almost all cases when using the larger ROI that included more of the endosteal region (zone 1+zone 2).

Spearmans correlation coefficient (ρ) for C_{bw} and C_{pw} metrics for two ROIs of the
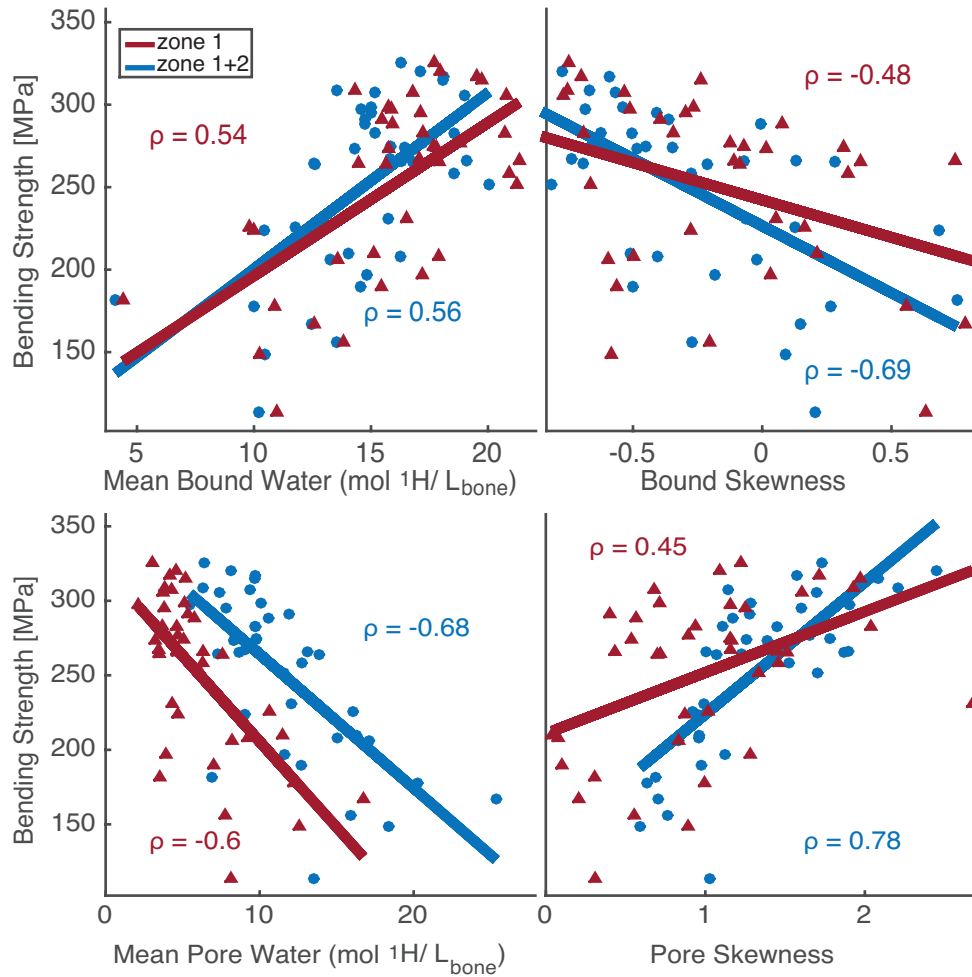
Figure 4.4: Correlations of mean C_{bw} and C_{pw} (left) and skewness of C_{bw} and C_{pw} distributions (right) with bending strength. Blue lines show total bone area including the larger endosteal region and red lines shows the smaller endosteal region.

whole bone at the distal third site (zone 1 + zone 2 includes endosteal region, zone 1 does not include endosteal region) with material properties.

The skewness of both C_{bw} and C_{pw} also gave consistently higher correlations to strength when using the ROI that included the larger endosteal region. These higher correlations with skewness is not surprising because large pores, which tend to accumulate at the endosteal border [36], affect fracture resistance more than small pores [37,38], so even though there is not a substantial change in the mean, the skewness is sensitive to this change. Similarly, the median C_{pw} for the larger ROI gave higher correlations than the mean, which was

Table 4.1: Correlation coefficients between material properties and imaging properties for two regions of interest

Spearman's ρ	Bound Water	Mean	Median	Skewness
Bending Strength	zone1+zone2	0.568	0.568	-0.687
	zone1	0.541	0.542	-0.478
Toughness	zone1+zone2	0.355	0.324	—
	zone1	0.342	—	—
Spearman's ρ	Pore Water	Mean	Median	Skewness
Bending Strength	zone1+zone2	-0.565	-0.744	0.783
	zone1	-0.597	-0.617	0.450

expected since the distribution in the ROI is strongly skewed from normal. The mean and median C_{bw} performed similarly for both strength and toughness, as expected, since the distribution of C_{bw} was more normally distributed. To evaluate MRI C_{bw} and C_{pw} in comparison with DXA and μCT, the metrics with highest correlation coefficients were usedthe skewness of C_{bw} and C_{pw}, mean C_{bw}, and median C_{pw} from the ROI that included both zone 1 and zone 2.

An overview of the significance of potential predictors (age and imaging properties from all modalities) to structural properties of the radii (bending force and work to fracture) is shown in Table 4.2. These statistical analyses included sex as a covariate when significant. All imaging properties explained the variance in the structural properties, with the aBMD from DXA having the highest adjusted coefficient of determination (Adj-R^2) for peak bending force, and C_{bw} having the highest Adj-R^2 for work to fracture. Age had a lower explanation of the variance in structural strength (bending force) than any imaging property, and was not a significant explanatory variable for work-to-fracture. Yield strength predictions were similar to bending strength, and resulting correlations are also shown in Table 4.2.

Table 4.3 shows an overview of corresponding estimated material properties of the bone with statistical significance indicated for the same potential predictors. Sex was again used

as a covariate in the general linear models when significant. While the predictive ability of all imaging parameters was lower for the estimated material strength than for structural strength of the radius, sex was no longer a significant covariate for any of the imaging properties except aBMD. In addition, the only imaging properties that significantly explained the variance in toughness were C_{bw} and porosity (which had a very weak correlation with toughness, though significant with sex as a significant covariate). Age again was the weakest predictor of strength compared to all imaging properties. Figure 4.5 shows plots of correlations with fitted lines for these material properties and selected imaging properties.

Table 4.2: Predictive ability of age and imaging measures with sex as a possible covariate for structural properties.

Structural Property	Variable	Sex	Interaction	Linear Model	Adj-R2
Yield Force	*Age*			M: $5.36 \times 10^3 - 47 * Age$	53.8
	$p < .001$	$p = 0.006$	$p = 0.025$	F: $1.79 \times 10^3 - 11.5 * Age$	
	aBMD			M: $-748 + 3.03 * aBMD$	85.6
	$p < .001$	$p = 0.152$	$p = 0.028$	F: $-363 + 1.97 * aBMD$	
	vBMD			M: $-1.19 \times 10^4 + 15.1 * vBMD$	63.5
	$p < .001$	$p = 0.017$	$p = 0.010$	F: $-3.56 \times 10^3 + 4.9 * vBMD$	
	Porosity			M: $3.04 \times 10^3 - 127 * Porosity$	72.4
	$p < .001$	$p < .001$	$p = 0.002$	F: $1.39 \times 10^3 - 42.1 * Porosity$	
	PW			M: $2.78 \times 10^3 - 170 * PW$	73.5
	$p < .001$	$p < .001$	$p < .001$	F: $1.4 \times 10^3 - 55 * PW$	
	PW_Skew			M: $-280 + 1330 * PW\_Skew$	78.7
	$p < .001$	$p = 0.231$	$p = 0.008$	F: $104 + 642 * PW\_Skew$	
	BW			M: $-909 + 163 * BW$	64.7
	$p < .001$	$p < .001$	n.s.	F: $-241 + 78.8 * BW$	
	BW_Skew			M: 1440-720*BW_Skew	56.8
	$p < .001$	$p < .001$	n.s.	F: $622 - 720 * BW\_Skew$	
Peak Bending Force	*Age*			M: $6.12 \times 10^3 - 51.9 * Age$	59.5
	$p < .001$	$p = 0.004$	$p = 0.021$	F: $1.9 \times 10^3 - 10.9 * Age$	
	aBMD			M: $-161 + 2.76 * aBMD$	84.7
	$p < .001$	$p < .001$	n.s.	F: $-705 + 2.76 * aBMD$	
	vBMD			M: $-1.18 \times 10^4 + 15.5 * vBMD$	64.3
	$p < .001$	$p = 0.039$	$p = 0.021$	F: $-3.4 \times 10^3 + 4.89 * vBMD$	

Continued on next page

Table 4.2 – *Continued from previous page*

Structural Property	Variable	Sex	Interaction	Linear Model	Adj-R^2
	Porosity			M: $3.43 \times 10^3 - 128 * Porosity$	70.8
	$p < .001$	$p < .001$	$p = 0.007$	F: $1.56 \times 10^3 - 42.9 * Porosity$	
	PW			M: $3.18 \times 10^3 - 173 * PW$	72.8
	$p < .001$	$p < .001$	$p = 0.004$	F: $1.59 \times 10^3 - 59.1 * PW$	
	PW_Skew			M: $-24.1 + 1410 * PW\_Skew$	79.9
	$p < .001$	$p = 0.380$	$p = 0.017$	F: $171 + 713 * PW\_Skew$	
	BW			M: $-771 + 179 * BW$	68.5
	$p < .001$	$p < .001$	n.s.	F: $-159 + 83.8 * BW$	
	BW_Skew			M: $1810 - 754 * BW\_Skew$	60.5
	$p < .001$	$p < .001$	n.s.	F: $763 - 754 * BW\_Skew$	
Work to Fracture	*Age*			—	—
	n.s.	n.s.	n.s.		
	aBMD			M: $1.21 \times 10^3 + 4.8 * aBMD$	52.5
	$p < .001$	$p = 0.004$	n.s.	F: $-235 + 4.8 * aBMD$	
	vBMD			M: $-2.23 \times 10^4 + 30.5 * vBMD$	41.8
	$p = 0.009$	$p = 0.049$	$p = 0.034$	F: $1.86 \times 10^3 + 0.97 * vBMD$	
	Porosity			M: $7.79 \times 10^3 - 254 * Porosity$	45.2
	$p = 0.004$	$p < .001$	$p = 0.024$	F: $2.89 \times 10^3 - 11.9 * Porosity$	
	PW			M: $7.17 \times 10^3 - 325 * PW$	40.3
	$p = 0.035$	$p < .001$	n.s.	F: $3.34 \times 10^3 - 60.7 * PW$	
	PW_Skew			M: $2740 + 1570 * PW\_Skew$	45.5
	$p = 0.004$	$p < .001$	n.s.	F: $901 + 1570 * PW\_Skew$	
	BW			M: $-3160 + 521 * BW$	64.4
	$p < .001$	$p = 0.027$	$p = 0.003$	F: $1.400 + 96.2 * BW$	
	BW_Skew			—	—
	n.s.	n.s.	n.s.		

M = Male, F = female, aBMD = DXA area bone mineral density, vBMD = μCT volumetric bone mineral density, C_{pw} = median pore water, C_{pw} _Skew = C_{pw} skewness, C_{bw} = mean C_{bw}, C_{bw} _Skew = C_{bw} skewness, n.s. = not signficant.

Table 4.3: Predictive ability of age and imaging measures with sex as a possible covariate for material properties.

Material Property	Variable	Sex	Interaction	Linear Model	Adj-R^2
Yield Strength	*Age*			$423 - 2.68 * Age$	17.7
	$p = 0.003$	n.s.	n.s.		
	aBMD			M: $2.18 + 0.257 * aBMD$	61
	$p < .001$	$p < .001$	n.s.	F: $51.4 + 0.257 * aBMD$	
	vBMD			$-680 + 0.988 * vBMD$	46.1
	$p < .001$	n.s.	n.s.		
	Porosity			$303 - 7.96 * Porosity$	53
	$p < .001$	n.s.	n.s.		
	PW			M: $319 - 17.1 * PW$	65.9
	$p < .001$	$p = 0.321$	$p = 0.009$	F: $296 - 8.69 * PW$	
	PW_Skew			M: $63.1 + 98.4 * PW\_Skew$	53.5
	$p < .001$	$p = 0.014$	n.s.	F: $95.3 + 98.4 * PW\_Skew$	
	BW			$47.1 + 10.9 * BW$	32.9
	$p < .001$	n.s.	n.s.		
	BW_Skew			$182 - 86.7 * BW\_Skew$	39
	$p < .001$	n.s.	n.s.		
Peak Bending Strength	*Age*			$451 - 2.49 * Age$	17.1
	$p = 0.004$	n.s.	n.s.		
	aBMD			M: $60 + 0.246 * aBMD$	63.8
	$p < .001$	$p = 0.002$	n.s.	F: $95 + 0.246 * aBMD$	
	vBMD			$-505 + 0.841 * vBMD$	37
	$p < .001$	n.s.	n.s.		
	Porosity			$336 - 7.1 * Porosity$	47.1
	$p < .001$	n.s.	n.s.		
	PW			$325 - 8.9 * PW$	53.3
	$p < .001$	n.s.	n.s.		
	PW_Skew			$136 + 88.4 * PW\_Skew$	55.2
	$p < .001$	n.s.	n.s.		
	BW			$93.6 + 10.7 * BW$	35.7
	$p < .001$	n.s.	n.s.		
	BW_Skew			$227 - 81.3 * BW\_Skew$	38.5
	$p < .001$	n.s.	n.s.		

Continued on next page

Table 4.3 – *Continued from previous page*

Material Property	Variable	Sex	Interaction	Linear Model	Adj-R2
Toughness	*Age*			—	—
	n.s.	n.s.	n.s.		
	aBMD			—	—
	n.s.	n.s.	n.s.		
	vBMD			—	—
	n.s.	n.s.	n.s.		
	Porosity			M: $9.63 - 0.205 * Porosity$	8.17
	$p = 0.083$	$p = 0.020$	$p = 0.044$	F: $5.17 + 0.102 * Porosity$	
	PW			—	—
	n.s.	n.s.	n.s.		
	PW_Skew			—	—
	n.s.	n.s.	n.s.		
	BW			M: $-0.267 + 0.488 * BW$	18.5
	$p = 0.003$	$p = 0.040$	$p = 0.027$	F: $6.41 + 0.00487 * BW$	
	BW_Skew			—	—
	n.s.	n.s.	n.s.		

M = Male, F = female, aBMD = DXA area bone mineral density, vBMD = μCT volumetric bone mineral density, C_{pw} = median pore water, C_{pw} _Skew = C_{pw} skewness, C_{bw} = mean C_{bw}, C_{bw} _Skew = C_{bw} skewness n.s. = not signficant.

Correlations between the non-destructive properties of the bone were also of interest to understand determinants of mechanical properties, and Figure 4.6 shows median C_{pw} for each bone plotted against porosity from μCT, with the fitted regression line. In agreement with previous studies [11,34,39], these parameters were highly correlated, giving us further confidence in the C_{pw} measurements as an indirect measure of porosity. There was also a moderate inverse correlation between C_{pw} and C_{bw} (ρ = -0.48, p = 0.002).

Results from multi-variable predictions of bending strength are shown in Table 4 for combinations of imaging parameters that gave better explanations of the variance than either parameter alone, regardless of whether sex was included as a significant covariate. One of the highest predictors of strength came from a combination of C_{bw} and C_{pw} or porosity.
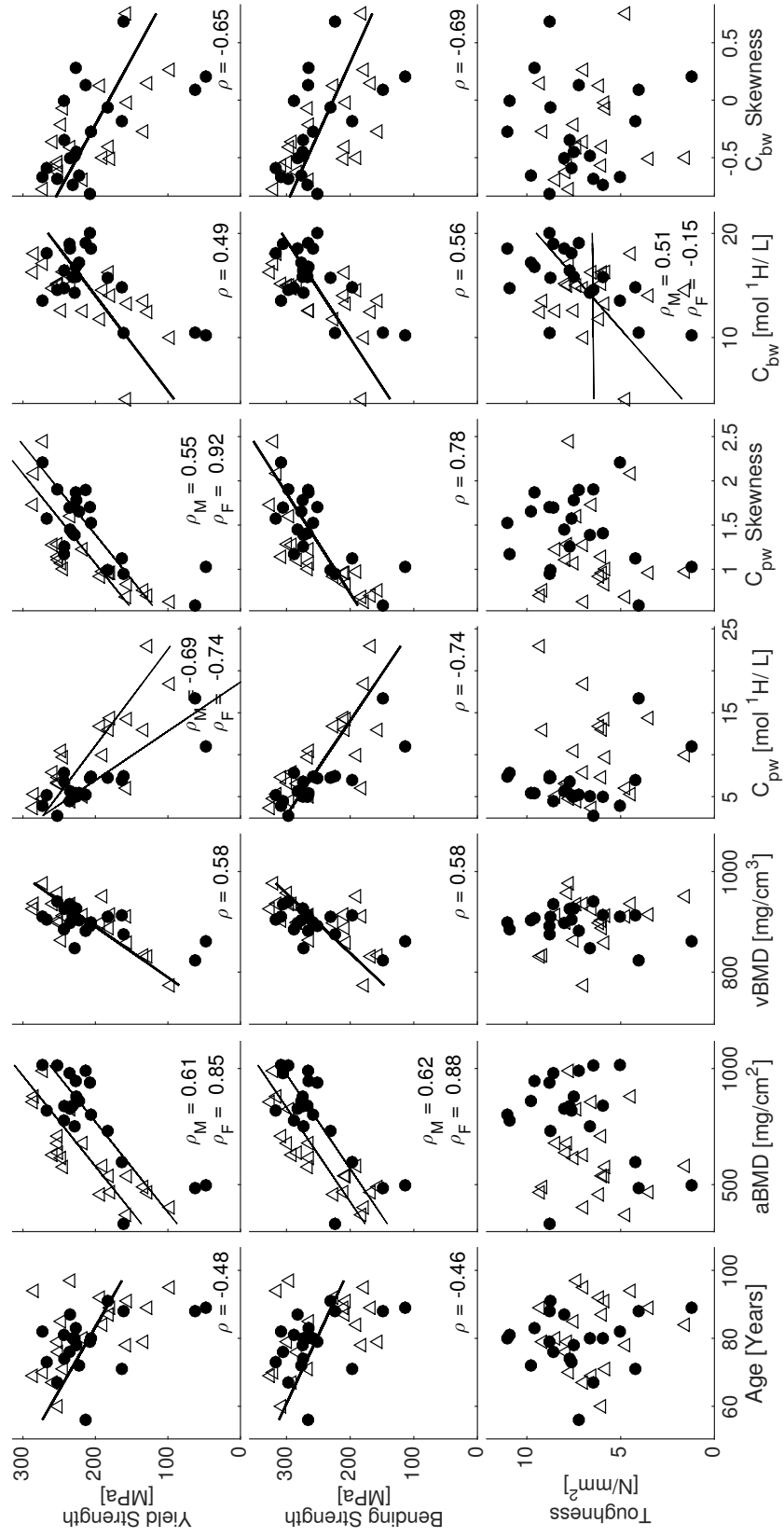
Figure 4.5: Correlations of material properties (bending strength, and toughness) versus age and various imaging properties (aBMD from DXA, vBMD from μCT, and median C_{pw}, C_{pw} skewness, mean C_{bw}, and C_{bw} skewness from MRI) with corresponding Spearman correlation coefficient and p values. Open triangle female, Solid circles - male.
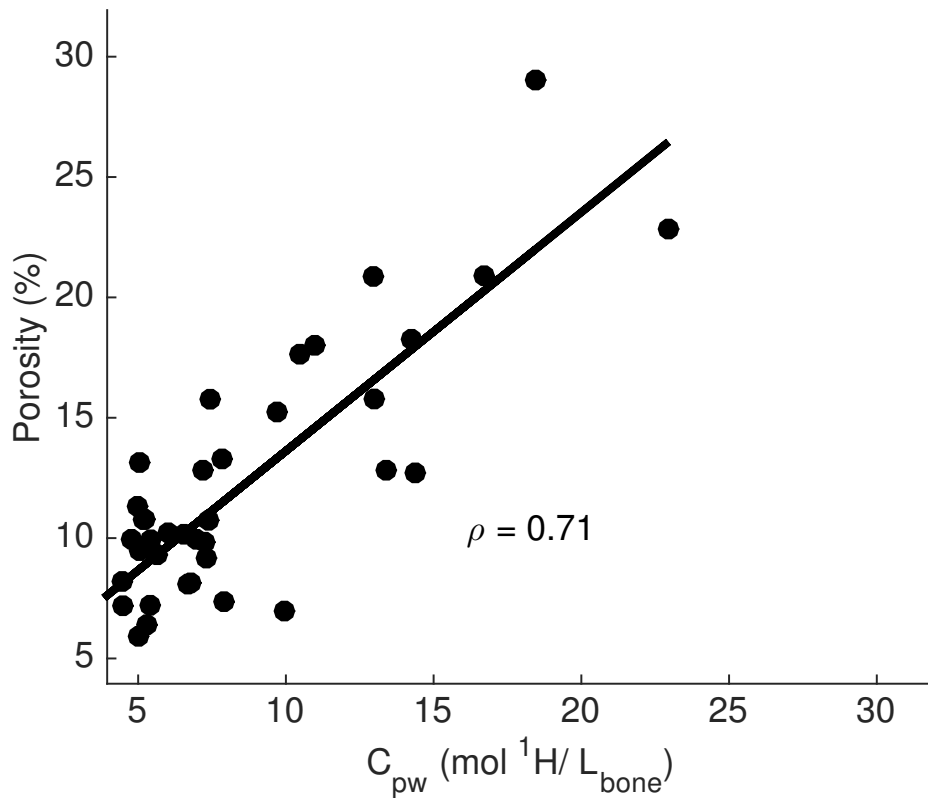
Figure 4.6: Plot showing the correlation between C_{pw} from MRI and porosity from μCT with corresponding Spearmans correlation coefficient (ρ).

There were no significant multi-variable linear models for toughness.

Table 4.4: Multivariate combinations of imaging measurements explaining the variance of material strength.

Material Property	Variable 1	Variable 2	Beta Coefficients	Adj-R2
Yield Strength	$vBMD$	BW	$0.519 * vBMD + 0.385 * BW$	57.2
	$p < .001$	$p = 0.002$		
	$vBMD$	BW_Skew	$0.491 * vBMD - 0.385 * BW\_Skew$	56.1
	$p < .001$	$p = 0.003$		
	$vBMD$	PW	$0.375 * vBMD - 0.457 * PW$	56.2
	$p = 0.012$	$p = 0.003$		

Table 4.4 – *Continued from previous page*

Material Property	Variable 1	Variable 2	Beta Coefficients	Adj-R2
	$vBMD$	PW_Skew	$0.426 * vBMD + 0.446 * PW\_Skew$	58.3
	$p = 0.002$	$p = 0.001$		
	$Porosity$	BW	$-0.574 * Porosity + 0.339 * BW$	61.0
	$p < .001$	$p = 0.005$		
	$Porosity$	BW_Skew	$-0.555 * Porosity - 0.352 * BW\_Skew$	61.3
	$p < .001$	$p = 0.004$		
	PW	BW	$-0.548 * PW + 0.36 * BW$	59.2
	$p < .001$	$p = 0.003$		
	PW	BW_Skew	$-0.535 * PW - 0.392 * BW\_Skew$	61.2
	$p < .001$	$p = 0.001$		
Peak Bending Strength	$vBMD$	BW	$0.424 * vBMD + 0.447 * BW$	52.2
	$p = 0.001$	$p < .001$		
	$vBMD$	BW_Skew	$0.402 * vBMD - 0.427 * BW\_Skew$	49.4
	$p = 0.003$	$p = 0.002$		
	$vBMD$	PW_Skew	$0.275 * vBMD + 0.589 * PW\_Skew$	59.2
	$p = 0.032$	$p < .001$		
	$Porosity$	BW	$-0.509 * Porosity + 0.39 * BW$	58.0
	$p < .001$	$p = 0.002$		
	$Porosity$	BW_Skew	$-0.504 * Porosity - 0.375 * BW\_Skew$	56.6
	$p < .001$	$p = 0.004$		
	PW	BW	$-0.566 * PW + 0.372 * BW$	63.5
	$p < .001$	$p = 0.002$		
	PW	BW_Skew	$-0.567 * PW - 0.373 * BW\_Skew$	63.6
	$p < .001$	$p = 0.001$		

avBMD = μCT volumetric bone mineral density, C_{pw} = median pore water, C_{pw} _Skew

= C_{pw} skewness, C_{bw} = mean C_{bw}, C_{bw} _Skew = C_{bw} skewness. bStandardized coefficients from the general linear model. No interactions were significant.

4.4   Discussion

Fracture resistance depends not only on structural strength (load bearing capacity) but also on the ability of the tissue to dissipate energy (strain bearing capacity). Most prior cadaveric imaging studies reported significant correlations between structural properties and bone mineral density or bone structure and architecture, as determined by quantitative CT, DXA, or MRI [40-42], consistent with results found in this study. The present study also showed that measures of C_{bw} and C_{pw}, derived from UTE MRI correlated with the estimated material properties of bone. C_{bw} positively correlated with both strength and toughness, the latter of which did not correlate with μCT- or DXA-derived measurements. In addition, C_{bw} was not significantly correlated with μCT-derived tissue mineral density (TMD), and does not appear to be a surrogate for μCT- or DXA-derived measurements. Hydration of collagen is known to drastically affect brittleness of bone, although it remains to be determined what tissue characteristics influence C_{bw}[43]. C_{pw} negatively correlated with both yield and bending strength, and additionally was highly correlated with μCT porosity. While MRI-derived C_{pw} is sensitive to water in pores smaller than 48 μm (nominal resolution of the μCT), the μCT measurements were collected at a higher resolution than is currently available clinically with HR-pQCT. The strong correlation between these two measures indicates C_{pw} gives an indirect measure of porosity. Unlike material strength correlations with DXA-derived aBMD, both C_{bw} and C_{pw} correlations were independent of sex. This difference may reflect the fact that aBMD depends on bone size, and thus sex [44]. The correlation between C_{bw} and C_{pw} was low enough that the two measurements could be used as independent variables together in a multivariate correlation, which resulted in a higher coefficient of correlation for bending strength than either alone. This study found that MRI-derived imaging measures of whole bone significantly correlate with

estimated material properties, consistent with previous studies using C_{bw} and C_{pw} measures from NMR of ex vivo bone samples [1719]. Although three-point bending test of the whole bone yields an approximate measure of material properties, it uniquely allows for a direct comparison of the material properties with the whole-bone imaging measurements, all performed at the same anatomical location of the radius.

This study assessed the biomechanical properties of the distal-third radius, which is near a common site (wrist) of fragility fractures, easily imaged with 3D UTE MRI, and permits direct comparison to clinically relevant DXA measures. Though there are moderate correlations between radius strength and imaging properties acquired at different anatomical locations in the body (e.g., hip) [41], site-specific measurements have relatively high correlations with bone strength as determined by in vitro whole-bone testing [40,41]. Therefore, it would also be useful to evaluate these strength-imaging correlations in other common sites of fracture such as the lumbar vertebrae and the femoral neck. However, implementing UTE MRI methods in the lumbar vertebrae and femoral neck presents technical challenges due to the large FOV and high spatial resolution requirements, which would result in long scan times using the current 3D DAFP and AIR protocols. Alternate MRI protocols utilizing 2D acquisitions and/or reduced FOV would likely be necessary to assess such sites.

The MRI acquisitions in this ex vivo cadaveric study were performed with a relatively high resolution (1 mm) and large FOV (250 mm) to ensure coverage of the entire radius and to obtain maximal information about the bones from the images, which resulted in fairly high scan times. In practice, in vivo acquisitions can use a much smaller FOV for the wrist ($\approx$ 120 mm) and similar resolution ($\approx$ 1.2 mm) and still achieve reliable results [12] in clinically practical scan times. The scan times were reduced by acquiring 16 spokes per magnetization preparation, though this does increase the likelihood of bound water signal contaminating the signal for the DAFP sequence. With a shot-to-shot TR = 3.5 ms, approximately 10% of bound water signal will recover during acquisition, which could lead

to pore water being overestimated by 1.8 (range 0.5 - 2.4) mol ^{1}H/L$_{bone}$ in bones with high bound water and low pore water.

Another potential source of error in the C_{bw} and C_{pw} maps is the inclusion of signal from bone marrow, including lipid signal, particularly when using ROIs including the zone 2 region. While chemical shift artifacts for these scans is small (0.34 pixels) due to the high receiver bandwidth, including signal from bone marrow due to segmentation choices and partial volume averaging will likely lead to overestimation of pore water. While this is undoubtedly causing some overestimation in the pore water, the inclusion of the zone 2 area in the ROI still correlates well with biomechanical properties and in fact tends to give higher correlations than ROIs that exclude this area.

Though all of these sources of error of the MRI sequences used in this study have the potential to contaminate the resulting C_{bw} and C_{pw} measurements, C_{bw} and C_{pw} were still found to contain meaningful information about bone quality and fracture risk. In future studies, the MRI methods can be refined or other methods can be used to measure C_{bw} and C_{pw}, such as bi-component analysis, dual-band saturation, or dual-echo time porosity index. Improvements in methods will likely result in stronger correlations between the MRI-measures and bone material properties.

The importance of the ROI placement on assessing these MRI maps of bone is emphasized by the different C_{bw} and C_{pw} measures from the two ROIs with different endosteal boundaries (inclusion or exclusion of zone 2). Specifically, the same image has the potential to give different assessments of fracture risk depending on the extent to which the segmentation includes bone within the endosteal region where there can be a transitional zone in the elderly. While including or excluding the endosteal region may not severely affect correlations with strength and toughness, it is nevertheless important that segmentation is not user-dependent and is performed in a consistent and somewhat automated manner to get reliable results, since the C_{bw} and C_{pw} metrics themselves change significantly depending on the ROI. The effect on correlations also pertains when finding small regions inside

of the bone instead of a whole bone segmentation. We tested this by finding several small ROIs inside the distal-third section of the radii, approximately ≈ 4.5 mm^3 each. While mean C_{bw} and C_{pw} of these ROIs still correlated with strength and toughness, the correlations, though not significantly different, were consistently weaker than the whole bone correlations with strength and toughness.

It is also important to look beyond the mean water concentrations, especially given the skewness of the distribution of concentrations within a whole bone ROI. Bones with a high positive skewness of C_{pw} (shift towards lower concentrations) show higher strength, as well as bones with a negative skewness of C_{bw} (shift towards higher concentrations). Though including more of the endosteal region risks overestimating the mean C_{pw} or underestimating the mean C_{bw} by including voxels that may include marrow space, it is also capturing essential information that is sensitive to the degradation of bone. Dependable analyses of these maps are critical for future studies with C_{bw} and C_{pw} MRI.

Similarly, evaluating ROIs of μCT images for intra-cortical porosity is not straightforward. The current gold standard for evaluating quantitative μCT, as done in this study, involves semi-automatic hand contouring, which has some subjectivity. This is especially true near the endosteal boundary where the cortical bone transitions to trabecular bone. More automatic methods have been suggested for μCT evaluation [27,35], and may eventually be more useful in achieving efficient and repeatable results.

In conclusion, this study demonstrated that clinically relevant MRI images correlate with material properties of bone. C_{bw} and C_{pw} together could be used to help better predict fracture risk, especially in cases where DXA is currently inadequate. In particular, C_{bw} correlated with toughness while no other imaging properties were significantly correlated with this material property assessing the lack of brittleness. Future directions or applications include applying these C_{bw} and C_{pw} MRI methods in vivo to compare groups of patients at risk for fragility fracture. Finding differences between patients with fragility fractures and healthy subjects, as well as finding differences in C_{bw} and C_{pw} in response to various drug

treatments, will help to further evaluate the significance of these quantitative MRI bone methods.

4.5 Acknowledgements

4.6 References

[1] W.H. Organization, Technical report: Assessment of fracture risk and its application to screening for postmenopausal osteoporosis, (1994).

[2] T.M. Link, Osteoporosis imaging: state of the art and advanced imaging., Radiology. 263 (2012) 317.

[3] J.A. Kanis, O. Johnell, A. Oden, A. Dawson, C. De Laet, B. Jonsson, Ten year probabilities of osteoporotic fractures according to BMD and diagnostic thresholds, Osteoporos Int. 12 (2001) 989995.

[4] C. Bergot, A. Laval-Jeantet, K. Hutchinson, I. Dautraix, F. Caulin, H. Genant, A comparison of spinal quantitative computed tomography with dual energy x-ray absorptiometry in European women with vertebral and nonvertebral fractures, Calcif Tissue Int. 68 (2001) 7482.

[5] E.S. Orwoll, L.M. Marshall, C.M. Nielson, S.R. Cummings, J. Lapidus, J.A. Cauley, et al., Finite Element Analysis of the Proximal Femur and Hip Fracture Risk in Older Men, J Bone Min Res. 24 (2009) 47583.

[6] X.S. Liu, E.M. Stein, B. Zhou, C. a Zhang, T.L. Nickolas, A. Cohen, et al., Individual trabecula segmentation (ITS)-based morphological analyses and microfinite element analysis of HR-pQCT images discriminate postmenopausal fragility fractures independent of DXA measurements., J Bone Min Res. 27 (2012) 26372.

[7] K.K. Nishiyama, H.M. Macdonald, D. a Hanley, S.K. Boyd, Women with previous fragility fractures can be classified based on bone microarchitecture and finite element analysis measured with HR-pQCT., Osteoporos Int. 24 (2013) 173340.

[8] C.E.D.H. De Laet, B. A van Hout, H. Burger, A. Hofman, H.A.P. Pols, Bone density and risk of hip fracture in men and women: cross sectional analysis, Br Med J. 315

(1997) 221225.

[9] J.A. Kanis, D. Hans, C. Cooper, S. Baim, J.P. Bilezikian, N. Binkley, et al., Interpretation and use of FRAX in clinical practice., Osteoporos Int. 22 (2011) 2395411.

[10] A. V Schwartz, E. Vittinghoff, D.C. Bauer, T.A. Hillier, E.S. Strotmeyer, K.E. Ensrud, et al., Association of BMD and FRAX Score With Risk of Fracture in Older Adults With Type 2 Diabetes, JAMA. 305 (2011) 218492.

[11] C.S. Rajapakse, M. Bashoor-Zadeh, C. Li, W. Sun, A.C. Wright, F.W. Wehrli, Volumetric Cortical Bone Porosity Assessment with MR Imaging: Validation and Clinical Feasibility, Radiology. 276 (2015) 526535.

[12] M.K. Manhard, R.A. Horch, D.F. Gochberg, J.S. Nyman, M.D. Does, In Vivo Quantitative MR Imaging of Bound and Pore Water in Cortical Bone, Radiology. 277 (2015) 221229.

[13] M. Carl, G.M. Bydder, J. Du, UTE imaging with simultaneous water and fat signal suppression using a time-efficient multispoke inversion recovery pulse sequence., Magn Res Med. 00 (2015) 16.

[14] R. Krug, S. Banerjee, E.T. Han, D.C. Newitt, T.M. Link, S. Majumdar, Feasibility of in vivo structural analysis of high-resolution magnetic resonance images of the proximal femur, Osteoporos Int. 16 (2005) 130714.

[15] G. Chang, C.M. Deniz, S. Honig, C.S. Rajapakse, K. Egol, R.R. Regatte, et al., Feasibility of three-dimensional MRI of proximal femur microarchitecture at 3 tesla using 26 receive elements without and with parallel imaging., J Magn Reson Imaging. 40 (2014) 22938.

[16] R.A. Horch, J.S. Nyman, D.F. Gochberg, R.D. Dortch, M.D. Does, Characterization of 1H NMR signal in human cortical bone for magnetic resonance imaging., Magn

Reson Med. 64 (2010) 6807.

[17] R.A. Horch, D.F. Gochberg, J.S. Nyman, M.D. Does, Non-invasive predictors of human cortical bone mechanical properties: T(2)-discriminated H NMR compared with high resolution X-ray., PLoS One. 6 (2011) e16359.

[18] J.S. Nyman, Q. Ni, D.P. Nicolella, X. Wang, Measurements of mobile and bound water by nuclear magnetic resonance correlate with mechanical properties of bone., Bone. 42 (2008) 1939.

[19] M. Granke, A.J. Makowski, S. Uppuganti, M.D. Does, J.S. Nyman, Identifying Novel Clinical Surrogates to Assess Human Bone Fracture Toughness., J Bone Min Res. 30 (2015) 1290300.

[20] J. Du, J.C. Hermida, E. Diaz, J. Corbeil, R. Znamirowski, D.D. DLima, et al., Assessment of cortical bone with clinical and ultrashort echo time sequences., Magn Reson Med. 70 (2013) 697704.

[21] W.C. Bae, P.C. Chen, C.B. Chung, K. Masuda, D. DLima, J. Du, Quantitative ultrashort echo time (UTE) MRI of human cortical bone: correlation with porosity and biomechanical properties., J Bone Min Res. 27 (2012) 84857.

[22] R.A. Horch, D.F. Gochberg, J.S. Nyman, M.D. Does, Clinically compatible MRI strategies for discriminating bound and pore water in cortical bone., Magn Reson Med. 68 (2012) 177484.

[23] M.K. Manhard, R.A. Horch, K.D. Harkins, D.F. Gochberg, J.S. Nyman, M.D. Does, Validation of quantitative bound- and pore-water imaging in cortical bone., Magn Reson Med. 71 (2014) 21662171.

[24] X. Wang, X. Shen, X. Li, C.M. Agrawal, Age-related Changes in the Collagen Network and Toughness of Bone, Bone. 31 (2002) 17.

[25] N.M. Keshawarz, R.R. Recker, Expansion of the medullary cavity at the expense of cortex in postmenopausal osteoporosis, Metab Bone Dis Relat Res. 5 (1984) 2238.

[26] B. Clarke, Normal bone anatomy and physiology., Clin J Am Soc Nephrol. 3 Suppl 3 (2008) S1319.

[27] R. Zebaze, a Ghasem-Zadeh, a Mbala, E. Seeman, A new method of segmentation of compact-appearing, transitional and trabecular compartments and quantification of cortical porosity from high resolution peripheral quantitative computed tomographic images., Bone. 54 (2013) 820.

[28] E. Perilli, Y. Bala, R. Zebaze, K.J. Reynolds, E. Seeman, Regional Heterogeneity in the Configuration of the Intracortical Canals of the Femoral Shaft., Calcif Tissue Int. 97 (2015) 32735.

[29] H.S. Rad, S.C.B. Lam, J.F. Magland, H. Ong, C. Li, H.K. Song, et al., Quantifying cortical bone water in vivo by three-dimensional ultra-short echo-time MRI., NMR Biomed. 24 (2011) 85564.

[30] S.T.S. Wong, M.S. Roos, A strategy for sampling on a sphere applied to 3D selective RF pulse design, Magn Reson Med. 32 (1994) 778784.

[31] P. Gurney, J. Pauly, D.G. Nishimura, A simple method for measuring B0 eddy currents, Proc Intl Soc Magn Reson Med 13. (2005) 866.

[32] N.R. Zwart, K.O. Johnson, J.G. Pipe, Efficient sample density estimation by combining gridding and an optimized kernel., Magn Reson Med. 67 (2012) 70110.

[33] R. Adams, L. Bischof, Seeded region growing, IEEE Trans Pattern Anal Mach Intell. 16 (1994) 6417.

[34] C. Li, A.C. Seifert, H.S. Rad, Y.A. Bhagat, C.S. Rajapakse, W. Sun, et al., Cortical Bone Water Concentration: Dependence of MR Imaging Measures on Age and Pore

Volume Fraction, Radiology. 272 (2014) 796806.

[35] H.R. Buie, G.M. Campbell, R.J. Klinck, J. a MacNeil, S.K. Boyd, Automatic segmentation of cortical and trabecular compartments based on a dual threshold technique for in vivo micro-CT bone analysis., Bone. 41 (2007) 50515.

[36] C. Chappard, S. Bensalah, C. Olivier, P.J. Gouttenoire, A. Marchadier, C. Benhamou, et al., 3D characterization of pores in the cortical bone of human femur in the elderly at different locations as determined by synchrotron micro-computed tomography images., Osteoporos Int. 24 (2013) 102333.

[37] P. Broulik, J. Kragstrup, L. Mosekilde, F. Melsen, Osteon cross-sectional size in the iliac crest, Acta Pathol Microbiol Immunol Scand. 90A (1982) 339344.

[38] H. Brockstedt, M. Kassem, E. Eriksen, L. Mosekilde, F. Melsen, Age- and sex-related changes in iliac cortical bone mass and remodeling., Bone. 14 (1993) 68191.

[39] R. Biswas, W. Bae, E. Diaz, K. Masuda, C.B. Chung, G.M. Bydder, et al., Ultra-short echo time (UTE) imaging with bi-component analysis: bound and free water evaluation of bovine cortical bone subject to sequential drying., Bone. 50 (2012) 74955.

[40] X.G. Cheng, G. Lowet, S. Boonen, P.H. Nicholson, G. Van der Perre, J. Dequeker, Prediction of vertebral and femoral strength in vitro by bone mineral density measured at different skeletal sites., J Bone Miner Res. 13 (1998) 143943.

[41] E.-M. Lochmller, C. a Lill, V. Kuhn, E. Schneider, F. Eckstein, Radius bone strength in bending, compression, and falling and its correlation with clinical densitometry at multiple sites., J Bone Min Res. 17 (2002) 162938.

[42] T. Baum, M. Kutscher, D. Mller, C. Rth, F. Eckstein, E.-M. Lochmller, et al., Cortical and trabecular bone structure analysis at the distal radius-prediction of biomechanical

strength by DXA and MRI., J Bone Min Metab. 31 (2013) 21221.

[43] J.S. Nyman, L.E. Gorochow, R. Adam Horch, S. Uppuganti, A. Zein-Sabatto, M.K. Manhard, et al., Partial removal of pore and loosely bound water by low-energy drying decreases cortical bone toughness in young and old donors, J Mech Behav Biomed Mater. (2012).

[44] V. Naganathan, P. Sambrook, Gender differences in volumetric bone density: a study of opposite-sex twins., Osteoporos Int. 14 (2003) 5649.

Chapter 5

Fast Bound and Pore Water Concentration Mapping of Cortical Bone found from 2D UTE with Optimized Half-Pulses

5.1   Introduction

Quantitative imaging of bound and pore water concentrations in cortical bone using ultra-short echo time (UTE) Magnetic Resonance Imaging (MRI) has shown potential for evaluating fracture risk [1]–[4]. Cortical bone has two main water components of interest that can be imaged using MRI the water bound to the collagen matrix, or bound water, and the water residing in the pore space, or pore water [5]. Bound water has a T_2 of $\approx 400\ \mu$s at 3T and is thought to be associated with cross-linking of collagen in cortical bone, which has been shown to be associated with the toughness, or brittleness of bone [6]. Pore water has a longer T_2 ranging from 1 ms to 1 s, and correlates strongly with porosity measured from μCT [4]. Porosity and bone mineral density (BMD) are indicators of bone health and are clinically used as the gold standard for predicting fracture risk [7]. Porosity and BMD can be measured with quantitative computed tomography (QCT) or high resolution peripheral QCT (HR-pQCT). More often BMD is measured with dual x-ray absorptiometry (DXA), which gives an areal measure of BMD. However these X-ray based methods are only sensitive to the mineral component of bone, and do not fully explain decreases in fracture resistance.

Using MRI to evaluate cortical bone has the potential to offer new information about fracture resistance. Several groups have developed methods to acquire these measures using clinically practical scans [8]–[10]. In the radius and the tibia, the Double Adiabatic Full Passage (DAFP) and Adiabatic Inversion Recovery (AIR) sequences have been demonstrated in vivo with 3D UTE to acquire maps of cortical bone pore water and bound water concentrations, respectively [9], [11]. In this work, we look to extend these 3D AIR and DAFP methods by implementing 2D UTE sequences to decrease scan time and improve

flexibility of the method.

The 3D AIR and DAFP methods require a relatively long scan time, around 30 minutes total for both acquisitions in regions such as the lower leg or the radius. This long scan time is in part due to the 3D isotropic field of view (FOV) and resolution that is required, and the long repetition time (TR) that is necessary because of specific absorption rate (SAR) constraints. For example, on a typical tibia scan, the FOV and resolution needed are approximately 200 mm and 1.5 mm respectively, with a minimum TR of 400 ms, resulting in a scan time of 14 minutes for either AIR or DAFP. One way to overcome these limitations is to use 2D UTE with the AIR and DAFP preparations to acquire bound and pore water concentration maps in a significantly shorter amount of time. Using 2D UTE instead of the current 3D methods would be especially useful in areas where a large 3D volume would otherwise be required, such as the femoral neck or the lumbar vertebrae (areas typically associated with high fracture risk) [12]. In this study, the 2D methods were applied in the tibia so that they could easily be compared to already established 3D methods.

2D UTE is typically acquired in two passes with a half-pulse selective excitation, so that when the data from the two passes are added together in reconstruction, one full pulse shape is achieved [13]. The signal from inside the slice adds together constructively, while the signal outside of the slice will cancel. This method has well-known issues with image artifacts that arise from gradient eddy currents and predistortions that result in imperfect canceling of out of slice signal [14]–[16]. Several methods have been proposed to overcome this imperfect cancelling, such as the double half-pulse [17], using optimized out of slice signal saturation [18], using a saturation-based slice selection method [19], or using a dedicated pre-scan to estimate imperfections [16], [20]. In this study, we used predistortion methods described by Harkins et.al. to iteratively minimize error in the slice select gradient and decrease out of slice signal [21]. The iterative predistortion method is advantageous because it is fast and simple to perform, and allows optimization at the scanner while the subject is in the magnet. Allowing the gradient to be re-optimized with every scan reduces

error from changes in eddy currents over time, and can be adjusted for any orientation or gradient shape desired.

The goal of this study was to implement AIR and DAFP sequences with half-pulse 2D UTE and compare results to previously validated 3D UTE methods. To evaluate the effectiveness and accuracy of the 2D UTE methods implemented here, we acquired 2D DAFP and AIR sequences in the tibia of healthy volunteers as well as already established 3D DAFP and AIR methods [11], [22] in the same subjects, and quantitatively compared resulting bound and pore water maps. The overall SNR efficiency of both methods was also compared.

5.2   Methods

5.2.1   Subjects

Three healthy volunteers (24M, 42M, 27M) underwent tibia scans on a 3T Philips Achieva scanner, with IRB approval and written informed consent. An 8 channel knee coil was used for receiving signal and a short T_2 reference marker with a known proton concentration was placed in the field of view (FOV) to allow maps of bound and pore water concentration to be converted to absolute units of mol ^{1}H/L$_{bone}$. Both 2D UTE with half-pulse excitation and 3D UTE with non-selective excitation were acquired on all subjects with AIR and DAFP preparations and were converted to bound and pore water concentration maps.

5.2.2   2D UTE Acquisition

The 2D UTE images were acquired using two half pulse acquisitions [13]. The RF pulse used was a 550 μs variable rate selective excitation (VERSE) pulse [23] of a half-Gaussian shape with a full width half maximum (FWHM) of 5 mm. A Gaussian shaped RF pulse, and in particular a VERSE Gaussian RF pulse, is the most commonly used pulse

for 2D UTE half pulse excitation [24]. A Gaussian shape has the shortest time bandwidth product, leading to the shortest pulse width and effectively shortest TE, as long pulses can lead to signal decay from short T_2 species during excitation. The VERSE pulse is used so that the RF pulse can end at the same time as the gradient pulse, so the RF pulse is played while the gradient ramps down.

The selective excitation was used with an optimized, bi-polar, smoothly varying slice select gradient. The slice select gradient had a maximum gradient strength of 23 mT/m, a maximum slew rate of 125 mT/m/ms, and a maximum acceleration of 1000 mT/m/ms^2, with a total length of 1.6 ms. The slice selective gradient was optimized for each subject during the scan session, by using the iterative pre-distortion method described by Harkins et al [21]. Briefly, the ideal gradient is applied and measured, using a modified Duyn's method [25], [26], and in the following iterations the applied gradient is modified to minimize the error between the measured gradient and the desired waveform. The maximum gradient constraints used were under the prescribed limits of the scanner, to help achieve lower errors with optimization. The root mean squared error (RMSE) between the ideal waveform and the measured waveform was minimized and took 3 to 5 iterations to converge to an average RMSE of 0.2%, with less than a minute between iterations. Figure 5.1 shows the ideal gradient waveform used on the left, and an example of how the error converges over iterations is shown on the right.

The 2D UTE scans were acquired with 200x200 mm FOV and 1.5 mm in plane resolution and 5 mm slice thickness. Acquisitions were read out in a center out fashion with golden angle spacing between acquired spokes to decrease coherent streaking in the image. The read out trajectory was measured on the x, y, and z axes (with the same method that was used to measure the slice selective gradient) to help reduce errors in the non uniform reconstruction, this was interpolated to all readout directions acquired. The two acquisitions using half pulses with opposite slice select gradient polarity were added during reconstruction for a full Gaussian slice profile. DAFP or AIR preparation pulses were used
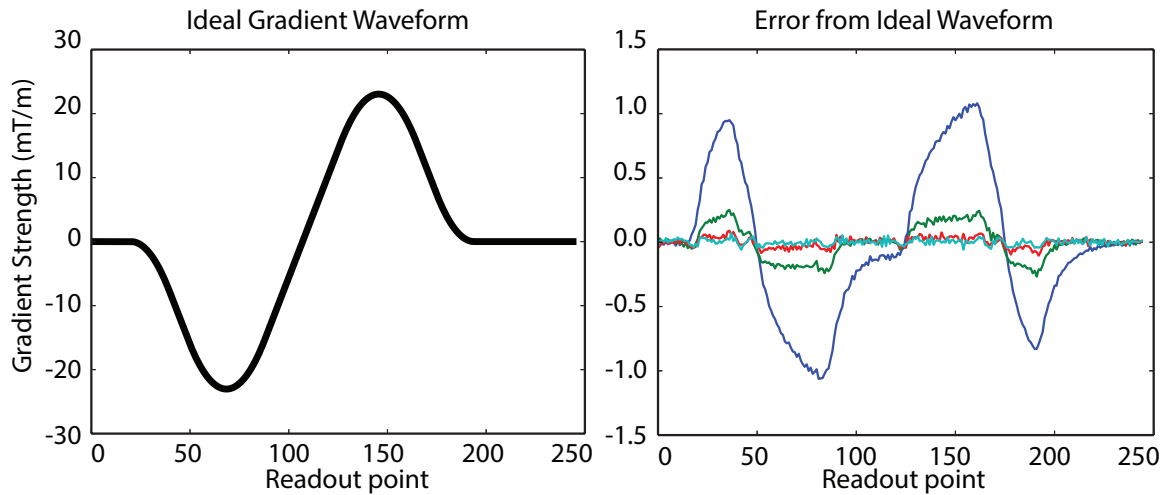
Figure 5.1: The ideal gradient waveform is shown on the left, and the first four iterations are shown on the right. The error is minimized within an RMSE of 0.2%. 1st iteration - blue, 2nd iteration - green, 3rd iteration - red, 4th iteration - cyan.

in combination with the 2D UTE excitation and radial readout. Similar to the previous 3D implementation, for every preparation pulse, 16 radial spokes were acquired, with a 3.2 ms spoke-to-spoke TR [11]. The flip angle was increased over the 16 radial spokes to achieve constant transverse magnetization throughout the acquisition. The echo time (TE) and repetition time (TR) of both DAFP and AIR scans was 70 μs/400 ms respectively, giving a scan time of 14 s per average for either the DAFP or AIR scans. To evaluate signal-to-noise ratio (SNR) needed for accurate signal quantification, 8 averages were acquired for each sequence, for a total scan time of 1 min 44 s for each scan. To compensate for any remaining unwanted out of slice signal, saturation slabs (the REigonal Saturation Technique (REST) in Philips software) were implemented on 2D DAFP scans to saturate signal on either side of the slice; this pulse was in the short span between the DAFP preparation pulse and the excitation train.

5.2.3 3D UTE Acquisition

For comparison, previously validated 3D UTE methods with a rectangular, 115 μs non-selective excitation pulse and 3D radial, center out readout was used in combination with DAFP and AIR preparation pulses. All scan parameters were similar to the 2D UTE when possible. The same trajectory measurements used for 2D reconstruction were used for the 3D reconstruction. The 3D scans had an isotropic FOV and resolution of 200mm/1.5 mm respectively, with a total scan time of 14 min each.

5.2.4 Evaluation of Quantitative Maps

Bound and pore water maps were derived from both 2D and 3D AIR and DAFP images using previously described signal equations [11]. A region of interest was found by segmenting the whole tibia in the slice, and for the 3D images, was averaged through the equivalent number of 2D slices.

Because 2D images had relatively low SNR, the bias from the Rician noise signal was significant and needed to be accounted for. This was done using a simple method described by Gudbjartsson et. al. [27]. Briefly, the true signal intensity A was estimated by the following postprocessing correction:

$$A = \sqrt{|M^2 - \sigma^2|} \tag{5.1}$$

where M is the measured signal intensity and σ is an estimate of the Rician noise. The noise was estimated as $\sigma = \mu_N / \sqrt{\pi/2}$, where μ_N was defined as the mean of a region of background signal. It is can be seen from Equation 5.1 that when SNR is relatively high ($M >> \sigma$), the difference between A and M is negligible, but in cases of low SNR, the noise will bias the magnitude of the signal intensity.

Differences between 2D and 3D maps were calculated on a subject by subject basis, and reported both in units of mol ^{1}H/L$_{bone}$ and as a percent error. The bound and pore

water concentrations were also evaluated with more averaging (up to 8 averages) for the 2D scans to evaluate SNR needed for reliable quanitfication.

5.3 Results

Figure 5.2 shows raw 2D AIR and DAFP images of the tibia and corresponding 3D AIR and DAFP images in the same slice. Qualitatively, the image contrasts look very similar, though the 2D images are significantly noisier. In one subject, RF spiking was present, so the artifacts were removed from k-space using a robust principal component analysis (RPCA) algorithm before reconstruction [28].

Figure 5.3 shows representative bound and pore water maps from the AIR and DAFP images in Figure 5.2. The bound and pore water measurements are generally in good agreement between 2D and 3D acquisitions.

An overview of all subjects is shown in Figure 5.4. The mean differences in bound and pore water concentrations between 2D and 3D across volunteers were 0.6 and 0.7 mol ^{1}H/L$_{bone}$ (2 / 9 %).

The mean SNR of the 2D and 3D sequences can be seen in Figure 5.5. SNR was defined as $\mu_S/(\mu_N/\sqrt{\pi/2})$, where μ_S is the mean signal in a region of cortical bone, and μ_N is background noise. The average 3D AIR scan SNR was 23, while the 1 average of the 2D scan had an average SNR of 3.0. When increasing to 8 averages, the SNR of the 2D scan increased to an average of 5.8. For the DAFP sequence, the mean SNR was 11 in the 3D scans and 2.3 in the 2D scan with 1 average. When increasing to 8 averages, the SNR went up to 5.0. Given these values of 2D SNR, if given an equivalent scan time to 3D scans, 2D AIR SNR should increase to approximately equivalent SNR of the 3D scans, so SNR efficiency is effectively the same for both methods.
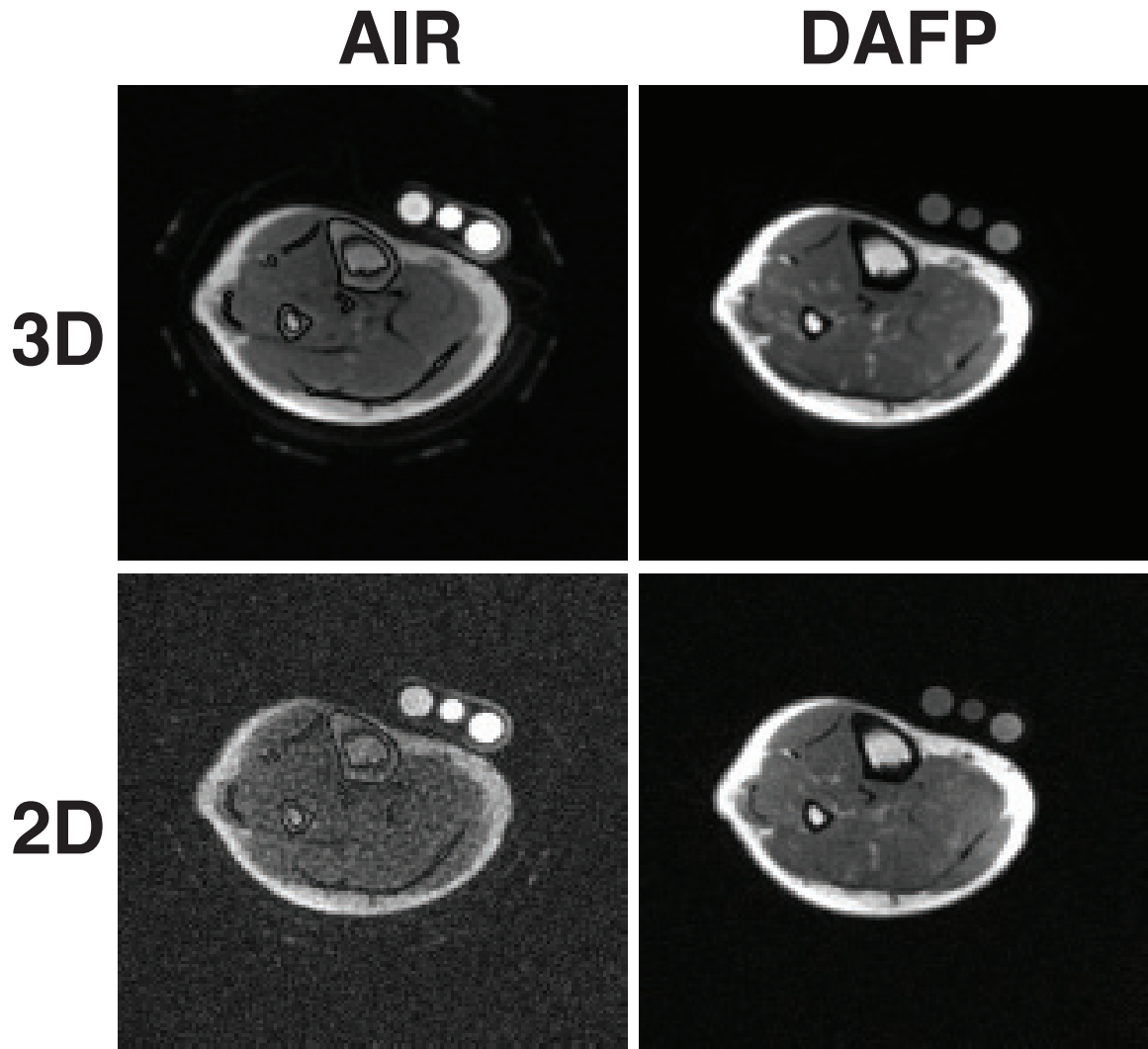
AIR **DAFP**

3D

2D

Figure 5.2: Representative images showing 3D (top) AIR and DAFP acquisitions and 2D acquisitions (bottom).

5.4   Discussion

These results show promising methods for decreasing scan time of bound and pore water MRI of bone. The differences in bound and pore water between 2D and 3D scans is small and is within the expected variation. The 2D method allows for faster images in a smaller FOV that could be useful in the future for evaluating fracture risk with MRI in a shorter scan time or in more areas. While the amount of information collected in a 2D scan is clearly much lower than that of a 3D scan, the 2D scan allows for flexibility in
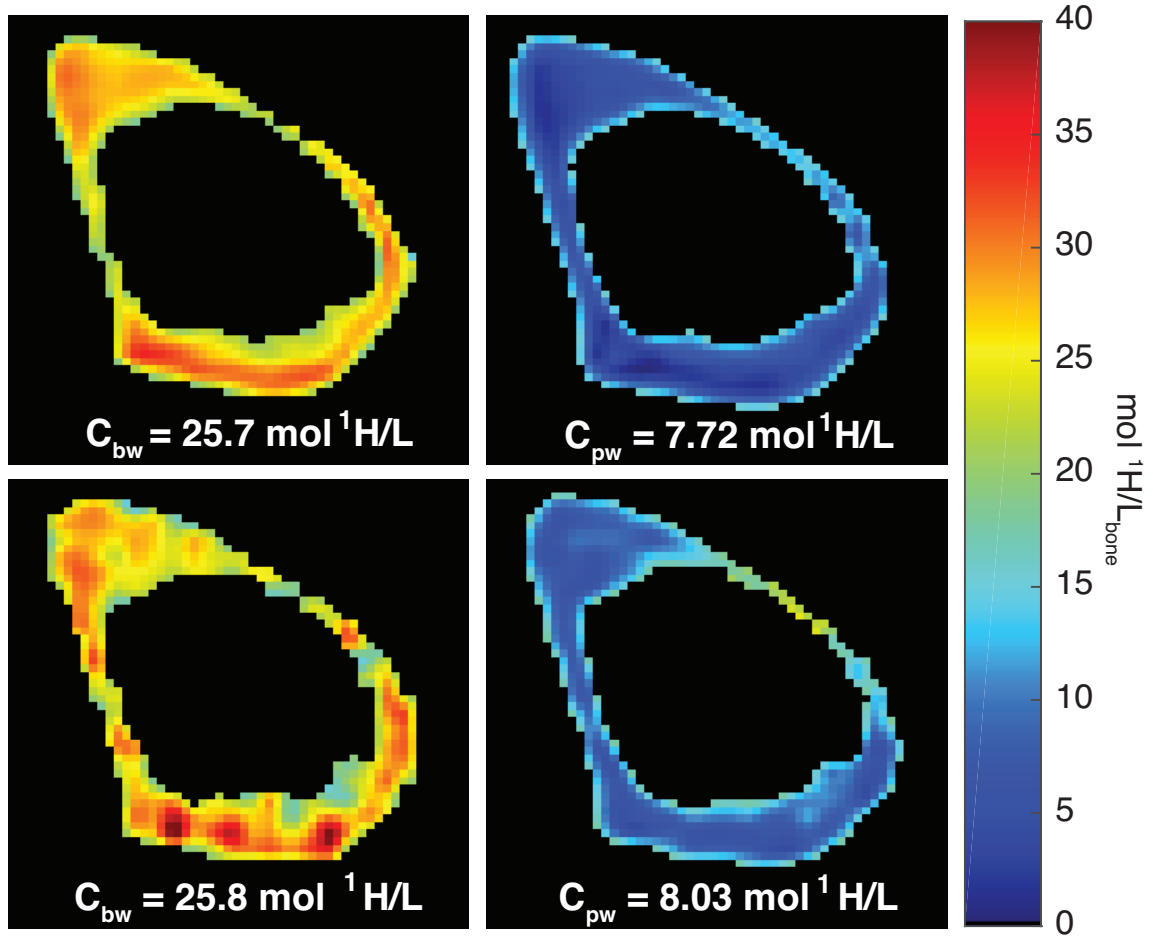
Figure 5.3: Representative tibia maps from 3D (top) AIR and DAFP acquisitions and 2D acquisitions (bottom). Mean bound (left) and pore (right) water values for the bone are shown below.

acquisitions that give it an advantage over 3D methods. For instance, the 2D method could be applied in bones that are very difficult to image with 3D UTE, such as the vertebrae or femoral neck. 2D methods also allow for higher in-plane resolution, since the resolution does not have to be isotropic.

While osteoporotic fractures do not usually occur in the tibia, osteoporosis is generally considered a systemic disease that affects bones of the entire body [12]. The tibia is an enticing area to apply 2D methods because the bound and pore water concentrations along the axis of a long bone vary relatively little, so 3D methods are not usually necessary. For
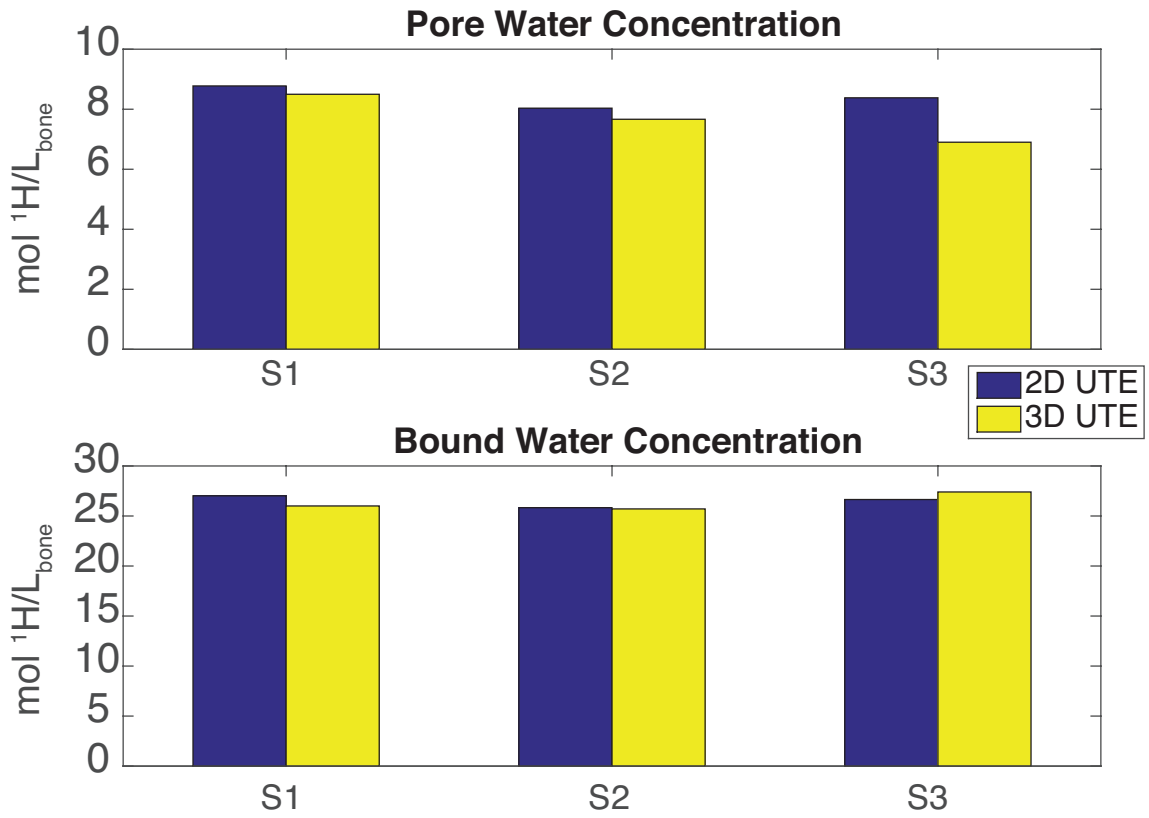
Figure 5.4: Differences between 3D and 2D bound and pore water concentrations in all subjects.
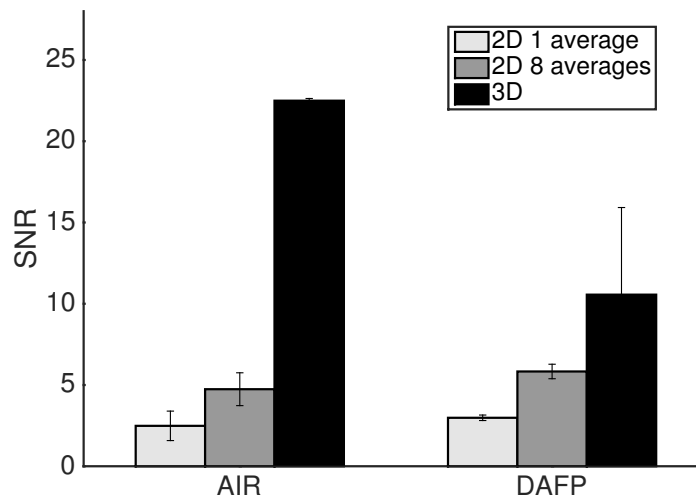

Figure 5.5: SNR from 3D AIR and DAFP scans, 2D scans, and 2D scans with 8 averages.

example, in Chapter 4, 3D acquisitions were acquired from ex vivo radii and compared to material properties of the bone. When looking at slices along the long axis of the radii, correlations between bound and pore water measurements and material properties did not change significantly when using mean bound and pore water measures found from different slices along the bone. The variation in concentration within the slice was found to be much more relevant to material properties.

The 2D UTE scans in this study had low SNR, and it was necessary to account for the noise contribution or average 2D scans so that the images would not be biased by noise signal. This is especially true in the case of the low signal of the DAFP images that results from healthy individuals having low pore water. While the SNR of the DAFP sequence may present less of a problem in typical osteoporotic patients that tend to have higher pore water, it is clear that these corrections can help to more accurately quantifying pore water concentration by reducing the error from 3D maps. Without the correction for bias, the mean differences in bound and pore water concentrations between 2D and 3D across volunteers were 3.3 and 2.6 mol ^{1}H/L$_{bone}$ (15/24 %). Using the correction resulted in much lower errors of 0.6 and 0.7 mol ^{1}H/L$_{bone}$ (2/9 %) for bound and pore water respectively. Averaging can also help reduce errors – when using 8 averages with no correction, (1 min 44 s scan time), the difference between bound/pore water concentration from 2D and 3D maps was 1.3/0.8 mol ^{1}H/L$_{bone}$ (5/10%).

It is also important that SNR be measured correctly – in this study (and all studies in this dissertation), a straightforward method for estimating the noise was used by finding the mean of the background, or air signal. However, methods using background signal to measure the noise are susceptible to errors from multiple coils, artifacts from low proton and short T_2 signals such as the coil itself, and streaking or coherent artifacts from the radial acquisition used here, which could result in inaccurate estimates of the noise. Alternative methods for measuring noise, including using a pixel-by-pixel standard deviation from re-peated acquisitions, finding the noise from a difference between two repeated acquisitions,

or acquiring a pure noise image [29] could help to achieve more accurate estimates of the noise, which is of particular importance when correcting for noise bias in the images.

The slice select gradient optimization is a key component to accurately quantifying concentration maps, as without this, the images have significant blurring and out of slice signal contamination. Additionally, the slice select gradient optimization needs to takes into account any predistortion that is incorporated into the generic gradient waveform. If the optimization only accounts for causal changes, the iterative method will converge at an error around 1% – almost an order of magnitude higher than the current predistortion method. This optimized slice select gradient still has room for improvement in design. For example, bipolar slice select gradients are used to help eliminate unwanted effects from eddy currents. However, since the gradient waveform is already being iteratively optimized, it is possible to only have a single direction gradient to help reduce the minimum TR.

Though the slice select gradient waveform used in the 2D UTE sequence was well optimized (RMSE < 0.2%), the slice profile still suffered from some out of slice signal effects. This was particularly a problem in the 2D DAFP sequence, which used a higher flip angle than the 2D UTE sequence and had more out of slice signal than the 2D AIR sequence. Though relatively small, there was a consistent bias in pore water concentration maps derived from the 2D scan that resulted in an increase in concentration compared to the concentrations derived from the 3D scan. To help with out of slice signal contamination, DAFP sequences used saturation slabs to saturate signal outside of the slice. This was added between the adiabtic prep pulse and the 16 excitation pulses, though alternatively, it could be added before the non-selective adiabatic pulses for the same effect. Adding the saturation pulses resulted in a delay time of 8 ms (the delay time used in previous studies was 5 ms). Other than adding this small delay between the prep pulse and the excitations, the saturation pulses were added with effectively no penalty – SNR between acquisitions with and without saturation slabs remained the same (between 2 and 3 both with and without saturation slabs). The longer the delay is between the prep pulse and

the excitations, the higher the risk of bound water signal recovering and contaminating the pore water acquisition, but this delay from the saturation slabs was minimal compared to the total delay from acquiring 16 shots at 3.2 ms a shot. The saturation pulses used in this sequence were the default pulses on the Philips scanner, but optimized out of slice saturation methods have also been proposed and could further help with out of slice signal issues [18]. However, since the slice select gradient in our work has already been optimized, this may not be necessary.

Some representative slice profiles with and without saturations slabs, and with and without an optimized slice select gradient can be seen in Figure 5.6. This slice profile is through a voxel in a copper sulphate phantom using the DAFP sequence. This emphasizes the importance of optimizing the gradient – without it, the total out of slice signal per voxel is 75% (71-78%) of the total in slice signal. When adding saturation slabs to the unoptimized pulse, this error drops to 21% (19-25%). With the optimized gradient, the out of slice signal is 17% (11-25%), and when adding the saturation slabs, the error is approximately 8% (6-12%). Another possible reason for out of slice signal contamination is partial volume averaging resulting from the low time-bandwidth product of the RF pulse. While RF pulses for 2D half pulse UTE typically use Gaussian pulses to achieve a short pulse and minimize the effective TE, the optimization of the excitation pulse could help further reduce out of slice signal contamination.

Another method to help with out of slice signal is to implement a non-selective $90°$ pulse at the end of the train of excitations in every TR. This allows both in slice and out of slice signal to begin at the same longitudinal magnetization (zero) for each recovery period. This method was implemented and tested, and while it does effectively decrease out of slice signal (similar performance as saturation slabs), it results in an SNR penalty compared to the steady state of the typical method (effective flip angle of $60°$). Therefore, for this study we chose to use the saturation slabs, however the non-selective $90°$ pulse method has some advantages and could be explored in future studies. For example, saturation slabs
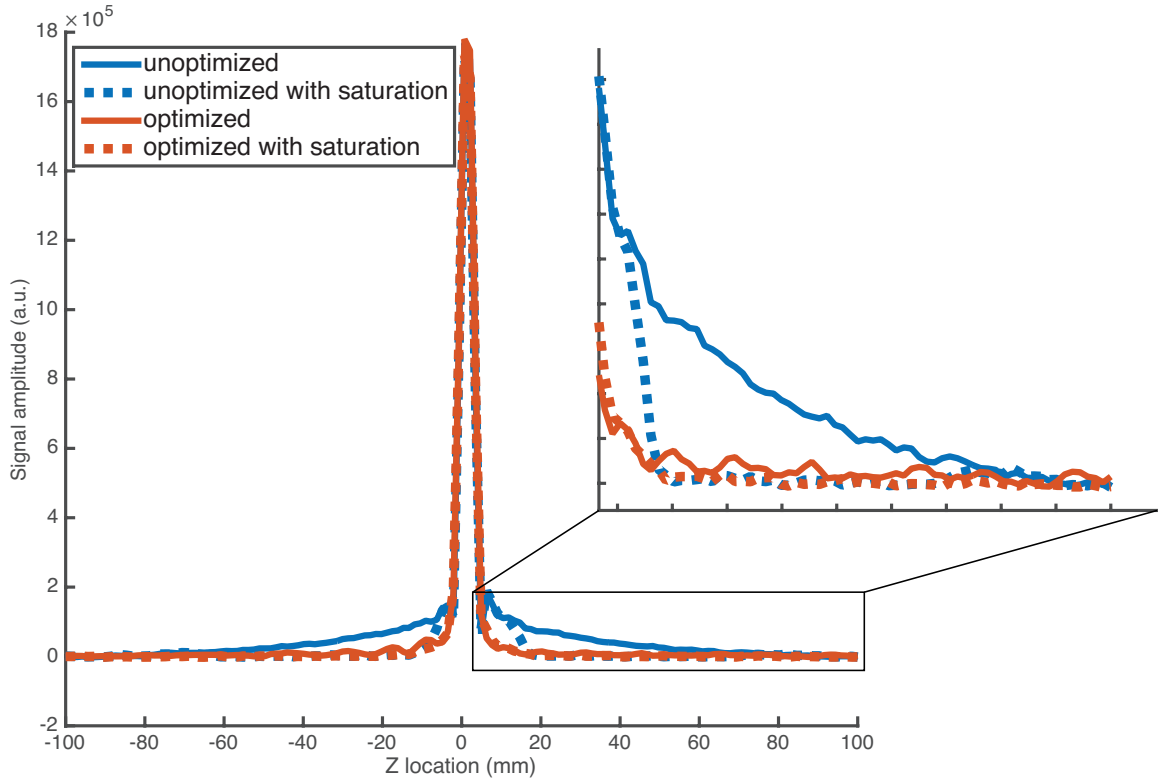
Figure 5.6: Slice profile shown for both unoptimized (blue) and optimized (red) acquisitions, with and without the saturation slabs. Inset shows zoomed in section of slice profiles where the suppression of out of slice signal from the saturation slabs is apparent.

need to have sharp slice profiles that are close to the slice of interest, and could also result in unwanted magnetization transfer effects, so using a non-selective 90° pulse could be advantageous to avoid these issues and still reduce out of slice signal contamination.

While out of slice signal primarily comes from gradient imperfections, another potential source of out of slice signal for the DAFP acquisition is from flow. The water in the pore space of the bone is partially due to blood volume inside the Haversian canals. Blood flow in cortical bone varies and is generally poorly understood, but is known to change in response to loading [30]. Flow of pore water into the slice during acquisition could result in an unwanted increase in pore water signal. The 2D methods were tested against 3D methods in ex vivo cadaveric bones with no flow, and found similar, small, increases in pore water concentration in 2D scans, suggesting that the error is predominantly from

imperfect slice profiles rather than flow. However, it is important to be aware of potential confounding results from flow contamination to avoid errors in pore water quantification. The saturation slabs for out of slice signal suppression can help flow effects to some degree, though depending on the speed of flow, will not be able to saturate all incoming flow. The non-selective 90° pulse would also help to eliminate artifacts caused by flow as well as helping to suppress other unwanted out of slice signal.

To show the sensitivity of the 2D DAFP method in particular, Figure 5.7 shows the same DAFP acquisition acquired on an individual in one scan session. From this figure, it is clear that adding a saturation slab or using a non-selective pulse can alter the quantitative maps, and help bring values closer to 3D results. Over the three subjects, the saturation slabs and the non-selective 90° methods both decreased pore water concentration by an average of 1 mol ^{1}H/L$_{bone}$ compared to no out of slice signal compensation, halving the error relative to 3D DAFP. In addition, using an acquisition without golden angle spacing between acquired spokes and instead acquiring spokes by stepping linearly around the radial k-space has the potential to further contaminate quantitative maps with coherent streaking.

3D DAFP   **2D DAFP with saturation**   **2D DAFP with non-selective 90**

PW = 8.5 mol ^{1}H/L   PW = 8.67 mol ^{1}H/L   PW = 9.4 mol ^{1}H/L

2D DAFP   **2D DAFP no golden angle**
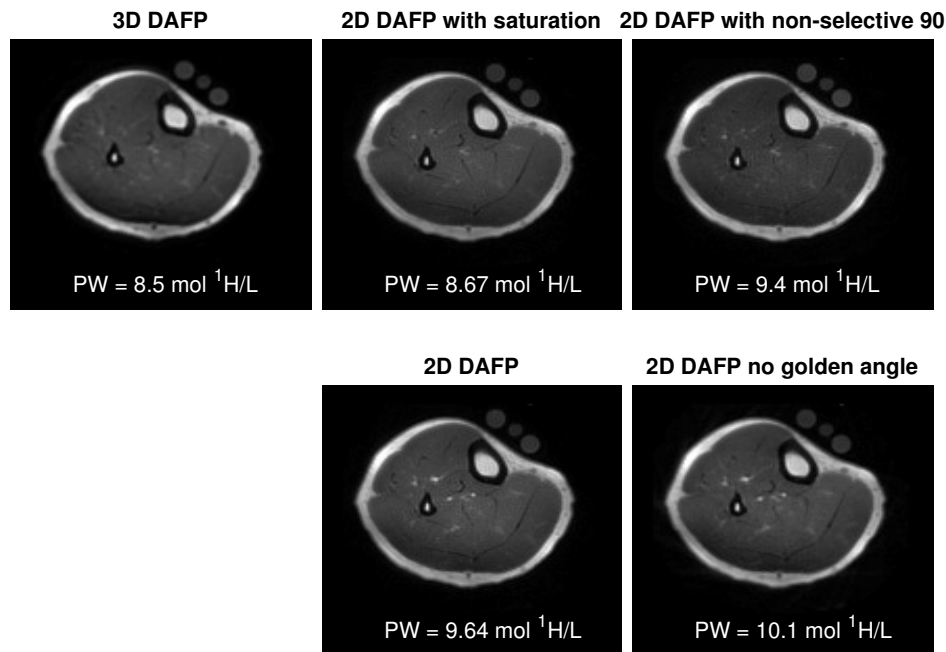
PW = 9.64 mol ^{1}H/L   PW = 10.1 mol ^{1}H/L

Figure 5.7: Images acquired from a subject with 3D DAFP (left) and several 2D DAFP variations. Top left - 2D DAFP with saturation slabs, top right - 2D DAFP with a non-selective 90°, bottom left - 2D DAFP with no out of slice signal corrections, and bottom right - 2D DAFP without golden angle acquisitions and no out of slice signal corrections.

Overall, one should exercise caution when using 2D UTE methods for quantification and be aware of possible pitfalls to avoid errors in measurements. Additional improvements, such as a combination of both the saturation slabs and the non-selective 90° could help to reduce errors further. In this study, saturation was only applied in the DAFP sequence, since the AIR sequence had comparably much lower percentages of errors. However, AIR slice profiles also exhibited some out of slice signal, though even without saturation slabs, this error was around 10%. It would be straightforward to also acquire the AIR sequence with the non-selective pulse, or with saturation slabs, though in this case magnetization transfer effects could possibly interfere with bound water quantification [5]. Further errors in bound water concentration could come from relaxation during the excitation pulse due to the short T_2 of bound water [24]. For the 2D sequence here, bound water

signal will be around 80% of its nominal value while the 3D sequence only leads to bound water signal of around 90% [31], which could lead to an underestimation in the true bound water concentration. Ultimately, the errors between 2D and 3D concentrations are well below the standard error of repeatability found in Chapter 3, which was approximately 2 mol ^{1}H/L$_{bone}$.

In conclusion, applying these fast DAFP and AIR sequences in 2D has the potential to greatly increase the utility of these methods in clinical settings for evaluating fracture risk in patient populations. While the amount of information collected in a 2D scan is much lower than that of a 3D scan, acquiring only 2D data allows for increased flexibility in the scan parameters. The 2D UTE method could also be applied in other bones that are difficult to image with 3D UTE, such as the vertebrae or femoral neck, which are highly associated with fracture risk.

5.5 References

[1] M. A. Fernández-Seara, S. L. Wehrli, M. Takahashi, and F. W. Wehrli, "Water content measured by proton-deuteron exchange nmr predicts bone mineral density and mechanical properties.," *J Bone Miner Res*, vol. 19, no. 2, pp. 289–96, Feb. 2004.

[2] R. A. Horch, D. F. Gochberg, J. S. Nyman, and M. D. Does, "Non-invasive predictors of human cortical bone mechanical properties: t(2)-discriminated h nmr compared with high resolution x-ray.," *PloS one*, vol. 6, no. 1, e16359, Jan. 2011.

[3] W. C. Bae, P. C. Chen, C. B. Chung, K. Masuda, D. D'Lima, and J. Du, "Quantitative ultrashort echo time (ute) mri of human cortical bone: correlation with porosity and biomechanical properties.," *J Bone Miner Res*, vol. 27, no. 4, pp. 848–57, Apr. 2012.

[4] M. K. Manhard, S. Uppuganti, M. Granke, D. F. Gochberg, J. S. Nyman, and M. D. Does, "Mri-derived bound and pore water concentrations as predictors of fracture resistance," *Bone*, vol. 87, pp. 1–10, 2016.

[5] R. A. Horch, J. S. Nyman, D. F. Gochberg, R. D. Dortch, and M. D. Does, "Characterization of 1h nmr signal in human cortical bone for magnetic resonance imaging.," *Magn Reson Med*, vol. 64, no. 3, pp. 680–7, Sep. 2010.

[6] J. S. Nyman, Q. Ni, D. P. Nicolella, and X. Wang, "Measurements of mobile and bound water by nuclear magnetic resonance correlate with mechanical properties of bone.," *Bone*, vol. 42, no. 1, pp. 193–9, Jan. 2008.

[7] W. H. Organization, "Who scientific group on the assessment of osteoporosis at primary health care level," World Health Organization, Brussels, Belgium, Tech. Rep., 2004.

[8] A. Techawiboonwong, H. K. Song, M. B. Leonard, and F. W. Wehrli, "Cortical bone water: in vivo quantification with ultrashort echo-time mr imaging," *Radiology*, vol. 248, no. 3, pp. 824–833, 2008.

[9] R. A. Horch, D. F. Gochberg, J. S. Nyman, and M. D. Does, "Clinically compatible mri strategies for discriminating bound and pore water in cortical bone.," *Magn Reson Med*, vol. 68, no. 6, pp. 1774–84, Dec. 2012.

[10] J. Du, J. C. Hermida, E. Diaz, J. Corbeil, R. Znamirowski, D. D. D'Lima, and G. M. Bydder, "Assessment of cortical bone with clinical and ultrashort echo time sequences.," *Magn Reson Med*, vol. 70, pp. 697–704, Sep. 2013.

[11] M. K. Manhard, R. A. Horch, K. D. Harkins, D. F. Gochberg, J. S. Nyman, and M. D. Does, "Validation of quantitative bound- and pore-water imaging in cortical bone.," *Magn Reson Med*, vol. 71, no. 6, pp. 2166–2171, Jul. 2014.

[12] J. Kanis, "Diagnosis of osteoporosis and assessment of fracture risk.," *Lancet*, vol. 359, no. 9321, pp. 1929–36, Jun. 2002.

[13] J. Pauly, S. Conolly, and D. G. Nishimura, "Slice-selective excitation for very short t2-species," in *Proc. Intl. Soc. Magn. Reson. Med.*, 1989, p. 28.

[14] M. D. Robson, P. D. Gatehouse, M. Bydder, and G. M. Bydder, "Magnetic resonance: an introduction to ultrashort te (ute) imaging," *J Comput Assist Tomo*, vol. 27, no. 6, pp. 825–846, 2003.

[15] P. Gatehouse and G. Bydder, "Magnetic resonance imaging of short t2 components in tissue," *Clinical Radiology*, vol. 58, no. 1, pp. 1–19, Jan. 2003.

[16] I. C. Atkinson, A. Lu, and K. R. Thulborn, "Characterization and correction of system delays and eddy currents for mr imaging with ultrashort echo-time and time-varying gradients.," *Magn Reson Med*, vol. 62, no. 2, pp. 532–7, Aug. 2009.

[17] S. Josan, J. M. Pauly, B. L. Daniel, and K. B. Pauly, "Double half rf pulses for reduced sensitivity to eddy currents in ute imaging.," *Magn Reson Med*, vol. 61, no. 5, pp. 1083–9, May 2009.

[18] S. Josan, E. Kaye, J. M. Pauly, B. L. Daniel, and K. B. Pauly, "Improved half rf slice selectivity in the presence of eddy currents with out-of-slice saturation.," *Magn Reson Med*, vol. 61, no. 5, pp. 1090–5, May 2009.

[19] K. D. Harkins, R. A. Horch, and M. D. Does, "Simple and robust saturation-based slice selection for ultrashort echo time mri," *Magn Reson Med*, vol. 73, pp. 2204–2211, 2015.

[20] T. Abe, "Half radiofrequency pulse excitation with a dedicated prescan to correct eddy current effect and gradient delay," *Medical Physics*, vol. 40, no. 032304, 2013.

[21] K. D. Harkins, M. D. Does, and W. A. Grissom, "Iterative method for predistortion of mri gradient waveforms," *IEEE T Med Imaging*, vol. 33, no. 8, pp. 1641–1647, 2014.

[22] M. K. Manhard, R. A. Horch, D. F. Gochberg, J. S. Nyman, and M. D. Does, "In vivo quantitative mr imaging of bound and pore water in cortical bone," *Radiology*, vol. 277, no. 1, pp. 221–229, 2015.

[23] S. Conolly, D. Nishimura, and A. Macovski, "Variable-rate selective excitation," *J Magn Reson*, vol. 458, pp. 440–458, 1988.

[24] M. D. Robson and P. D. Gatehouse, "Consequences of t2 relaxation during half-pulse slice selection for ultrashort te imaging.," *Magn Reson Med*, vol. 64, no. 2, pp. 610–5, Aug. 2010.

[25] J. H. Duyn, Y. Yang, J. a. Frank, and J. W. van der Veen, "Simple correction method for k-space trajectory deviations in mri.," *J Magn Reson*, vol. 132, no. 1, pp. 150–3, May 1998.

[26] P. Gurney, J. Pauly, and D. G. Nishimura, "A simple method for measuring b0 eddy currents," *Proc. Intl. Soc. Magn. Reson. Med. 13*, p. 866, 2005.

[27] H. Gudbjartsson and S. Patz, "The rician distribution of noisy mri data," *Magnetic Resonance in Medicine*, vol. 34, pp. 910–914, 1995.

[28] A. E. Campbell-Washburn, D. Atkinson, Z. Nagy, R. W. Chan, O. Josephs, M. F. Lythgoe, R. J. Ordidge, and D. L. Thomas, "Using the robust principal component analysis algorithm to remove rf spike artifacts from mr images," *Magn Reson Med*, pp. 1–9, 2015.

[29] O. Dietrich, J. G. Raya, S. B. Reeder, M. F. Reiser, and S. O. Schoenberg, "Measurement of signal to noise ratios in mr images, influence of multichannel coils, parallel imaging, and reconstruction filters.," *J Magn Reson Img*, vol. 26, no. 2, pp. 375–85, Aug. 2007.

[30] S. C. Cowin, "Bone poroelasticity.," *Journal of biomechanics*, vol. 32, no. 3, pp. 217–38, Mar. 1999.

[31] A. Techawiboonwong, H. K. Song, and F. W. Wehrli, "In vivo mri of submillisecond t 2 species with two-dimensional and three-dimensional radial sequences and applications to the measurement of cortical bone water," *NMR Biomed*, vol. 21, pp. 59–70, 2008.

Chapter 6

Applying Bound and Pore Water MRI of Cortical Bone in Osteoporotic Patients

6.1 Introduction

Osteoporotic fractures are a growing problem worldwide, especially with the increase in the aging population and the increase of type II diabetes, both of which are highly associated with fractures [1], [2]. Methods to diagnose and treat osteoporosis are extremely important in preventing fractures, as without proper treatment, this disease has high rates of morbidity and mortality [3].

Current methods for evaluating fracture risk primarily measure bone mineral density (BMD), usually assessed from Dual X-ray Energy Absorptiometry (DXA). While this fast and inexpensive method is the current single leading predictor of fracture risk in the clinic [4], DXA does not identify many individuals who are at risk of a fracture. This is a particularly problem with the known under-diagnosed increase in fractures that occur with aging [1]. Furthermore, it is not always clear how well a patient is responding to particular drug treatment. There is an overall need for an improvement in diagnostic methods of bone health.

MRI based methods are a more recent, promising detector of fracture risk that report on a different material component of bone than BMD. BMD reflects the mineral portion of bone. MRI methods can evaluate cortical bone by assessing the amount of water bound to the collagen matrix (bound water), or by assessing the water in the pore space in cortical bone (pore water) [5]. Relaxation selective MRI-derived bound and pore water measures in cortical bone have previously been implemented in vivo on a 3T Philips scanner in both the tibia and the radius on healthy volunteers, and shown good repeatability [6]. While MRI bound and pore water concentrations have shown ability to predict fracture resistance of ex vivo bone samples [7], [8], the sensitivity of the method in clinical populations is currently

unknown.

The goal of this work is to evaluate bound and pore water measures acquired in the tibia from individuals recently diagnosed with osteoporosis. DXA measurements, the gold standard, were also acquired on these osteoporotic subjects from the hip, spine, and radius, as well as a trabecular bone score map (TBS) [9] found from the DXA spine image. Finally, we compared bound and pore water concentrations measurements from the osteoporotic volunteers with measurements from healthy individuals with no history of bone disease.

6.2 Methods

6.2.1 Subjects

All subjects were recruited with IRB approval and written informed consent. The osteoporotic volunteers (9 female, mean age 63 (range 58-73)) were individuals that had been recently diagnosed with osteoporosis and were beginning a new drug treatment. Treatments included teriparatide, denosumab, alendronate and zoledronate. Subjects were scanned with both MRI and DXA measurements on the same day; scans took place within two weeks of the start of the drug treatment. In 2 of the 9 cases, DXA measurements were not acquired as subjects already had DXA performed by their local doctor within the past week. Those results were not included in our DXA analysis.

Healthy subjects (6 male/7 female, mean age 34 (range 24-68)) were also recruited for comparison and had MRI scans only (no DXA scans were acquired on the healthy controls). The same MRI protocol was used on both healthy and osteoporotic subjects.

6.2.2 DXA Acquisitions

Standard clinical DXA scans were acquired on the forearm, spine, and hip from each osteoporotic subject using a GE Lunar iDXA system. Measures of areal BMD were found from these scans after quality assurance performed by a clinical densiometrist. From the

forearm scan, the aBMD in the distal third radius was analyzed. From the hip scan, the aBMD from both the total femur and the femoral neck was used in further analysis. From the spine scan, total aBMD from the L1-L4 vertebrae was found – in some cases, one or more vertebrae were excluded because of poor image quality or artifacts from degenerative disk disease. In such cases, average BMD was found in the spine from the remaining vertebrae. All BMD measures were also reported as T-scores, as this is the common way to discuss DXA results clinically. Osteoporosis is diagnosed as having a T-score of -2.5 or lower in at least one of the sites measured (spine, hip, forearm). A trabecular bone score map was derived from the spine DXA scan using TBS iNsight software.

6.2.3 MRI Acquisitions

The Adiabatic Inversion Recovery (AIR) and Double Adiabatic Full Passage (DAFP) sequences were used with 3D UTE to measure bound and pore water concentrations, respectively, in the cortical bone in the tibia. Conventional UTE sequences were also acquired on all subjects. As in previous studies, a reference marker was placed in the FOV so that signal could be converted into absolute units of mol ^{1}H/L$_{bone}$ and compared across subjects. The scans were acquired at a 200 mm isotropic FOV with 1.5 mm resolution in a scan time of 14 minutes each. A B_1^- map was found by acquiring a T_1 weighted scan twice, once using the body coil for receive and once with the knee coil for receive. The smoothed ratio of the signal was then applied to the images. Bound and pore water concentration maps were found using signal equations, as described in previous work [8], [10]. The mean bound and pore water values found from a 14 mm thick section of the tibial midshaft tibia were used for further analysis.

6.2.4 Statistical Analysis

To compare MRI results between osteoporotic and healthy subjects, a t-test was used to evaluate differences in bound and pore water concentrations. Differences in concentrations

between groups with a p-value<0.05 were considered significant. MRI derived bound and pore water concentrations were correlated to DXA derived aBMD/T-scores and TBS measures using Pearson's R correlation coefficients.

6.3   Results

Figure 6.1 shows a representative bound and pore water map overlaid on a conventional UTE image from a healthy control and from an osteoporotic subject. In this image, it is clear the variation in concentration within the bone in the slice is relatively small compared to the variation between these two subjects. The bound water concentration is much higher in the healthy tibia compared to the osteoporotic tibia, while the pore water is much lower in the healthy control compared with the osteoporotic tibia.

Figure 6.2 shows the mean bound and pore water concentrations across both healthy and osteoporotic subjects. The healthy subjects had a mean bound/pore water concentrations of 26/10 mol ^{1}H/L$_{bone}$. The osteoporotic subjects had a mean bound/pore water concentrations of 17/14mol ^{1}H/L$_{bone}$. A significant decrease in bound water ($p < 0.001$) and a significant increase in pore water ($p = 0.03$) was shown in the osteoporotic subjects compared to the healthy subjects. The changes between healthy and osteoporotic subjects were in the expected directions based known correlations between bound and pore water measures and bone material properties [7], [8], [11].

Figure 6.3 shows a representative DXA image from the forearm, hip, and spine as well as the TBS map. Lines in the images show reference points used by the software to help technologists and clinicians define the area in which to calculate BMD. In this case, the distal third radius BMD was 0.763 g/cm^2 (T-score of -1.3), the total hip BMD was 0.662 g/cm^2 (T-score of -2.8), and the vertebrae BMD was 0.863 g/cm^2 (T-score of -2.7). The TBS was 1.194 for this subject. Overall, baseline T-scores ranged from -2.9 to -1.4 in the total femur, -2.9 to -1.5 in the femoral neck, -4.1 to -0.4 in the distal third radius, and -3.0 to 0.9 in the vertebrae. TBS scores ranged from 1.1 to 1.4.
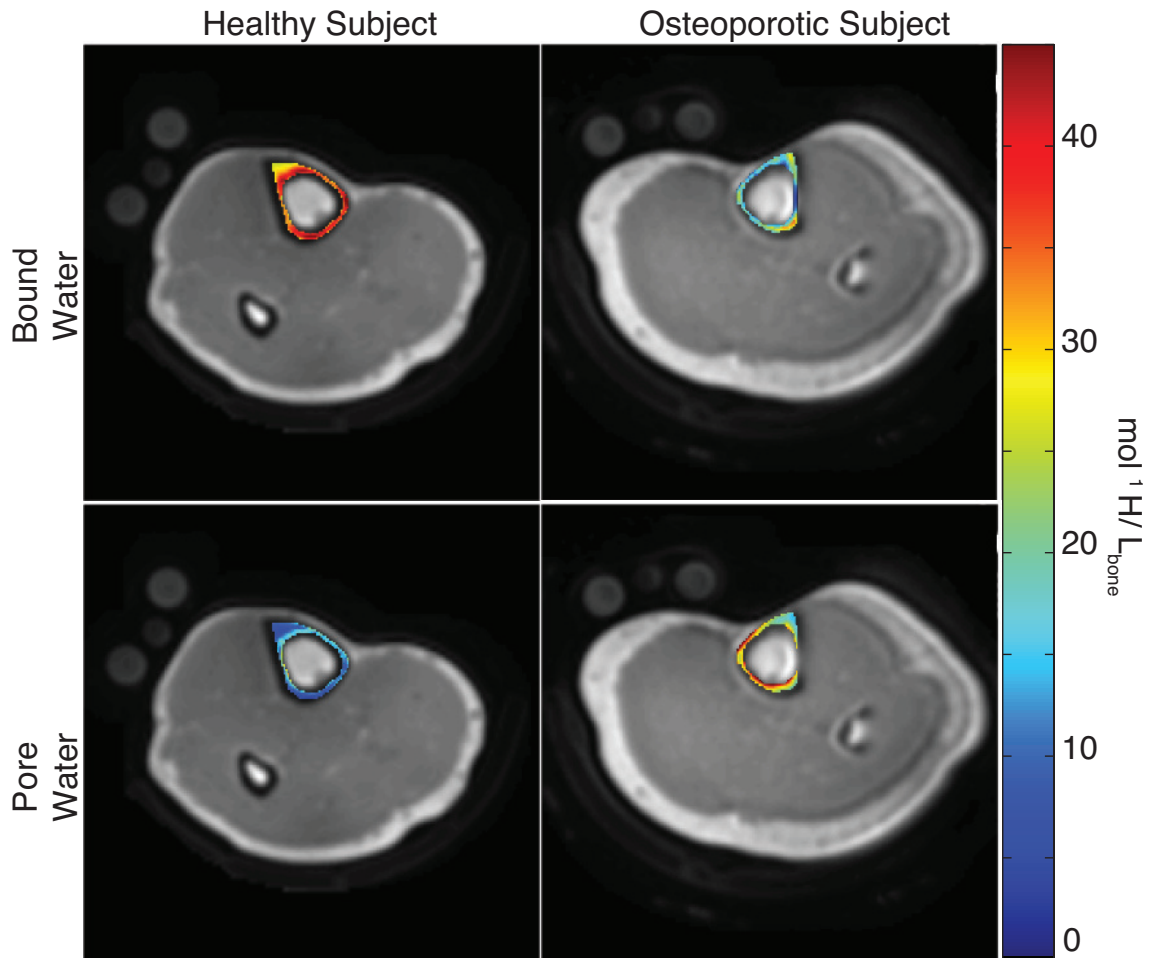
Figure 6.1: Representativie UTE images of the lower leg in both a healthy (left) and osteoporotic (right) subject. Bound (top) and pore (bottom) water concentration maps are overlaid.

Figure 6.4 shows select linear correlations between MRI and DXA measurements. TBS was not significantly correlated with any MRI concentrations or DXA BMD. Bound water concentration correlated only with the total hip T-score, while pore water concentration was close to significantly correlated with the total hip T-score. Bound and pore water concentrations did not significantly correlate with any other DXA T-score measurements. Bound and pore water concentrations from MRI were inversely correlated (R = -0.84, p < 0.05).
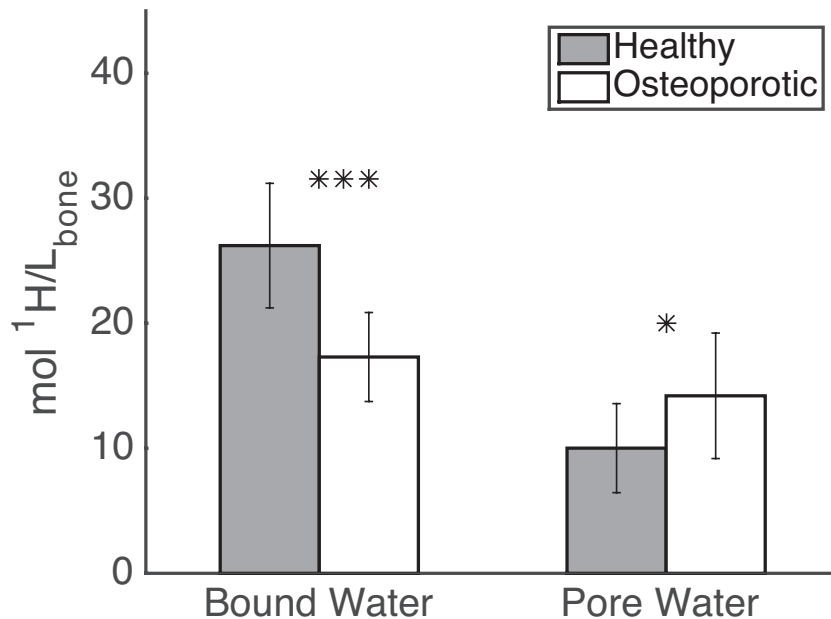
Figure 6.2: Mean bound and pore water concentrations in both healthy controls and osteoporotic subjects. Bound water was significantly lower (p<0.001) while pore water (p<0.05) was significantly higher in osteoporotic subjects.

6.4 Discussion

These results demonstrate that MRI measures of bound and pore water using AIR and DAFP are sensitive enough to detect differences between normal and osteoporotic bone. The results show expected changes with osteoporosis, which is promising for future studies using these methods for evaluating fracture risk. The results support the hypothesis that low bound water is a marker of poor bone quality, which has been associated with low fracture resistance [7], [8], [11], [12]. The pore water also increases with osteoporosis as pore water is a marker of porosity and has been shown to correlate with porosity from uCT [8].

MRI measurements in tibial cortical bone correlated with the total hip T-scores using DXA, which is consistent with the largely cortical content of the total hip. MRI measures did not correlate with TBS scores, which is derived from the texture of trabecular bone scans. TBS and MRI measures are reporting on very different properties of the bone, and
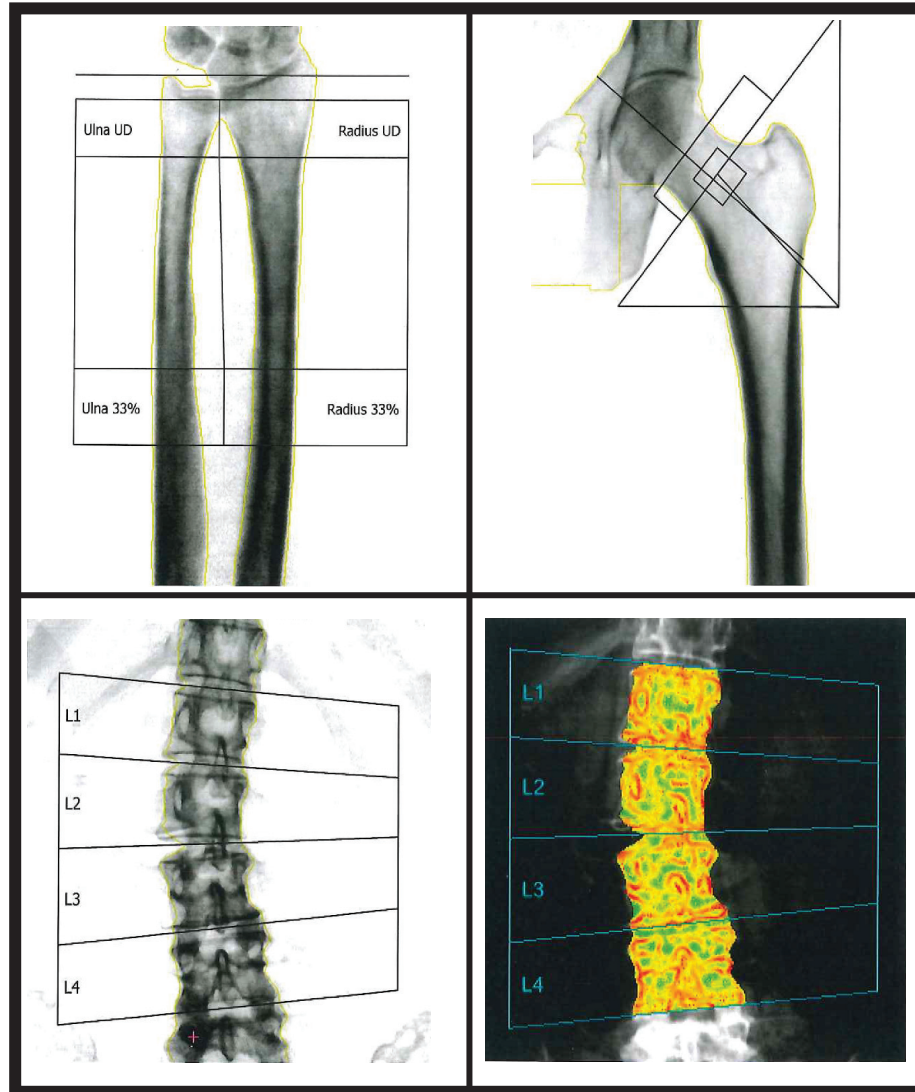
Figure 6.3: Overview of DXA scans acquired on osteoporotic subjects. BMD values and T-scores were found in the distal third radius from the forearm (top left), the proximal femur (top right), and the L1-L4 vertebrae (bottom left). TBS maps were derived from the spine DXA (bottom right).

therefore it is not surprising that TBS did not correlate with MRI measures. Bound and pore water concentrations were inversely correlated, which agrees with previous literature [7], [8], [13].

Overall, the results in this study are promising as a preliminary application of these methods to a relevant population. Future clinical studies will be needed to fully evaluate
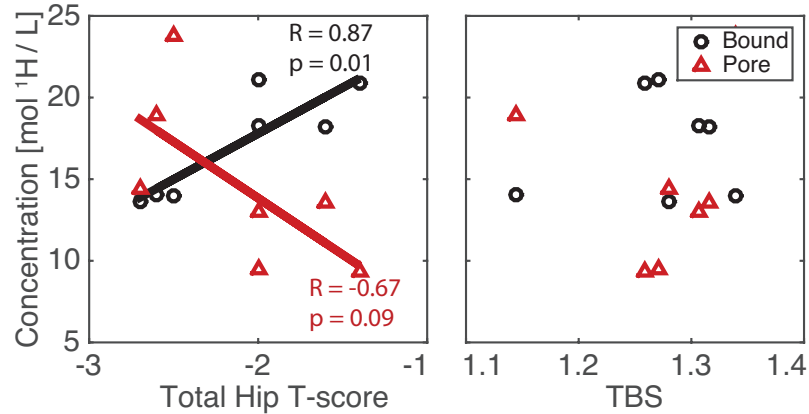
Figure 6.4: Correlations between MRI bound and pore water concentrations and DXA derived T-score from the femur (left) and TBS score (right). Bound and pore water correlated with the femur T-score but did not correlate with TBS.

the diagnostic capability of these MRI methods in enhancing fracture risk predictions. A particularly important question is whether these MRI measurements change with osteoporosis in a way that is different from BMD or TBS changes. This work is ongoing, and MRI and DXA measurements will be collected on the osteoporotic volunteers at 6 months and 1 year following the start of drug treatment. This will enable evaluation of the extent to which changes can be detected with the MRI measurements in response to drug treatment, and will allow comparison of MRI results with those found from DXA.

Other clinical populations are also of interest for the MRI bound and pore water concentration measurements. One area of interest is collecting bound and pore water measurements in patients that have recently had fracture. Currently, we are collecting these measurements in two groups - high energy fracture (e.g. trauma) and low energy fracture (e.g. fall from standing). Low energy fractures are common with diseases such as osteoporosis, and are generally associated with those who are at high fracture risk [14]. Evaluating differences in bound and pore water concentrations between these groups may help to better understand how these MRI measurements can be used in diagnosing fracture risk.

Another cohort that would be useful to measure and that has great potential for the MRI measurement are patients with type II diabetes, which is known as an independent risk factor for fracture [2]. This is hypothesized to be because of abnormal cross-linking in the collagen matrix of the bone that leads to brittle bone [2]. Since the MRI methods presented here measure the water bound to the collagen matrix with the AIR method, this has the potential to be sensitive to change in cross-linking. This is particularly important for type II diabetes because fracture risk is often undetected with DXA – BMD levels remain high and can sometimes even increase, despite the higher risk of fracture [15].

In conclusion, the findings from this study are an important step in applying the MRI bone measures to clinically relevant populations. Future studies investigating bound and pore water measurements will allow for further investigation of differences of bound and pore water measures across diseases and changes of bound and pore water with response to various drug treatment methods.

6.5 References

[1] J. Kanis, O. Johnell, A. Oden, A. Dawson, C. De Laet, and B. Jonsson, "Ten year probabilities of osteoporotic fractures according to bmd and diagnostic thresholds," *Osteoporosis Int.*, vol. 12, no. 12, pp. 989–995, 2001.

[2] W. D. Leslie, M. R. Rubin, A. V. Schwartz, and J. a. Kanis, "Type 2 diabetes and bone.," *J Bone Miner Res*, vol. 27, no. 11, pp. 2231–7, Nov. 2012.

[3] C. Cooper, E. J. Atkinson, S. J. Jacobsen, W. M. O. Fallon, and L. J. M. Iii, "Population-based study of survival after osteoporotic fractures," *American Journal of Epidemiology*, vol. 137, no. 9, pp. 1001–1005, 1993.

[4] W. H. Organization, "Who scientific group on the assessment of osteoporosis at primary health care level," World Health Organization, Brussels, Belgium, Tech. Rep., 2004.

[5] R. A. Horch, J. S. Nyman, D. F. Gochberg, R. D. Dortch, and M. D. Does, "Characterization of 1h nmr signal in human cortical bone for magnetic resonance imaging.," *Magn Reson Med*, vol. 64, no. 3, pp. 680–7, Sep. 2010.

[6] M. K. Manhard, R. A. Horch, D. F. Gochberg, J. S. Nyman, and M. D. Does, "In vivo quantitative mr imaging of bound and pore water in cortical bone," *Radiology*, vol. 277, no. 1, pp. 221–229, 2015.

[7] R. A. Horch, D. F. Gochberg, J. S. Nyman, and M. D. Does, "Non-invasive predictors of human cortical bone mechanical properties: t(2)-discriminated h nmr compared with high resolution x-ray.," *PloS one*, vol. 6, no. 1, e16359, Jan. 2011.

[8] M. K. Manhard, S. Uppuganti, M. Granke, D. F. Gochberg, J. S. Nyman, and M. D. Does, "Mri-derived bound and pore water concentrations as predictors of fracture resistance," *Bone*, vol. 87, pp. 1–10, 2016.

[9] T. Piveteau, R. Winzenrieth, and D. Hans, "Trabecular bone score (tbs) the new parameter of 2d texture analysis for the evaluation of 3d bone micro architecture status," *Bone*, vol. 48, S176, May 2011.

[10] M. K. Manhard, R. A. Horch, K. D. Harkins, D. F. Gochberg, J. S. Nyman, and M. D. Does, "Validation of quantitative bound- and pore-water imaging in cortical bone." *Magn Reson Med*, vol. 71, no. 6, pp. 2166–2171, Jul. 2014.

[11] J. S. Nyman, Q. Ni, D. P. Nicolella, and X. Wang, "Measurements of mobile and bound water by nuclear magnetic resonance correlate with mechanical properties of bone." *Bone*, vol. 42, no. 1, pp. 193–9, Jan. 2008.

[12] J. S. Nyman, L. E. Gorochow, R. Adam Horch, S. Uppuganti, A. Zein-Sabatto, M. K. Manhard, and M. D. Does, "Partial removal of pore and loosely bound water by low-energy drying decreases cortical bone toughness in young and old donors.," *Journal of the mechanical behavior of biomedical materials*, vol. 22, pp. 136–45, Jun. 2013.

[13] H. H. Ong, A. C. Wright, and F. W. Wehrli, "Deuterium nuclear magnetic resonance unambiguously quantifies pore and collagen-bound water in cortical bone.," *J Bone Miner Res*, vol. 27, no. 12, pp. 2573–2581, Jul. 2012.

[14] O. Löfman, I. Hallberg, K. Berglund, O. Wahlström, L. Kartous, A.-m. Rosenqvist, L. Larsson, and G. Toss, "Women with low-energy fracture should be investigated for osteoporosis," *Acta Orthopaedica*, vol. 78, no. 6, pp. 813–821, 2007.

[15] J. N. Farr, M. T. Drake, S. Amin, L. J. Melton III, L. K. McCready, and S. Khosla, "In vivo assessment of bone quality in postmenopausal women with type 2 diabetes," *J Bone Miner Res*, vol. 29, no. 4, pp. 787–95, Apr. 2014.

Chapter 7

Conclusions and Future Directions

This dissertation has brought the AIR and DAFP UTE MRI methods for imaging bound and pore water concentrations of cortical bone into a clinically relevant scope. The methods were first translated and implemented as clinically practical imaging sequences, validated by comparisons to NMR methods and by assessing good repeatability in vivo in the tibia and the radius. The AIR and DAFP methods were then tested as predictors of fracture risk by finding correlations of bound and pore water concentrations with material properties in ex vivo radii. A new technique for acquiring AIR and DAFP measurements was applied using 2D UTE, greatly enhancing the flexibility of the method and decreasing scan time, and making this method more applicable to both more bones of interest and to a broader clinical population. Finally, these AIR and DAFP methods were implemented on osteoporotic volunteers and compared with healthy controls to assess the sensitivity and feasibility of the method in the clinic.

Apart from the aforementioned clinical populations of interest for applying these bound and pore water concentration mapping methods in Chapter 6, there are several other future areas of interest related to the work in this dissertation. One potential use for these methods would be the ability to predict material properties related fracture, such as yield strain and modulus, with a model based on the bound and pore water concentrations on a voxel by voxel basis. Finite element analysis [1] is one way apply this by using bound and pore water concentrations as a basis for the model. This method can then simulate loading of the bone and predict a breaking force as a result. This method has already been applied to bone with QCT measurements [2]–[5]. With the 3D methods used in this study, the bound and pore water measurements could be used to predict biomechanical properties of the bone with greater precision than a metric of the concentration (e.g., mean) alone, or a metric of structure alone. Because the data in Chapter 4 has results from loading already,

this data would be an easily accessible way to testing finite element analysis. The 3D bound and pore water maps could be used in a finite element model and compared to the loading results from the three-point bend test.

A different application for bound and pore water imaging would be implementation in pre-clinical MRI systems. Animal systems offer much higher slew rates, gradient strength and maximum RF power than clinical systems. This would allow for higher resolution scans and higher SNR than is currently feasible with the human scanner, and would allow studies involving animals or ex vivo bones. Other scans that would be easier to implement on a pre-clinical scanner, such as zero echo time (ZTE) [6] or SWeep Imaging with Fourier Transform (SWIFT) [7], offer the potential for better quality images. SWIFT is an alternative method to UTE that uses interleaved RF excitation and signal acquisition. This results in a signal that essentially has a TE of zero, allowing for imaging of species with extremely short T_2 such as cortical bone. With SWIFT, it is easier to achieve a higher resolution, higher SNR scan in a more efficient manner than ramp sampling that is used in typical 3D UTE. The SWIFT package and software is fully developed and available for the Varian animal system, and can be adapted to include DAFP and AIR preparation pulses similar to the way they are included in the current 3D UTE implementation. Pre-clinical studies, both in vivo and ex vivo, would allow for in-depth studies of bound and pore water measurements, changes to bound and pore water concentrations, and drug development.

Other areas of improvement include alternate methods to speed up the acquisition, or increase the SNR, or both. Using dedicated coils for a particular area of interest could greatly help the SNR and potentially help to limit the field of view, such as with a surface coil. Other coils such as the 16 channel transmit-receive knee coil may help by using higher RF power to shorten pulses and achieve much higher SNR. Other improvements such as 3D radial imaging with an anisotropic FOV could help to reduce scan time [8]. Anisotropic FOV is straightforward in Cartesian imaging by reducing the number of k-space points acquired in a particular direction, but more complicated in a radial acquisition.

In radial imaging, points are sampled on projections that start in the center of k-space and are typically uniformly distributed on a circle or a sphere. Because the projections are rotated around a circle or sphere and no two are in the same direction, it is not possible to increase the spacing of projections by simply eliminating projections in the direction that the FOV is being reduced. However, recent work has shown that specific trajectories can be used to specify the FOV and the resolution in an anisotropic manner [9], [10]. Using an anisotropic FOV will be particularly useful in long bones such as the radius or tibia, where the signal variation along one dimension is significantly less than the other directions. In addition, anisotropic FOVs may be useful in all bones that have an anisotropic region of interest, since acquiring an isotropic FOV is inefficient because there is no signal in a significant part of the FOV.

The AIR and DAFP methods as presented in this dissertation are valuable tools, but are by no means optimized. Bone imaging with MRI is a relatively new field, and has various areas that could be improved. One first step would be to compare the AIR and DAFP methods to other MRI methods aiming to report on bone characteristics. Several methods have currently been reported in the literature, such as view-sharing methods with biexponential analysis to determine bound and pore water fractions [11], or the 3D hybrid radial sequence that uses a slab selective pulse for excitation and acquires the z direction with Cartesian sampling, while acquiring radially within the x-y plane (stack of stars) [12]. An interesting step would be to compare these methods directly, both from an accuracy or agreement standpoint but also to evaluate the SNR efficiency of the methods relative to each other. A study aiming to find the relative advantages and disadvantages of these tools to measure these bone water characteristics would be of great use to many researchers in this field.

To be truly clinically practical, a few, relatively straightforward, implementations will need to take place. First, reconstruction of images needs to happen at the scanner. This can be done on the scanner now, but it would be useful if it was integrated with the Philips

software using Recon 2.0. Since these quantitative methods require some analysis and segmentation, this should be straightforward and depend as little as possible on user input. The analysis includes several steps, such as finding the B_1^- map, segmenting the bone signal and the reference marker signal, finding the β factor on a voxel by voxel basis for the bone, converting the signal to proton densities using signal equations, and finally converting to units of absolute concentration using the reference marker signal. The Post-Processing (PRIDE) tool will be useful in helping to achieve this analysis at the scanner. Since a reference marker is needed in the field of view, this would ideally be in an accessible, disposable, marker with a known proton concentration, such as a commonly used MRI fiducial markers. The ability to have reconstruction, segmentation, and analysis done in a semi-automated, relatively quick manner will enhance repeatability and ease of use of the bone water imaging methods.

In conclusion, the work in this dissertation has brought forward a new avenue for bone imaging and diagnosing fracture risk. In the future, researchers will be able to build upon the methods presented here to improve the accuracy, utility and application of quantitative bone MRI.

7.1 References

[1] G. Strang and G. J. Fix, *An analysis of the finite element method*, Vol. 212. Englewood Cliffs, NJ: Prentice-Hall, 1973.

[2] R. Crawford, C. E. Cann, and T. M. Keaveny, "Finite element models predict in vitro vertebral body compressive strength better than quantitative computed tomography," *Bone*, vol. 33, no. 4, pp. 744–750, Oct. 2003.

[3] E. S. Orwoll, L. M. Marshall, C. M. Nielson, S. R. Cummings, J. Lapidus, J. A. Cauley, K. Ensrud, N. Lane, P. R. Hoffmann, D. L. Kopperdahl, and T. M. Keaveny, "Finite element analysis of the proximal femur and hip fracture risk in older men," *J Bone Miner Res*, vol. 24, no. 3, pp. 475–83, 2009.

[4] K. K. Nishiyama, H. M. Macdonald, D. a. Hanley, and S. K. Boyd, "Women with previous fragility fractures can be classified based on bone microarchitecture and finite element analysis measured with hr-pqct.," *Osteoporosis Int*, vol. 24, no. 5, pp. 1733–40, May 2013.

[5] N. Zhang, J. F. Magland, C. S. Rajapakse, Y. a. Bhagat, and F. W. Wehrli, "Potential of in vivo mri-based nonlinear finite-element analysis for the assessment of trabecular bone post-yield properties.," *Medical physics*, vol. 40, no. 5, p. 052 303, May 2013.

[6] M. Weiger, K. P. Pruessmann, and F. Hennel, "Mri with zero echo time: hard versus sweep pulse excitation.," *Magn Reson Med*, vol. 66, no. 2, pp. 379–89, Aug. 2011.

[7] D. Idiyatullin, C. Corum, J.-Y. Park, and M. Garwood, "Fast and quiet mri using a swept radiofrequency.," *J Magn Reson*, vol. 181, no. 2, pp. 342–9, Aug. 2006.

[8] P. Z. Larson, P. T. Gurney, and D. G. Nishimura, "Anisotropic field-of-views in radial imaging.," *IEEE transactions on medical imaging*, vol. 27, no. 1, pp. 47–57, Jan. 2008.

[9] P. E. Z. Larson, M. S. Lustig, and D. G. Nishimura, "Anisotropic field-of-view shapes for improved propeller imaging.," *Magn Reson Img*, vol. 27, no. 4, pp. 470–9, May 2009.

[10] C. Li, A. Siefert, J. Magland, and F. Wehrli, "Zero echo time (zte) imaging with anisotropic field-of-view," *Proc. Intl. Soc. Magn. Reson. Med. 21*, p. 762, 2013.

[11] E. Diaz, C. B. Chung, W. C. Bae, S. Statum, R. Znamirowski, G. M. Bydder, and J. Du, "Ultrashort echo time spectroscopic imaging (utesi): an efficient method for quantifying bound and free water.," *NMR Biomed*, vol. 25, no. 1, pp. 161–8, Jan. 2012.

[12] H. S. Rad, S. C. B. Lam, J. F. Magland, H. Ong, C. Li, H. K. Song, J. Love, and F. W. Wehrli, "Quantifying cortical bone water in vivo by three-dimensional ultrashort echo-time mri.," *NMR Biomed*, vol. 24, no. 7, pp. 855–64, Aug. 2011.